



Rita Joana da Cruz Roque

X-ray imaging using 100 μm thick Gas Electron Multipliers operating in Kr-CO₂ mixtures

Master's Dissertation in Engineering Physics, supervised by
Fernando Domingues Amaro and Cristina Maria Bernardes Monteiro and presented to the Faculty of Sciences and
Technology of Universidade de Coimbra

June 2018



UNIVERSIDADE DE COIMBRA

UNIVERSITY OF COIMBRA

MASTERS DISSERTATION

**X-ray imaging using 100 μm thick Gas
Electron Multipliers operating in Kr-CO₂
mixtures**

Author:

Rita Joana da Cruz Roque

Supervisors:

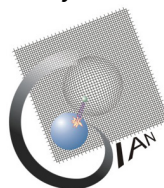
PhD Fernando Domingues Amaro
PhD Cristina Maria Bernardes Monteiro



*A dissertation submitted in fulfillment of the requirements
for the degree of Master in Engineering Physics*

in the

LibPhys UC
Department of Physics
Faculty of Sciences and Technology
University of Coimbra



May 29, 2018

TITLE:

X-ray imaging using 100 μm thick Gas Electron Multipliers operating in Kr-CO₂ mixtures

IMAGE IN COVER:

Doctors of the Great War - Marie Curie
"Flanders Fields"

AUTHOR:

Rita Joana da Cruz Roque

DATE:

May 29, 2018

SUPERVISORS:

Fernando Domingues Amaro
Cristina Maria Bernardes Monteiro

LOCATION:

Physics Department: LibPhys UC
Faculty of Sciences and Technology
University of Coimbra
Coimbra, Portugal

“A scientist in his laboratory is not a mere technician:
he is also a child confronting natural phenomena that impress him as though they
were fairy tales.”

— Marie Curie —

Dedicated to the giants of my life, who always carried me on their shoulders.

ABSTRACT

Krypton is known to have the best value of position resolution amongst the noble gases within the range 14 – 34 keV, which makes it a good candidate for imaging applications. Also, the choosing of 100 μm thick Gas Electron Multipliers (GEM) over the standard GEM plates presents an undeniable advantage as the former is more robust to sparking while achieving similar multiplication coefficients. By taking these factors into account, higher charge gains and lower values of position resolution can be achieved to produce cleaner imaging data in the energy range 14 – 34 keV.

A cascade of two non-standard GEM plates (twice the thickness of a standard GEM) fabricated at CERN was coupled to a 2D resistive readout with an active area of $10 \times 10 \text{ cm}^2$. This setup allows event energy and interaction position information to be recorded using only four channels, simplifying the electronic system and the image reconstruction process. This detection system was operated in krypton-based mixtures and irradiated by a ^{55}Fe and a continuous x-ray source. Whenever possible, the results were compared to the ones achieved in a Ar-CO₂ (70:30) mixture.

Parameters such as the charge gain, energy resolution, image signal-to-noise ratio, position resolution and contrast response were measured under the described conditions. For krypton-based mixtures, the reduction of position resolution and increase in contrast response happened for radiation energies higher than 18 keV.

Keywords: X-ray imaging, electron multipliers (gas), gaseous detectors, micropattern gaseous detectors (MSGC, GEM, THGEM, RETHGEM, MHSP, MICROPIC, MICROMEGAS, InGrid), krypton, position resolution, image quality, contrast response.

RESUMO

O cripton é o gás nobre que possui os melhores valores de resolução espacial para energias entre 14 – 34 keV, o que o torna um bom candidato para aplicações de imagiologia. Além disso, a escolha de *Gas Electron Multipliers* (GEM) com 100 μm de espessura ao invés de um GEM *standard* representa uma vantagem inegável; os primeiros são mais robustos a descargas, atingindo coeficientes de multiplicação semelhantes. Combinando estas duas características, é possível atingir ganhos em carga mais elevados e melhores valores de resolução espacial, o que permite obter imagens mais detalhadas no intervalo de energias 14 – 34 keV.

Uma cascata de dois GEMs não convencionais (com o dobro da espessura de um GEM *standard*) fabricados no CERN foi associada a uma placa resistiva de leitura bidimensional, com uma área ativa de $10 \times 10 \text{ cm}^2$. Esta montagem permite recolher informação sobre a energia e a posição de cada evento usando apenas quatro canais, simplificando a eletrônica associada, bem como a própria reconstrução das imagens. Este detetor foi operado em misturas baseadas em cripton e irradiado com uma fonte de ^{55}Fe e com uma fonte contínua de raios-x. Sempre que possível, os resultados foram comparados com as medidas obtidas com uma mistura Ar-CO₂ (70:30).

Parâmetros como ganho em carga, resolução em energia, relação sinal ruído das imagens, resolução espacial e resposta em contraste foram determinados nestas condições. Para as misturas baseadas em cripton, verificou-se uma redução na resolução espacial e um aumento de contraste para energias acima dos 18 keV.

Palavras-Chave: Imagiologia de raios-x, multiplicadores de elétrons (gás), detetores gasosos, *multipattern gaseous detectors* (MSGC, GEM, THGEM, RETHGEM, MHSP, MICROPIC, MICROMEGAS, InGrid), cripton, resolução espacial, qualidade de imagem, resposta em contraste.

PUBLICATIONS

IN INTERNATIONAL JOURNALS WITH PEER-REVIEW

DECEMBER 2017: **Gain characteristics of a 100 μm thick GEM in Krypton-CO₂ mixtures** (R. C. Roque, H. Natal da Luz, L. F. N. D. Carramate, C. D. R. Azevedo, J. A. Mir, F. D. Amaro), *JINST - Journal of Instrumentation* 12 C12061.

ORAL COMMUNICATIONS

NOVEMBER 2017: **Potentials of an imaging system based on a GEM (100 μm thick) gaseous detector operating in krypton-CO₂ mixtures** (R. C. Roque, F. D. Amaro, H. Natal da Luz, L. F. N. D. Carramate, C. D. R. Azevedo, J. A. Mir), *FisMed 2017 - Encontro Nacional de Física Médica*, Coimbra, Portugal.

POSTER PRESENTATIONS

JULY 2017: **Operation of 100 micron thick GEM in Krypton-CO₂ mixtures** (F. D. Amaro, R. C. Roque, H. Natal da Luz, L. F. N. D. Carramate, C. D. R. Azevedo, J. A. Mir), *iWoRiD 2017*, Krakow, Poland.

JUNE 2018: **Spatial resolution properties of krypton-based mixtures using a 100 μm thick Gas Electron Multiplier** (R. C. Roque, F. D. Amaro, H. Natal da Luz, L. F. N. D. Carramate, C. D. R. Azevedo, J. A. Mir), *EXRS 2018 - European Conference on X-ray Spectrometry*, Ljubljana, Slovenia (accepted).

*“Nothing in life is to be feared,
it is only to be understood.
Now is the time to understand more,
so that we may fear less.”*

— Marie Curie

ACKNOWLEDGEMENTS

First of all, I would like to leave a warm thank you to my high school physics teacher Rosa Lourenço for showing me the beauty of physics and without whom I would certainly follow a very different path.

To everyone who contributed in some way to my education, academic or not.

Also, a thank you note to professor Joaquim dos Santos for inviting me for this project and for all the support and interest in my future.

To all members of GIAN who warmly welcomed me.

A very special thanks to my supervisor Fernando Amaro, who guided me through the entire process, always available and opened to my questions and concerns.

To Cristina Monteiro, for reviewing my work.

To the entire collaboration group. To Lara, who taught me the tricks of the CAEN manual. To Hugo, who 8000 km away and with 4 hours of time difference helped me to improve my work in many ways: from the discussions and corrections to the kind suggestions.

To my parents to whom I cannot find enough words to thank.

To my sister, Inês, my partner in crime and best friend in the world.

To Marcos, who always offers me infinity.

CONTENTS

1	INTRODUCTION	1
1.1	Objectives	1
1.2	Motivation	1
1.3	Approach	2
1.4	Project planning	2
1.5	Organization	3
I	FUNDAMENTALS	5
2	RADIATION INTERACTION WITH MATTER	7
2.1	X-rays	7
2.1.1	X-ray production	7
2.1.2	X-ray interaction with matter	10
2.2	Electron interaction with matter	13
3	GASEOUS DETECTORS	15
3.1	Operation principle	15
3.2	Ionization chambers	16
3.3	Gas proportional counters	17
3.4	Micropattern gaseous detectors	18
3.4.1	Gas electron multiplier	18
3.5	Gas medium	20
3.5.1	Gas selection	20
3.5.2	Gas aging	22
4	CONCEPTS ON DETECTOR IMAGING	25
4.1	Fundamentals of image acquisition	25
4.2	Detector image quality	25
4.2.1	Charge gain	26
4.2.2	Energy resolution	26
4.2.3	Image signal-to-noise ratio	27
4.2.4	Spatial resolution	28
4.2.5	Position resolution limitations	31
II	EXPERIMENTAL SETUP	37
5	SYSTEM DESCRIPTION	39
5.1	System overview	39
5.2	X-ray source	40
5.2.1	Radioactive ^{55}Fe source	40
5.2.2	X-ray generator	40
5.3	Gas system	40
5.3.1	Gas containers	41
5.3.2	Mass flux controllers	42
5.3.3	Detector connection	42
5.3.4	Exit filter	42
5.4	Electronic system	42
5.4.1	Optimization studies	43
5.4.2	Imaging studies	44

6	DETECTOR DESCRIPTION	47
6.1	Detector configuration	47
6.2	Gaseous chamber	48
6.3	Cathode mesh	48
6.4	G-100 plates	48
6.5	Readout board	49
6.6	Structure biasing apparatus	50
7	AUXILIARY MATERIAL	51
7.1	MTF mask	51
7.2	Wood mannequin	52
7.3	Music box	53
7.4	Geomag® kit	54
III	SOFTWARE DEVELOPMENT AND TESTING	55
8	SOFTWARE REQUIREMENT SPECIFICATION	57
8.1	Functional description	57
8.2	User's profile	57
8.3	Input and preconditions	57
8.4	Output	57
8.5	Successful completion	57
8.6	Speed of operation	58
8.7	Additional characteristics	58
8.8	Quality	58
9	SOFTWARE DEVELOPMENT	59
9.1	Image reconstruction	59
9.1.1	File reading	59
9.1.2	Event resolving	59
9.1.3	Event position determination	63
9.2	Image analysis tools	66
9.2.1	Point source profiling	66
9.2.2	Double slit profiling	67
9.2.3	Position resolution and MTF determination	67
9.2.4	SNR determination	69
9.2.5	Energy filtering	69
10	SOFTWARE TESTING	71
10.1	Functional requirements	71
10.2	Speed of operation	71
10.3	Compatibility and maintainability	72
10.4	Flexibility	72
10.5	Quality	72
10.6	Limitations	73
IV	EXPERIMENTAL RESULTS AND DISCUSSION	75
11	DETECTOR CALIBRATION AND OPTIMIZATION	77
11.1	Electronic calibration	77
11.2	Energy calibration	79
11.3	Position calibration	79
11.4	Electronic optimization	80
11.4.1	Drift region	81

11.4.2	Transfer region	82
11.4.3	Induction region	83
11.5	Signal optimization for the imaging studies	84
12	EVALUATION OF DETECTOR PERFORMANCE	87
12.1	Time stability	87
12.2	Spatial uniformity	88
12.2.1	Charge gain and energy resolution	88
12.2.2	Image distortion	89
12.2.3	Position resolution	90
12.3	Charge gain and energy resolution	91
12.4	Signal-to-noise ratio	93
12.5	Spatial resolution	95
12.6	Contrast response	96
12.7	Imaging characteristics	97
12.7.1	Wood mannequin	97
12.7.2	Music box	97
12.7.3	Geomag® kit	98
13	FINAL REMARKS	101
13.1	Conclusion	101
13.2	Applications	102
13.3	Future work	102
V	APPENDIX	107
A	SCREENSHOTS OF THE ANALYSIS ENVIRONMENT	109
B	ANALYSIS IMAGES	111

LIST OF FIGURES

Figure 1	Schematics of a conventional x-ray tube	8
Figure 2	Bremsstrahlung and characteristic radiation mechanisms:	8
Figure 3	Energy spectrum of <i>bremsstrahlung</i> and characteristic x-rays . .	9
Figure 4	Moseley plot	10
Figure 5	The three major types of x-ray interaction	11
Figure 6	Photoelectric absorption	12
Figure 7	Compton scattering	12
Figure 8	Pair production	13
Figure 9	Operating regions of gaseous detectors	15
Figure 10	Ionization chamber	17
Figure 11	Gas proportional counter	17
Figure 12	GEM structure observed with an electron microscope	19
Figure 13	Field lines and equipotentials imposed by a GEM	19
Figure 14	Position resolution for different noble gases	21
Figure 15	X-ray absorption of different noble gases	22
Figure 16	Steps of digital image acquisition	25
Figure 17	Charge gains for single, double and triple GEM setup	26
Figure 18	Full width at half maximum	27
Figure 19	Spatial resolution of a digital image	29
Figure 20	Characteristics of the point spread function	29
Figure 21	Line, edge and modulation transfer functions of a digital image	30
Figure 22	Position resolution as a function of x-ray energy	32
Figure 23	Resistive charge division	33
Figure 24	Image magnification and uncertainty	34
Figure 25	Block diagram of the experimental system	39
Figure 26	Schematics of the gas system	41
Figure 27	Electronic system setup used for the optimization studies . . .	43
Figure 28	Electric signals along the electronic system	44
Figure 29	Electronic system setup used for the imaging studies	44
Figure 30	Signal processing using the CAEN digital approach	45
Figure 31	Configuration of the G-100-based MPGD	47
Figure 32	Gaseous chamber	48
Figure 33	Assembly of the G-100 plates	49
Figure 34	Schematics of the 2D resistive readout	50
Figure 35	MTF mask used as an imaging target	51
Figure 36	Lead x-ray attenuation characteristics	52
Figure 37	Wooden dummy used as an imaging target	52
Figure 38	X-ray attenuation of soft tissue, wood, and cortical bone	53
Figure 39	Interior of the music box	53
Figure 40	Geomag® kit	54
Figure 41	Coincidence analysis algorithm	60
Figure 42	Time window optimization data	62
Figure 43	Time window optimization	62
Figure 44	Characteristics of the reconstruction equations	64

Figure 45	Point source location using Gaussian fitting	64
Figure 46	Point source distribution in an equally-spaced grid	65
Figure 47	Distortion quantification for the reconstruction equations	66
Figure 48	Edge-gradient analysis algorithm	68
Figure 49	Implementation of the edge-gradient algorithm	68
Figure 50	Consistency of the position resolution determination	73
Figure 51	Electronic calibration system setup	77
Figure 52	Electronic calibration curves	78
Figure 53	Energy spectrum of a ^{55}Fe source in Ar-CO ₂ (70:30)	79
Figure 54	Schematics of the position calibration method	80
Figure 55	Drift field optimization	82
Figure 56	Transfer field optimization	83
Figure 57	Induction field optimization	84
Figure 58	Time stability of charge gain	87
Figure 59	Perforated grid used to study the uniformity of the detector	88
Figure 60	Charge gain variation with position	89
Figure 61	Energy resolution variation with position	89
Figure 62	Geometric distortion of the detector	90
Figure 63	Horizontal FWHM uniformity	90
Figure 64	Vertical FWHM uniformity	91
Figure 65	Charge gain and energy resolution	92
Figure 66	Pulse height distribution for pure krypton and Kr-CO ₂ (80:20)	93
Figure 67	RoI determination for image SNR calculation	94
Figure 68	Image SNR of different krypton-based mixtures	94
Figure 69	Position resolution as a function of radiation energy	95
Figure 70	MTF for energies within the 22 – 24 keV range	96
Figure 71	Wooden dummy imaging for Kr-CO ₂ mixtures	97
Figure 72	Music box imaging for Kr-CO ₂ (90:10)	98
Figure 73	Geomag kit imaging for Kr-CO ₂ (90:10)	99
Figure 74	Image reconstruction cell	109
Figure 75	Sub-image reconstruction cell	110
Figure 76	Images used for SNR, position resolution and MTF determination	111

LIST OF TABLES

Table 1	Cross sections for x-ray interactions	10
Table 2	Characteristics of different noble gases	21
Table 3	SNR values imposed by the ISO 12232 – 2006 standard	28
Table 4	Characteristic x-rays of a ⁵⁵ Fe source	40
Table 5	Density of different Kr-CO ₂ mixtures	42
Table 6	Position calibration constants used for quantitative analysis	80
Table 7	Electric fields for the drift region optimization	81
Table 8	Electric fields for the transfer region optimization	82
Table 9	Electric fields for the induction region optimization	83
Table 10	Optimized electric conditions for krypton mixtures	86
Table 11	Electric fields used for the charge gain and energy resolution study	92
Table 12	Quality parameters of krypton mixtures	99
Table 13	Charge gain and energy resolution for the quantitative analysis	112

ACRONYMS

1/2/3/4D	one/two/three/four D imensional
ADC	Analog to D igital C onverter
BNC	B ayonet N eill– C oncelman C onector
CERN	C onseil E uropéen pour la R echerche N ucléaire
ESF	E dge S pread F unction
FWHM	F ull W idth at H alf M aximum
G-100	Non-standard G as E lectron M ultiplier (100 µm thick)
GEM	G as E lectron M ultiplier
GIAN	G ruppo de I nstrumentação A tômica e N uclear
INL	I ntegral N onlinearity
LSB	L east S ignificant B it
LSF	L ine S pread F unction
MCA	M ulti C hannel A nalysers
MPGD	M icropattern G aseous D etector
MTF	M odulation T ransfer F unction
NIST	N ational I nstitute of S tandards and T echnology
NTP	N ormal T emperature and P ressure (293.15 K, 101.325 kPa)
OTF	O ptical T ransfer F unction
PSF	P oint S pread F unction
RoI	R egion of I nterest
SNR	S ignal-to- N oise R atio
SRS	S oftware R equirement S pecification
USB	U niversal S erial B us
UV	U ltra V iolet
XRF	X - R ay F luorescence

PHYSICAL CONSTANTS

Electron rest mass: $m_0 = 510.9989461(31) \text{ keV}$

Elementary charge: $e = 1.602\,176\,620\,8(98) \times 10^{-19} \text{ C}$

Planck constant: $h = 4.135\,667\,662(25) \times 10^{-15} \text{ eV} \cdot \text{s}$

Speed of light (vacuum): $c = 299\,792\,458 \text{ m s}^{-1}$

Standard acceleration of gravity: $g = 9.80665 \text{ m s}^{-2}$

LIST OF SYMBOLS

a: edge discontinuity location	w: energy of the first ionization
a_R : for the right edge	x: horizontal coordinate
a_L : for the left edge	\bar{x} : average value
\mathcal{A} : distribution amplitude	X: signal in the x coordinate
E: energy	X_A : in the A terminal
E_e : of the electron	X_B : in the B terminal
E_p : of the photon	y: vertical coordinate
E_T : deposited in the detector	Y: signal in the y coordinate
F: Fano factor	Y_A : in the A terminal
L: position calibration factor	Y_B : in the B terminal
\mathcal{M} : magnification	Z: atomic number
R: resolution	θ : angle
R_e : regarding the energy	μ/ρ : mass attenuation coefficient
R_p : regarding the position	ν : wave frequency
ΔV : voltage difference	σ : standard deviation

All values correspond to the information found at the foundation of modern science and technology from the Physical Measurement Laboratory of NIST.

Only the symbols that are used in more than one section are specified in this list.

INTRODUCTION

1.1 OBJECTIVES

The main objective of this project was the study of an x-ray imaging detector with a double cascade of non-standard gas electron multipliers (GEM) (100 μm thick), here named as G-100. This micropattern gaseous detector (MPGD) was operated under different krypton-carbon dioxide mixtures with proportions (100 : 0), (90 : 10), (80 : 20), (70 : 30) and (60 : 40). The detector's performance was quantified regarding charge gain, energy resolution, signal-to-noise ratio, position resolution and the modulation transfer function value at 10%.

1.2 MOTIVATION

The discovery of x-rays by Röntgen in 1895 has made it possible to explore, without surgical aid, the interior of the human body, to "see" and to photograph the bones and the organs; in 1914 only a limited number of Röntgen machines existed in France and were used by radiographic doctors. The wartime Military Health Service had provided equipment in certain big centers considered worthy of the luxury: that was all. (...)

Marie Curie found the solution. She created, with funds from the Union of Women in France, the first "radiological car"; it was an ordinary motor-car in which she put a Röntgen apparatus and a dynamo which, driven by the motor of the car, furnished the necessary current. This complete mobile station circulated from hospital to hospital from August 1914 onward; it was the only one to take care of the examination of the wounded evacuated toward Paris during the Battle of the Marne.

- Eve Curie in *Madame Curie*: February 1938 [1]

These *radiological cars* were nicknamed the *little Curies* and they traveled across France to find the wounded and to help in their treatment. They gave the doctors the necessary tools to see inside the human body without the painful resource to surgery. The advantages of using x-rays to image the invisible world were and remain innumerable and many researchers focus their efforts in developing radiation-based systems to image what lays hidden from the human sight.

Radiation detection using gaseous detectors traces back to 1908 with the invention of the *Geiger-Müller counter*. Since its discovery, their intrinsic potential was evident and efforts were made to use detectors as imaging systems. The first step towards imaging applications was the development of the *Multiwire proportional chamber* in 1968 [2].

During the eighties, MPGDs represented a new technology that showed lots of promise as the manufacture of more detailed structures was now possible. In the nineties, a new type of MPGD was introduced; the *Gas Electron Multiplier* (GEM) achieved higher charge multiplication coefficients due to its ability to operate in a cascade assembly. Another advantage is the capability GEMs have to suppress photon-feedback processes, thus improving the detector's gain and performance. Because of

this, after the introduction of gas electron multipliers, noble gases became, once more, a current topic of discussion in detector applications [3]. Also, like many others, these structures are also capable of preserving spatial information during the charge multiplication process. Because of this set of advantages, GEMs are the most common technology in imaging applications based on gaseous radiation detectors [2].

The fields in which imaging radiation detection is preponderant are vast and include high-energy physics, astrophysics, neutron and proton detection as well as medical imaging, security check and quality control. MPGDs are used throughout these applications, which makes them a current topic of discussion.

1.3 APPROACH

This dissertation project was firstly designed as a follow-up study of the masters degree thesis referenced in [4] and the articles associated with that work ([5]–[7]). The project focused on studying the behavior of a 100 μm thick GEM (G-100) gaseous detector for imaging applications using a gas mixture of argon and carbon dioxide.

These studies concluded that, using an Ar-CO₂ (70 : 30) mixture, gain charges of 3×10^3 and 10^4 were achieved in a single and double amplification stages configuration, respectively. The results showed the G-100 ability to reproduce the values achieved with standard GEM structures, while guarantying lower chances of spark-caused damage. Image acquisition was also performed with the same detector and gas mixture, achieving energy resolutions of 21% and charge gains above 10^4 (using a ⁵⁵Fe radioactive source). Using an x-ray generator, the minimum position resolution obtained was 1.69 mm.

Because krypton has the best value of position resolution among the noble gases in the range 14 – 34 keV [8], changing the gas is a natural step to increase the detector's performance. The presence of the krypton's absorption edge near 14 keV produces a sudden drop in position resolution, as the photoelectron range is minimized in this region. Due to this unique characteristic, krypton is a strong candidate for imaging detection within this energy interval.

By operating the MPGD in krypton-based mixtures, the same study regarding position resolution *versus* incoming photon energy was developed. It was also of interest to evaluate the behavior of different Kr-CO₂ mixtures so the optimum operation mode could be determined.

1.4 PROJECT PLANNING

The initial activities of this project focused, mainly, in the experimental work related to the detector characterization and were:

1. **Prototype assembly:** once this project was developed in the same research group as the previous investigation, the experimental setup was very similar to the one described in [4]. However, as the detector was out of work for more than half a year at the beginning of the research, cleaning and structure testing was fundamental to assure the detection system was not damaged and worked properly;
2. **Detector characterization:** to provide the best possible conditions during image acquisition, calibration and electric field optimization studies were required. For

this purpose, charge gain and energy resolution were measured for different electric field configurations and gas mixtures;

3. **Imaging system:** images were acquired for the optimized settings achieved in point 2. The correspondent data was processed and analyzed to quantify the position resolution of the detection system and compare its performance with existing gaseous detectors.

As the work progressed, new items were added to the initial proposition and were developed in parallel with the experimental procedures already enumerated:

- **Software development:** it was of interest to rewrite the previous analysis software from scratch to improve its applicability. The main requirements were to shorten the processing time, provide a fast visualization of the collected data during image acquisition and allow full processing of image data with personalized tools to determine and quantify image quality;
- **Quality measurement:** as this investigation was associated with a metrology and quality degree, a special focus was given to the characterization and quantification of the image quality. Therefore, a special care and focus was given to the calibration and optimization aspects of the project, especially regarding the determination of the quantitative parameters.

1.5 ORGANIZATION

This dissertation is divided in four parts, being the first one on the theoretical fundamentals, where the physical phenomena behind radiation interaction, the evolution of gaseous detectors and the concepts of detector imaging are discussed.

The second part describes the experimental setup and the different elements that compose the detection system, focusing on the gas flow, detector assembly, x-ray sources and on the electronic layout. Some auxiliary material of interest is also described.

The third part was reserved to report the software implementation and the developed features that were later used to analyze the data associated with the imaging studies. All the algorithms and methodologies regarding the analysis procedures are presented here.

In the fourth and last part, the experimental procedures regarding the calibration, optimization and the results of detector performance evaluation are presented and discussed.

Part I
FUNDAMENTALS

This chapter reviews the most important physical phenomena that supports the operation of gaseous x-ray detectors. As a consequence, x-ray production and its interaction with matter are indispensable to understand the functioning of this kind of detectors. The production of x-rays introduces how the radiation sources used to ionize the gas inside the detector work and their limitations. X-ray interaction with matter, on the other end, describes how the incoming x-rays will interact with the gas molecules by freeing electrons to produce a detectable signal.

After the photon-mediated interactions take place, free electrons are produced and travel through the gas medium until they reach the anode. Because of this, a brief discussion of the possible ways in which electrons may interact with matter is presented.

2.1 X-RAYS

X-rays are a type of electromagnetic radiation originated by atomic transitions, having wavelengths between 10^{-8} m and 10^{-12} m. They are high-energy photons (about a few keV) and were discovered by Wilhelm Conrad Röntgen in 1885 [9]. The photon energy, E_p , is related to the correspondent wave frequency, ν , by the Planck constant, h , as seen in equation 1.

$$E_p = h\nu \quad (1)$$

They are commonly used in several areas of medicine for diagnosis and treatment purposes. However, they have the ability to damage or even to destroy living tissues of the human body so care is needed to prevent overexposure to this type of radiation. They also represent a relevant tool in the field of crystallography because its wavelengths have similar dimensions to the atomic separations of solid materials (≈ 0.1 nm) [9], [10]. X-ray imaging is also used for security purposes in the form of checkpoint metal detectors to protect critical infrastructures such as airports, prisons, government buildings, among other examples [11].

2.1.1 X-ray production

To create x-rays with conventional x-ray tubes like the one shown in figure 1, electrons are emitted from a cathode and accelerated by a voltage induced at the anode.

The kinetic energy lost at the anode is transformed into x-rays by *bremsstrahlung* and *characteristic radiation* mechanisms. The whole apparatus is maintained under vacuum conditions [9].

The efficiency of an x-ray tube is highly dependent on the atomic number (Z) of the target material and on the energy of the electrons that leave the cathode. Tungsten ($Z = 74$) is commonly used as the target material because of intrinsic characteristics like endurance to high temperatures. The radiation is produced in the focal point which is a small area defined by the dimensions of the incident electron beam. A housing acts as a shield, absorbing the x-radiation, leaving only a small window (usually made of beryllium) to allow the passage of a collimated x-ray beam to the exterior [13].

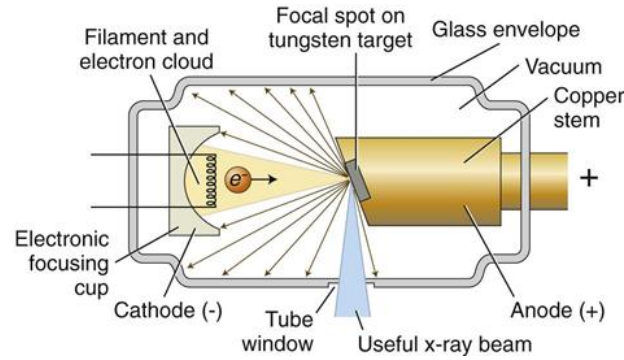


Figure 1: **Schematics of a conventional x-ray tube:** the electrons (e^-) are emitted from the cathode and collected at the anode releasing x-ray radiation [12].

2.1.1.1 *Bremsstrahlung radiation*

When fast electrons go through a certain medium, they are subjected to a specific energy loss that depends on the type of the absorber material. When this energy loss is expressed by radiative processes, the *bremsstrahlung* effect occurs and electromagnetic radiation is emitted. When the incoming electrons have sufficiently high energy or the interaction happens close to the nucleus, the emitted radiation has the typical energy that belongs to the x-ray region of the spectrum [2].

The fraction of energy converted through *bremsstrahlung* in the form of x-rays increases with increasing electron energy and with increasing atomic number of the absorbent material [9].

As depicted in figure 2 (paths 1, 2 and 3), the electron is decelerated by the Coulomb forces imposed by the atoms of the absorbent material. This results in energy loss and deflection of the electron's path; for greater distances of interaction, lower energy x-rays are emitted. The maximum energy is achieved when there is a direct impact with the nucleus [2].

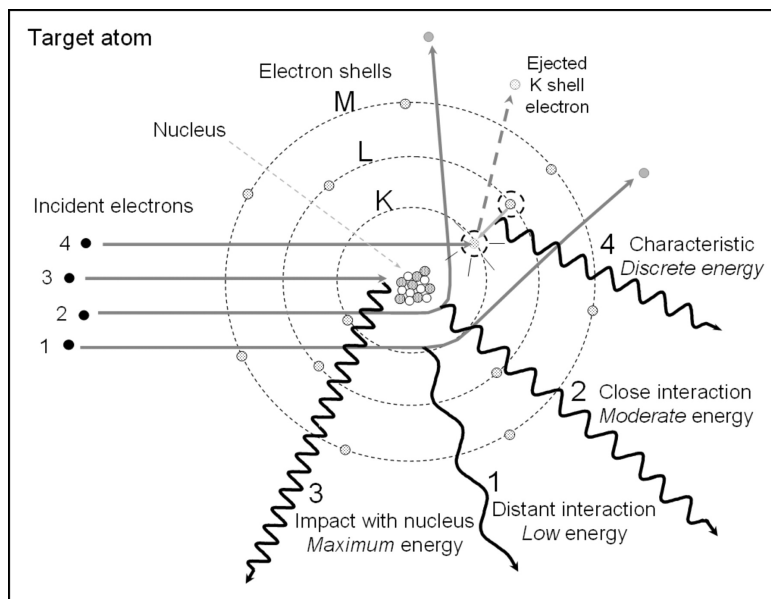


Figure 2: **Bremsstrahlung (1,2,3) and characteristic radiation (4) mechanisms:** the incident electrons interact with the target atoms resulting in x-ray production [14].

When mono-energetic electrons lose their energy through a *bremstrahlung* process, the photon energies are described by a continuum spectrum (as seen in figure 3). The energy of the incoming electron dictates the maximum photon energy than can be produced. [9].

2.1.1.2 Characteristic x-rays

Every time the orbital electrons of an atom suffer disruption as a consequence of some excitation process, the atom rearranges itself almost immediately, spending about 1 ns returning to its ground state [2]. One mechanism that returns the atom to its fundamental state implies the release of the extra energy within the atom in the form of a photon, creating the *characteristic x-ray* for that transition. The energy of the emitted photon is equal to the difference between the initial and final states of the atom. As a consequence, the characteristic x-rays have well known energies, depending on the atomic number of the atom and on the type of transition that occurs [2].

The production of the discrete energy x-rays is depicted in figure 2 in path 4, unleashed by an electron emission from the K-shell.

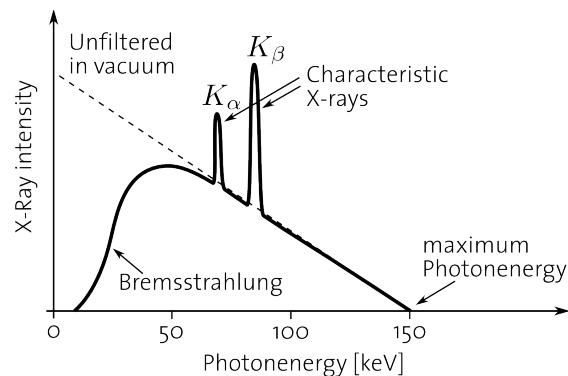


Figure 3: **Energy spectrum of *bremstrahlung* and characteristic x-rays:** the continuum energy spectrum due to the *bremstrahlung* mechanism is overlapped with the peaks correspondent to the photon production in characteristic x-rays [15].

The energy spectrum of this phenomena assumes a set of well defined peaks that correspond to the discrete energies of the emitted photons. When *bremstrahlung* occurs simultaneously with characteristic x-rays, these peaks are superimposed with the continuum spectrum, as figure 3 illustrates.

The energy of the emitted x-rays is related to the atomic number of the medium, Z and to the emission line they correspond to, following a linear law. Henry Moseley found that the energy of the emitted x-ray increased with increasing atomic number because, for larger Z values, the Coulomb charges in the atom are also larger and so are the energy differences between the atom's shells. This leads to the emission of more energetic x-rays. The findings of Henry Moseley are illustrated in figure 4 [16].

Because each element emits its characteristic x-rays with an unique frequency for each transition type, it is possible to identify the elements within a given sample by analyzing its x-ray spectrum [17]. This atomic analysis method is called *x-ray fluorescence* (XRF) and is very commonly used to study valuable artifacts like paintings and sculptures as it is a non-destructive method [18]. One interesting application of XRF is the reconstruction of underlying paintings by identifying metal-based color pigments in the XRF spectrum, such as described in [19].

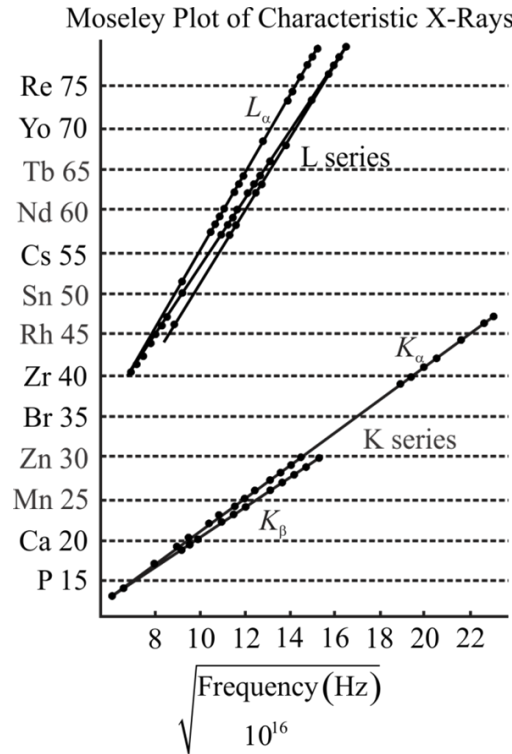


Figure 4: **Moseley plot:** the energy of the characteristic x-rays depends on the atomic number of the atom, Z , following a linear behavior for each emission line [16].

2.1.2 X-ray interaction with matter

There are four ways in which photons interact with matter, however only three effects have enough relevance in the study of x-ray behavior. These are the *photoelectric absorption*, *Compton scattering* and *pair production*.

These processes result in abrupt changes regarding the photon's original path and lead to total or partial energy transfer to the orbital electrons. After these interactions take place, the photon disappears or is scattered through a significant angle [2], [20].

These effects have different dominances according to the radiation energy and target material characteristics as shown in figure 5. Also, table 1 describes the cross section dependence on the type of radiation energy and on the media characteristics. Their relative dominance determines the shape of the resulting spectrum.

Table 1: **Cross sections for x-ray interactions:** the cross section σ_i of each interaction depends on the incident radiation energy, E_p , and on the absorber's atomic number, Z [21].

PHOTOELECTRIC	COMPTON SCATTERING	PAIR PRODUCTION
$\sigma_f \propto \frac{Z^5}{E_p^{7/2}}$	$\sigma_c \propto \frac{Z}{E_p}$	$\sigma_p \propto Z^2 \ln(2E_p)$

2.1.2.1 Mass attenuation coefficient

When photons go through a medium, the overall intensity of the beam is attenuated because of absorption and scattering effects. This intensity decrease is dependent on the kind of material the photons go through and on the radiation energy itself. This

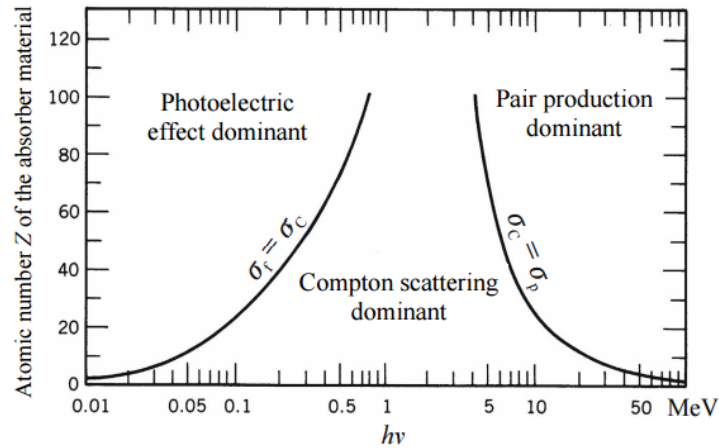


Figure 5: **The three major types of x-ray interaction:** *photoelectric absorption, Compton scattering and pair production* dominances are influenced by the photon energy and by the type of atoms present in the media. The lines show the values of Z and radiation energy for which the two neighboring effects have the same cross section [2].

quantity is expressed by the *attenuation coefficient*, which is a sum of the contributions of the partial attenuation coefficients for the various interaction processes. This is illustrated in equation 2, where μ is the total attenuation coefficient, and the other correspond to the *photoelectric absorption, Compton scattering and pair production* [22].

$$\mu = \tau + \sigma + \kappa \quad (2)$$

The attenuation coefficient (μ) can be determined experimentally by equation 3.

$$\frac{I}{I_0} = e^{-\mu \cdot t} \quad (3)$$

where I is the counting rate with the absorber, I_0 is the counting rate without the absorber and t is the absorber's thickness. The literature usually defines this parameter as μ/ρ (cm^2/g), dividing its value by the absorber's density. This parameter is called the *mass attenuation coefficient* [2].

2.1.2.2 Photoelectric absorption

This process implies the disappearance of the photon and its energy is transferred to a *photoelectron* that leaves its bound shell within the atom. The energy of the *photoelectron*, E_e , that is emitted is given by equation 4.

$$E_e = h\nu - E_b \quad (4)$$

where E_b is the binding energy of the electron in its shell before the interaction [2]. Figure 6 describes the main features of the photoelectric effect.

The gap created by the escaping *photoelectron* originates a disequilibrium within the atom and one of the mechanisms used to restore its ground state can result in *characteristic x-rays* (already described in 2.1.1.2) [2].

The photoelectric absorption process is most probable for soft x-rays because of the energy range associated with this type of radiation (see figure 5) [2].

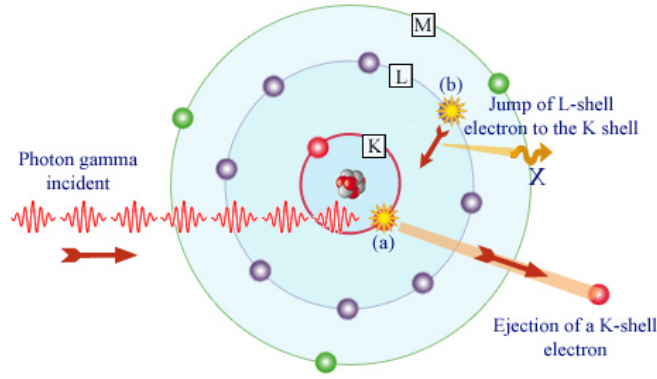


Figure 6: **Photoelectric absorption:** schematics of the photoelectron emission from a K shell (a). A characteristic x-ray is then produced (b) [23].

2.1.2.3 Compton scattering

Compton scattering results in the deflection of the incident photon through a given angle, θ , and the transference of a fraction of its energy, $h\nu$, to a *recoil electron* [2]. Figure 7 represents the Compton scattering process.

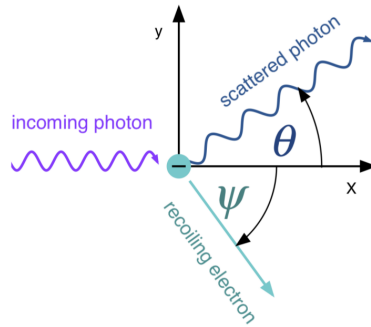


Figure 7: **Compton scattering:** an incident photon interacts with a target electron at rest by transferring a fraction of its initial energy. The *recoiling electron* scatters through a significant angle ψ and the *scattering photon*, through an angle θ [24].

All scattering angles θ are possible, although with different probabilities, and so the *recoil electron* can have an energy between 0 eV and a maximum value achievable when $\theta = \pi$. Equation 5 relates the final photon energy (E'_p) with the initial one and with the scattering angle.

$$E'_p = \frac{E_p}{1 + \frac{E_p}{m_0 c^2} (1 - \cos \theta)} \quad (5)$$

E_p is the photon's initial energy, m_0 , the rest mass of the electron and c , the speed of light in vacuum. This equation can be derived by considering a classic collision between particles with momentum and energy conservation [2].

2.1.2.4 Pair production

Every time the gamma ray energy is bigger than two times the rest mass of the electron ($2m_0 \approx 1.02 \text{ MeV}$), pair production can occur. During this process, the photon disappears originating an electron-positron pair. When the produced positron en-

counters an electron, an annihilation usually produces two photons (with energy of $\approx 0.51 \text{ MeV}$) as secondary byproducts [2]. Figure 8 illustrates the pair production effect.

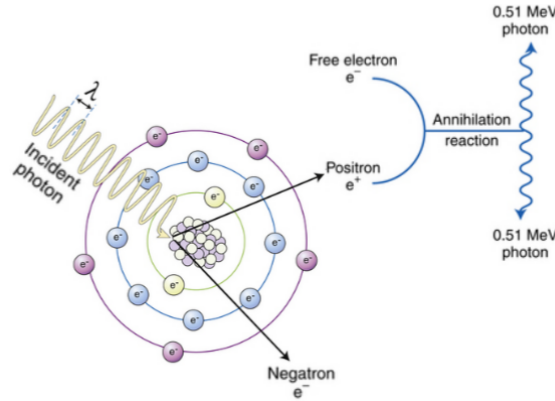


Figure 8: **Pair production:** the interaction originates the emission of a positron-electron pair. Later, the positron suffers an annihilation by encountering a free electron within the medium, producing two photons of energy $\approx 0.51 \text{ MeV}$ [25].

2.2 ELECTRON INTERACTION WITH MATTER

Electrons lose their energy in absorbing materials being easily deflected by the atoms of the medium, stopping only when all energy is transferred to their surroundings. Electron collisions with the absorbent medium determine an energy loss per unit of distance traveled determined by equation 6.

$$-\left(\frac{dE_e}{dx}\right)_c = \frac{2\pi e^4 N Z}{m_0 v^2} \left[\ln \frac{m_0 v^2 E_e}{2I^2(1-\beta^2)} - (\ln 2)(2\sqrt{1-\beta^2} - 1 + \beta^2) + (1-\beta^2) + \frac{1}{8}(1-\sqrt{1-\beta^2})^2 \right] \quad (6)$$

where N is the number density of the absorber atoms, e is the electron charge, v is the electron velocity, I is the average excitation and ionization potential of the absorber and $\beta = v/c$.

Besides collisional interactions, electrons also loose energy by radiative processes like *bremstrahlung*, already discussed in 2.1.1.1. The linear specific energy loss through this effect is described by equation 7.

$$-\left(\frac{dE_e}{dx}\right)_r = \frac{NE_e Z(Z+1)e^4}{137m_0^2 c^4} \left(4 \ln \frac{2E_e}{m_0 c^2} - \frac{4}{3} \right) \quad (7)$$

The total energy loss accounts for the contribution of the collision and radiative means of energy transference:

$$\frac{dE_e}{dx} = \left(\frac{dE_e}{dx}\right)_c + \left(\frac{dE_e}{dx}\right)_r \quad (8)$$

By applying an adequate electric field, it is possible to overcome this energy loss and accelerate the electrons through any medium.

CHAPTER OVERVIEW

As it was discussed, x-rays can be produced by an *x-ray tube* under two different but interdependent mechanisms, being them *characteristic radiation* and *bremsstrahlung*. X-rays are able to interact with matter by different physical processes depending on their energy and medium characteristics, such as *photoelectric absorption*, *compton scattering* and *pair production*.

The photon beam suffers a progressive intensity attenuation according to the absorber media they are subjected to. This attenuation is determined by the type and thickness of the medium as well as by the radiation energy.

By interacting with the gas molecules, x-rays are able to free electrons from the atom's media which are then decelerated by collision and radiative processes unless electric fields are applied nearby. These are the basic physical processes behind the operation of gaseous detectors.

GASEOUS DETECTORS

The most common types of radiation detectors are based on the ionization and excitation of gas molecules, leading to the production of electron-ion pairs. These pairs are then quantified as a detectable electronic output signal.

Ionization chambers, proportional counters and Geiger tubes are examples of this type of detectors and will be briefly discussed next as an introduction to the detector used in this work. Many detectors are left out of the discussion (as this topic is very vast) but the most relevant ones, such as the *gas electron multiplier*, are correspondingly highlighted.

3.1 OPERATION PRINCIPLE

Adopting a generalist and simplistic view, a gaseous detector is a chamber containing a gas medium and two electrodes inside. When radiation of sufficient energy goes through the gas medium, ionization or excitation processes occur (as described in the last chapter), originating free electrons and positive ions from the neutral gas molecules. An electric field imposed by the electrodes separates the positive charges to the cathode and negative ones to the anode. This effect creates a temporal variation of charge within the detector, *i.e.*, the production of an induced current. This current is then processed by the detector's electronics [2], [22].

Gaseous detectors can operate under different operation regions, according to the voltage imposed at the electrodes, as seen in figure 9. The number of electron-ion pairs produced for a certain incoming radiation is dictated by this voltage setting.

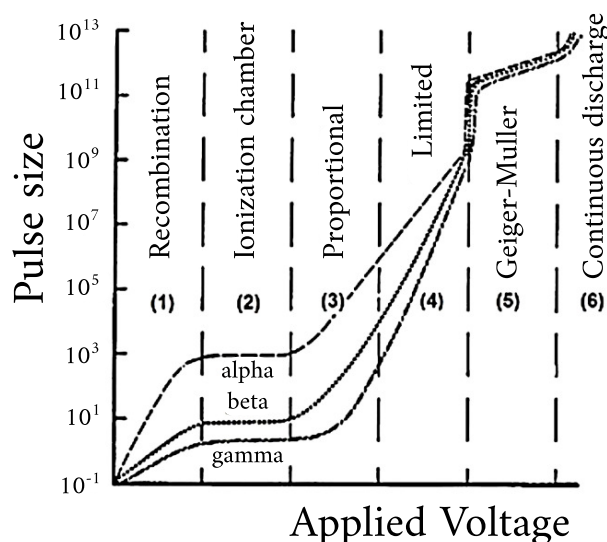


Figure 9: **Operating regions of gaseous detectors:** six different operating regions can be distinguished at different voltage ranges, being them the *recombination, ionization chamber, proportional, limited, Geiger-Müller* and *continuous discharge* regions [26].

Each numbered region can be characterized as [26]:

1. **Recombination region:** at low voltages, many electron-ion pairs suffer recombination before reaching the electrodes because the electric field is not strong enough to properly accelerate them. As the applied voltage increases, the recombination rate decreases and the pulse size grows accordingly. For detection purposes, this region is unusable and no detector operates in this domain;
2. **Ionization region:** the ionization region comprehends the voltage range at which (almost) all the ion pairs are collected at the electrodes. That is why this region presents a saturated profile and is associated with the operation of ionization chambers;
3. **Proportional region:** in this region, gas amplification is responsible for creating more electron-ion pairs that will then be collected at the correspondent electrodes and increase the output signal strength. This happens when the electrons from the primary ionization gain sufficient energy to originate new ionizations due to the strong electric field they are subjected to – *electron avalanche*. The gas amplification factor is commonly used to describe the multiplication process, being defined as the ratio between the number of ion pairs collected and the number of original ion pairs. In this region, as the applied voltage increases, the output signal increases proportionally, allowing particle distinguishing according to their energy.
4. **Limited proportional region:** in this region there is no proportionality between the output signal and the applied voltage because of non-linear effects. These are a consequence of the distortion of the electric field due to high concentration of positive ions. Just like the recombination region, this one is also avoided in detector applications.
5. **Geiger Müller region:** while in the proportional region each electron-ion pair produces a single avalanche, in the Geiger Müller operation mode multiple avalanches are originated from a single interaction. This happens because ultraviolet photons are emitted during the avalanche process, producing more free electrons that start new avalanches on their own. This region is used for the operation of Geiger Müller tubes but can only detect the presence of particles, being incapable of quantifying their energy.
6. **Continuous discharge region:** when the electric field alone is capable of producing ionization within the gas, continuous discharges occur. Once this operation region can permanently damage the detector, it is not used in experimental conditions.

3.2 IONIZATION CHAMBERS

According to the convention, ionization chambers are radiation detectors where electron-ion pairs are produced in a gaseous medium. A schematic of an ionization chamber is shown in figure 10. They are composed by two electrodes which can be arranged as parallel plates or in a cylinder-type geometry. A gaseous medium is imposed within [27].

The electric field created by the electrodes defines the charge paths; while electrons are collected at the anode, the heavy positive ions are gathered at the cathode. This

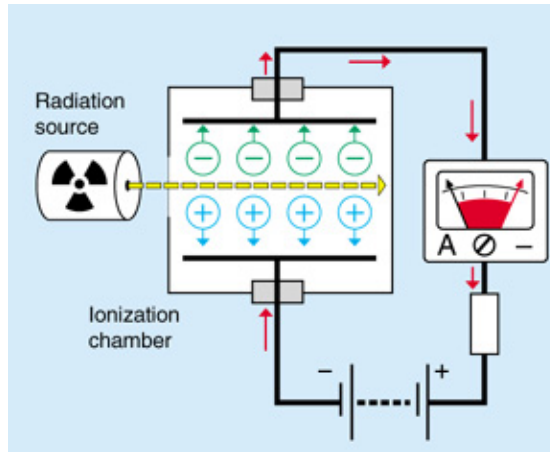


Figure 10: **Ionization chamber:** the charge separation imposed by the presence of an electric field creates an ionization current proportional to the number of electron-ion pairs produced by the ionizing radiation [27].

charge separation originates a small ionization current proportional to the number of ion-pairs collected [2].

3.3 GAS PROPORTIONAL COUNTERS

Proportional counters date back to the 1940s and operate with higher applied electric fields than the ionization chambers to allow charge multiplication of the original electron-ion pairs. This process is known as a *Townsend avalanche* and happens if the electrons have sufficient kinetic energy to surpass the ionization energy of the neutral gas molecules during a collision. Additional ionization occurs once more if the new free electrons experiment the same conditions [2]. The avalanche process stops only when all the free electrons are collected at the anode of the detector. A diagram of this process is depicted in figure 11 where each one of the four initial ionizations generates different avalanches.

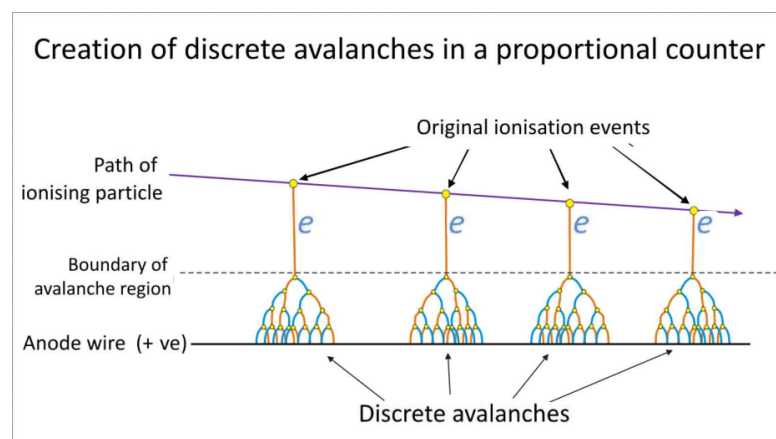


Figure 11: **Gas proportional counter:** the free electrons originated in the first ionization, having sufficient kinetic energy, are able to produce secondary ionizations of the gas molecules [28].

Unlike ionization chambers, gas proportional counters allow studies where the signal from the initial ionization is rather small; the multiplication process acts as a self-

sustained amplification of the electronic signal inside the detector. However, unlike ion chambers that allow operation with any kind of filling gas, proportional counters need a specific gas-type to permit the avalanche process and a frequent purification of the system is indispensable [20].

The basic geometry used for proportional counters consists on a cylindrical chamber where the walls operate as the cathode and a thin wire located at the center works as the anode. The interior of the container is commonly filled with a noble gas. The cylinder-type geometry creates a high electric field very close to the anode wire which is strong enough to sustain a Townsend avalanche. On the other side, a relatively low electric field is registered outside of this area, comprising a drift region where no multiplication takes place. In an ideal proportional counter, an electro-ion pair drifts until reaching the multiplication region close to the anode wire, where a single avalanche is formed, assuring the proportionality between the deposited energy and the collected charge [2].

3.4 MICROPATTERN GASEOUS DETECTORS

Micropattern gaseous detectors (MPGD) appeared in the late 80s and are defined as small-scale detailed structures or readouts that improve spatial resolution down to a few μm . This characteristic enables the usage of MPGDs in imaging applications, rapidly substituting wire-based imaging gaseous detectors such as the *multiwire proportional chamber* [2].

MPGDs have inherent advantages when compared to other detector types, such as lower position resolution ($\approx 30 \mu\text{m}$), high rate capability ($1 \times 10^6 \text{ Hz mm}^{-2}$), larger sensitive areas and operational stability. Furthermore, they are more resistant to performance degradation caused by incoming radiation [29]. They are also a low cost, versatile and portable solution for detector applications [22].

Microstrip gas chambers, *gas electron multipliers* and *micromegas* are examples of MPGDs [2]. For the purpose of this work, only *gas electron multipliers* will be discussed but complementary literature can be encountered in the reference above.

3.4.1 Gas electron multiplier

The *gas electron multiplier* (GEM) was developed by the physicist Fabio Sauli in 1996. In present days, it is the most popular gaseous ionization detector in fields where ionization pattern imaging is of great importance. High-energy physics, nuclear physics, astrophysics, and medical-imaging are some examples of its areas of application [30].

3.4.1.1 Typical structure

GEM is a hole-type structure, composed of a thin insulator sheet (made of a $50 \mu\text{m}$ thick kapton foil) where both surfaces have a metallic cladding (copper sheet about $5 \mu\text{m}$ thick). This foil has an hexagonal pattern of small holes with a double cone shape that go through the GEM with a diameter of $60 - 80 \mu\text{m}$ on the metallic surface and $40 - 60 \mu\text{m}$ at the center of the plate. The spacing between the holes within the hexagonal matrix is, typically, $140 \mu\text{m}$ [30]. The fine pattern of a GEM plate can be easily observed through an electron microscope as seen in figure 12.

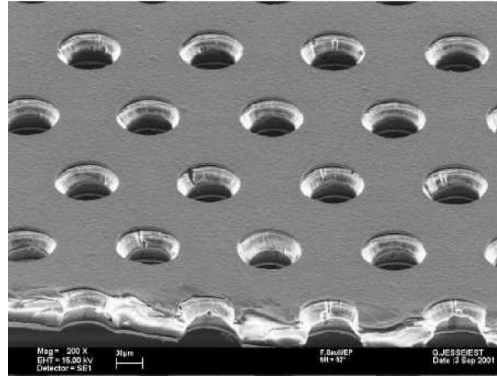


Figure 12: **GEM structure observed with an electron microscope:** the hole matrix allows the focusing of the electrons and charge multiplication [31]

A GEM plate is fabricated using micro-manufacturing procedures, such as *photolithography*¹ and *chemical etching*² techniques to guarantee a precise design and increase detector reliability. [30]

3.4.1.2 Operating principle

A GEM plate is operated according to the conditions of the proportional region (see figure 9) [22]. This structure is placed inside the detector between the area where the incident radiation interacts with the gas and the readout board. A high voltage is applied between the two metallic surfaces of the plate, creating an electric field within each hole. May this voltage be high enough, the field is sufficiently strong to cause electron avalanching [2].

The electric field and the correspondent equipotentials lines established when the GEM is under a voltage difference are represented in figure 13.

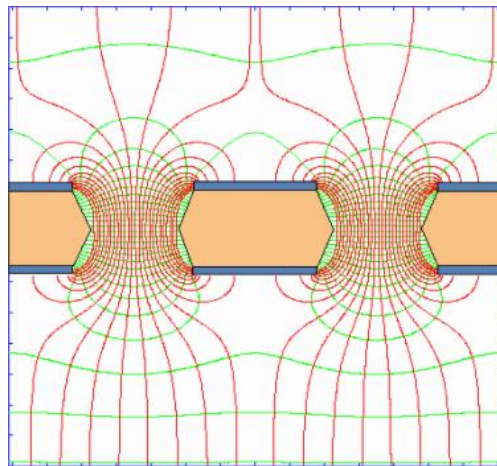


Figure 13: **Field lines (red) and equipotentials (green) imposed by a GEM:** they are the result of applying an adequate voltage between the metallic surfaces of the GEM. These field lines also account for the presence of two external electrodes, positioned before and after the GEM foil [32].

-
- 1 **Photolithography** is a manufacture process that transfers geometric shapes on a mask into a smooth surface by exposition to optical radiation.
 - 2 **Chemical etching** is the manufacture process that uses corrosive chemicals to dissolve away portions of metal and kapton and sculpt highly complex patterns.

When free electrons enter this high electric field region, charge multiplication occurs. Here, one single electron can produce about several hundred others, depending on the applied electric field. Due to the fine hole pattern of the plate, the diffusion of the electrons is minimal and the spatial information is preserved, making it a system with low position resolution values. This is compatible with high-resolution imaging applications [2].

Trying to increase the gain, it is common practice to arrange a *cascade* of GEM foils to add more multiplication stages and produce stronger output signals [3].

GEM-based detectors have the advantage of separating the multiplication step from the charge collection area. By doing so, the signal gathered at the readout plate is only caused by the incoming electrons, with the absence of the slow signal from the heavy ions. This simplifies the process of signal separation, reducing the probability of pileup and also fastens the electronic processing [29].

3.4.1.3 G-100 structure

Several efforts were made to further improve the performance of GEM structures such as the development of Thick GEMs (THGEM), *Optimized GEM* and Large Electron Multipliers (LEM) [33].

Following this trend, the G-100 structures were developed at GIAN. They are manufactured at CERN using the same wet chemical etch process of a standard GEM foil. They are fabricated from a 100 μm thick kapton foil (twice as thick as a standard GEM), having a hole diameter and pitch of 100 μm and 200 μm , respectively.

The usage of these plates provides a more robust detection system, lowering the chance of structure damaging by intense discharges between the electrodes.

3.5 GAS MEDIUM

The performance of gaseous radiation detectors is determined by various factors. One of them is the type of gas chosen as the ionization medium. Therefore, the most relevant points regarding this matter will be shortly discussed next.

3.5.1 Gas selection

Noble gases are commonly used as the absorbent media in radiation detection because of a wide variety of advantages such as the ones discussed below [21], [22] and quantified in table 2:

- **Stability:** noble gases are known to be inert under NTP conditions;
- **Purification:** noble gases, when compared to other types of gases, can be easily purified which is indispensable for experimental purposes;
- **Fano factor:** noble gases have relatively low Fano factors³ which means that the statistical limit for the energy resolution is also smaller;

³ The Fano factor, F , is a correction to Poisson statistics that predicts that the energy resolution of a detector is \sqrt{FN} , being N the number of particles detected. This correction implies an improvement in energy resolution which is actually defined by \sqrt{FN} .

- **Efficiency:** usually, gaseous detectors operate using noble gases because they allow higher efficiencies; noble gases do not form complex molecules so energy dissipation due to rotation or vibration effects is minimized.

Table 2: **Characteristics of different noble gases:** for argon, krypton and xenon the abundance in the earth's atmosphere, w -value and Fano factor are shown.

CHARACTERISTIC	ARGON	KRYPTON	XENON
ATOMIC NUMBER	18	36	54
ABUNDANCE [34]	9340.00 ppm	1.14 ppm	87 ppb
FANO FACTOR	0.16 [21]	$\leq 0.23(1)$ [35]	0.13(1) [21]
W-VALUE [36]	25.8(6) eV	24.0(7) eV	21.7(5) eV

Another fact that must not be forgotten is the cross section associated with the media. According to table 1, the higher the atomic number of the absorber, the higher is the probability of interaction (in all types of x-ray interaction). This means that using gases with bigger Z improves the detection efficiency [21].

Usually, a *penning mixture*⁴ is used, allowing energy transfer between the excited inert gas and the molecular gas through collisions. As a result, there is extra electron release, lowering the w -value and the Fano factor, thus improving the intrinsic energy resolution value [37].

Another parameter that must be taken into account is the position resolution as a function of the radiation energy for the different gaseous mixtures. Reference [8] shows a throughout study of position resolution for photons with energy between 1 – 60 keV in pure noble gases which is illustrated in figure 14.

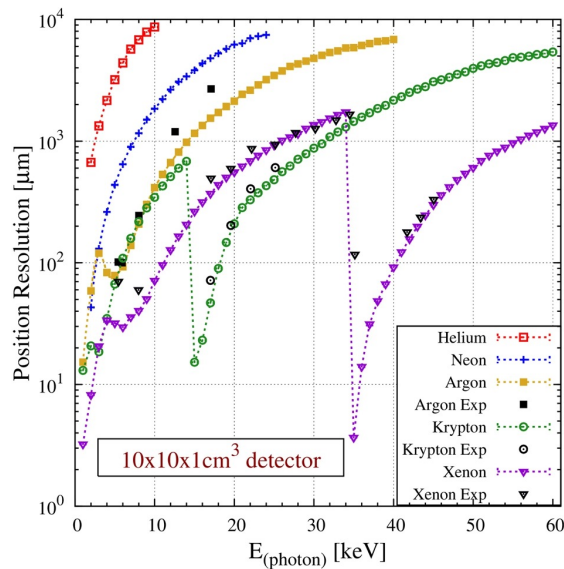


Figure 14: **Position resolution for different noble gases for a limited-volume detector:** in the range 14 – 34 keV, krypton has a better position resolution than helium, neon, argon and xenon, showing its potential for imaging applications [8].

4 **Penning Mixture:** mixture of an inert gas with a smaller amount of a different gas (typically, a molecular gas). This last component has lower ionization potential than the metastable excited state of the noble gas.

One of the most relevant statements of this work is the results for krypton in the range of 14 – 34 keV which were better than the ones measured for the other noble gases. This conclusion was the motivation behind the choice of krypton as the base gas for the current project. In the work [22], pure krypton usage in x-ray imaging was already evaluated, showing promising results. The main advantages of using krypton mixtures rely on [22]:

- **Spatial resolution:** because of the absorption edge of krypton near 14 keV, the spatial resolution decreases in this region. This happens because a higher photon energy is needed to produce free electrons with the same kinetic energy. Because many photons only have a slightly higher energy than the absorption edge, the emitted photoelectrons do not possess big values of kinetic energy. This small energy is rapidly lost near the place where the initial interaction took place. As a result, the charge avalanche spreads only over a small area, decreasing the value of the photoelectron range. As it will be later discussed, the diminishing of the photoelectron range means a smaller limitation in position resolution values.
- **X-ray absorption:** as it is illustrated in figure 15, krypton has a higher cross section for x-ray absorption than neon. Argon, however absorbing a slightly bigger quantity of x-rays for energies smaller than 15 keV, is surpassed by krypton after its absorption edge. This also happens for xenon, although with a smaller difference in x-ray attenuation.

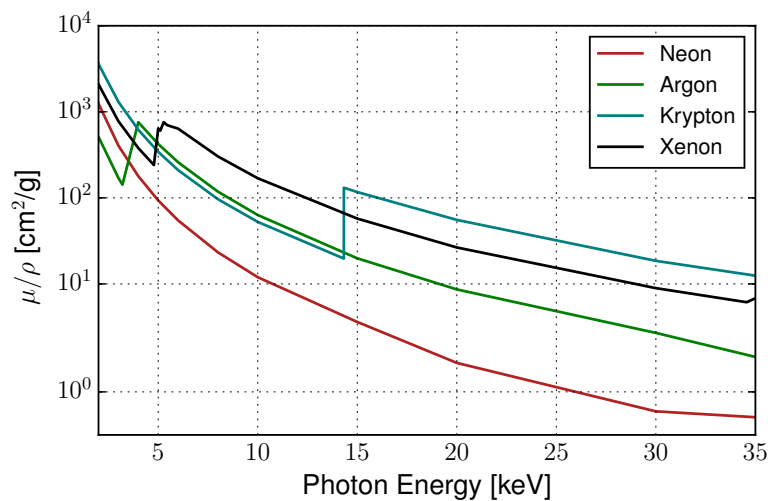


Figure 15: **X-ray absorption of different noble gases:** for neon, argon, krypton and xenon, the mass attenuation coefficient variation with radiation energy is shown. Data collected from [38].

This is an important factor because, as a higher quantity of radiation is absorbed by the gas medium, the stronger the output signal is, as more free electrons are produced.

3.5.2 Gas aging

When gaseous detectors are exposed to radiation for long periods of time, their performance tends to decrease, limiting their lifetime. This loss is due to local and permanent damages of the detector as a consequence of sparking occurrences. These

factors imply a loss in energy resolution and a loss and non-linearity of charge gain. The main causes that are behind this behavior are the presence of pollutants inside the detector chamber, the lack of isolation of the gas system and the occurrence of impurities within the gas [39].

Some procedures can be adopted to minimize the aging process such as an adequate selection of the gas mixture, gas purity, gas gain, gas system components and their assembly. A study about how these factors influence the performance of gaseous detectors is presented in reference [39]. One of the main conclusions of this work is that the usage of hydrocarbon mixtures is not the best for long-term applications because self-polymerization occurs. Instead, CO_2 and CF_4 mixtures are preferable but not completely immune to aging.

CHAPTER OVERVIEW

After discussing the main types of gaseous detectors and its characteristics, the vastness of work developed in this field is evident, contributing to a rich history regarding radiation detectors. Among these, the *gas electron multiplier* presents itself as a capable microstructure adequate for imaging applications because of its ability to preserve spatial information. More recently, the introduction of G-100 improved even further the potential of this structure by adding physical and electrical robustness to sparking without hurting the overall performance.

By reflecting upon the types of gas that are appropriate for image detection, krypton stands out as a strong candidate, promising low position resolution values in the energy range 14 – 34 keV.

CONCEPTS ON DETECTOR IMAGING

In this chapter, the characteristics of imaging detectors are discussed in terms of charge gain, energy resolution, image signal-to-noise ratio and position resolution. About this last parameter, the point, line and edge spread functions, as well as the modulation transfer function are discussed with detail because they are fundamental to quantify the imaging capabilities of any imaging system. The physical limitations that influence the position resolution of imaging detectors are also presented and discussed.

4.1 FUNDAMENTALS OF IMAGE ACQUISITION

To capture a scene element as a digital image, an energy source is needed to be reflected by the object. In some applications like x-ray imaging, the energy is transmitted through the scene elements that act as a radiation mask. The imaging system is responsible for collecting the incoming energy onto the image plane which is composed by a sensor array. Each sensor produces an output proportional to the amount of energy received which is then digitized independently. This process originates a digital image $f(x, y)$ where x and y are the horizontal and vertical dimensions and f is the amplitude or intensity of the corresponding pixel. All of these parameters assume discrete values during the quantization process [40]. The image acquisition process described is also illustrated in figure 16.

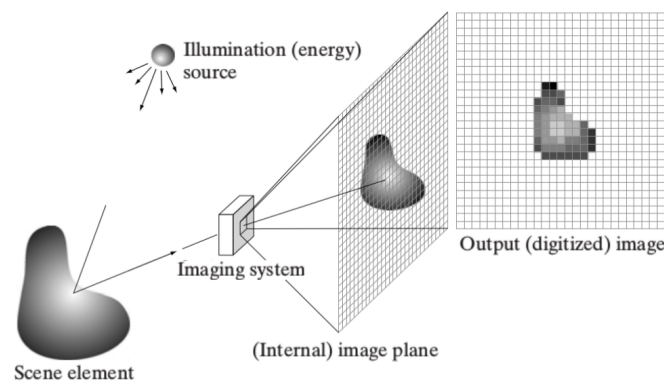


Figure 16: **Steps of digital image acquisition:** an energy source reaches the scene element, being captured by the imaging system. Within, the scene is projected onto the image plane, producing the digitized image [40].

4.2 DETECTOR IMAGE QUALITY

To evaluate how similar the acquired image is to the original scene element, a set of quantifiable parameters are discussed in this section. The indicators addressed in the following sections are characteristic of the field of radiation detection imaging and are not applicable to all kinds of imaging systems.

4.2.1 Charge gain

Charge gain is a parameter that evaluates the performance of detectors with a charge multiplication mechanism. It is defined as the ratio between the collected and the initial charge [20]. This parameter is highly dependent on the voltage applied to the different elements of the detector, as well as the gas type used as the ionization medium [3].

Charge gain is directly linked to signal-to-noise ratio (SNR), as higher gains often mean better SNR values as well as lower spatial and energy resolution values [41].

Figure 17 reflects common charge gains registered with three different GEM setups in Ar-CO₂ (70:30). It can be concluded that, by combining more GEM plates, the voltage difference needed between each foil to achieve the same charge gain is lower. Additionally, the usage of more GEM plates in a cascade setup allows the achievement of higher charge gains before the onset discharges; while, in the example shown, a single GEM does not achieve a 10³ multiplication coefficient, a factor near 10⁴ and 10⁵ is accomplished with double and triple GEM cascades, respectively.

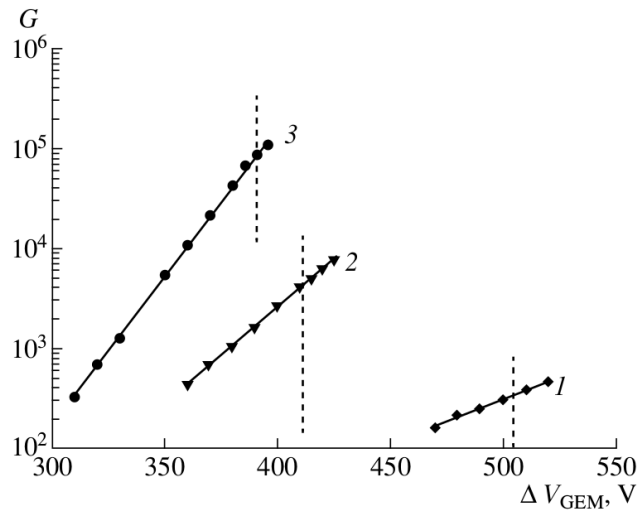


Figure 17: **Charge gains for single (1), double (2) and triple (3) GEM setup:** the charge gain, G , is represented as a function of the voltage applied to each GEM plate. These curves were obtained with a gaseous mixture of Ar-CO₂ (70:30) exposed to x-rays [30].

4.2.2 Energy resolution

When a real detector is exposed to a mono-energetic source of radiation, its response function is not a defined peak, but a distribution around the average pulse height. A wider distribution of the pulses means poorer detector performance. On the contrary, as the quality of the detector increases, the response function has smaller and smaller widths [42].

When the detector response is a normal distribution with standard deviation σ , this parameter is quantified using the definition of Full Width at Half Maximum (FWHM) described by equation 9 and depicted in figure 18.

$$\text{FWHM} = 2 \times \sqrt{2 \ln 2} \times \sigma \approx 2.355\sigma \quad (9)$$

The minimum energy value that any detector is able to resolve is equal to its value of FWHM [22].

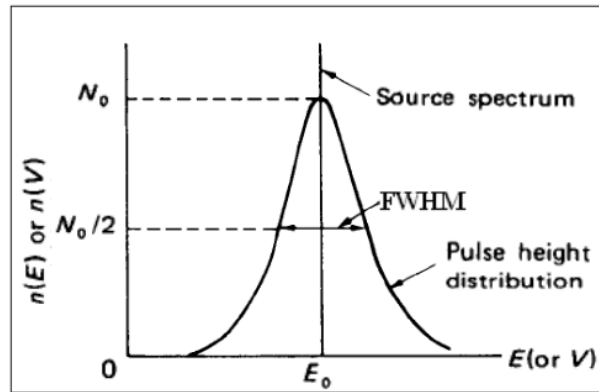


Figure 18: **Full width at half maximum:** graphically, the FWHM represents the width of the normal distribution at half its amplitude ($N_0/2$).

Energy resolution, \mathcal{R}_e , is then calculated using equation 10, being E_0 the average pulse height. This value is commonly expressed as a percentage. Smaller values mean that the detector is able to properly distinguish signals with similar energies.

$$\mathcal{R}_e = \frac{\text{FWHM}}{E_0} \times 100\% \quad (10)$$

The factors that contribute to the increase of energy resolution are many and account for random noise, statistical noise, drift of the operating characteristics of the detector and the fluctuations of the intrinsic physical effects because the detection of each charge carrier is described as a Poisson process [2].

For any gaseous detector, the minimum and ideal energy resolution, \mathcal{R}_e^{\min} , is dependent of the Fano factor (F), the w-value (w) and the incident x-ray energy (E_p) as represented in equation 11 [43].

$$\mathcal{R}_e^{\min} = 2\sqrt{\frac{2Fw \ln 2}{E_p}} \quad (11)$$

For pure krypton, Fw is known to be 5.472 eV [35] which means that, for an x-ray energy of 5.89 keV (^{55}Fe radioactive source) the minimum energy resolution that can be achieved is 7.18%. According to table 2, the minimum energy resolution expected for argon is 6.23%, which is lower than the one predicted for krypton.

4.2.3 Image signal-to-noise ratio

The signal-to-noise ratio (SNR) parameter reflects the ratio between the power of the desired data (which can be either analog or digital) and the power of the background noise. Consequently, this value is a measure of the quality of the collected data and can be associated with audio, electronic pulses, imaging and many other applications [44]. Typically, in the industrial business, it is expressed in decibels (dB), however it is also commonly represented as a percentage.

This tool is used to evaluate sets of images acquired using homogeneous materials or smaller uniform regions within a complex image. Depending on the application

and on the acquired data, the SNR can be calculated using different qualitative or quantitative definitions [45].

For imaging purposes, where data is always non-negative, the SNR is calculated by dividing the average pixel value (\bar{x}) within a ROI by the standard deviation of the pixel values (σ) in that same area. The $20 \log_{10}$ rule is then applied to convert the SNR into a dB value as shown in equation 12.

$$\text{SNR}_{\text{dB}} = 20 \times \log_{10} \left(\frac{\bar{x}}{\sigma} \right) \text{ dB} \quad (12)$$

In terms of x-ray detectors like the one developed in this work, this corresponds to the ratio between the average number of detected particles and the statistical fluctuation that occurs due to their random arrival rate, as well as the electronic fluctuations caused by the electronics. A more detailed discussion about this topic can be found in reference [46].

The SNR can then be compared with standard values to assure the quality of the acquisition. One of them is the *Rose criterion* that states that a SNR equal or above 5 or $\text{SNR}_{\text{dB}} = 13.98 \text{ dB}$ allows the successful recognition of any object [44]. A more rigorous scale (table 3) is set by the standard ISO 12232 – 2006 that applies to the branch of photography for digital still cameras.

Table 3: **SNR values imposed by the ISO 12232 – 2006 standard:** for digital still cameras, image quality can be assessed by studying its SNR value in an uniform region.

SNR	DESCRIPTION
$\dots < 20.00 \text{ dB}$	unacceptable image quality
$20.00 \text{ dB} \leq \dots < 32.04 \text{ dB}$	acceptable image quality
$\dots \geq 32.04 \text{ dB}$	excellent image quality

4.2.4 Spatial resolution

Spatial resolution is defined as the capacity to resolve fine details in a given image and is characterized by the minimum required distance between two objects for them to be distinguished by the imaging system [44].

As we can see in figure 19, when the objects are very close together (a and c), the imaging system is not able to understand the presence of both objects (b and d), as their profiles become superimposed. The minimum distance between the objects (e) that allows the perception of the two objects (f) is called spatial resolution [47].

The lower the value of position resolution, the better the imaging system is in terms of spatial feature separation.

The spatial resolution properties of an imaging system can be characterized by a set of parameters like the *point*, *line* and *edge spread functions*, as well as the *modulation transfer function* [44].

4.2.4.1 Point spread function

The *point spread function* (PSF) or *impulse response function* is defined as the response of the imaging system to an input point source. The PSF is a 2D function in the x and

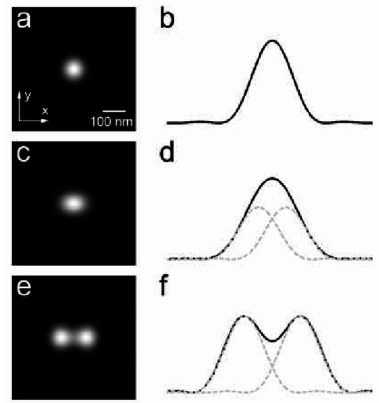


Figure 19: **Spatial resolution of a digital image:** as the distance between the objects widens (*a*, *c* and *e*), the imaging system can resolve their presence more successfully based on their profiles (*b*, *d* and *f*) [47].

y coordinates that can determine whether the system is stationary or non-stationary. In a stationary or shift invariant system, the PSF is the same along the vertical and horizontal coordinates of the system. On the contrary, a non-stationary system has a different PSF for the different image coordinates [44]. Also, when the imaging system is linear and the PSF is known, a convolution ($*$) with the input image gives the output image [48], as depicted in figure 20.

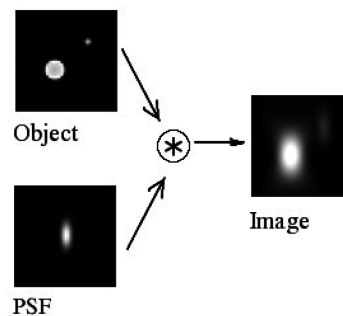


Figure 20: **Characteristics of the point spread function:** knowing the impulse response of the imaging system and the input image, the output image can be calculated using the convolution operation [48].

To obtain the PSF of an imaging system based on radiation detectors, a collimator is needed to mask the x-ray source into a dimensionless point, which is experimentally impossible. Because of this, the direct measurement of the PSF for position resolution determination is not very common. Furthermore, a satisfactory high exposure image is needed to guarantee adequate statistics [44].

4.2.4.2 Line spread function

The *line spread function* (LSF) is the imaging system's response to a line stimuli; using x-rays, a mask in the form of a narrow slit is usually used to produce the adequate input. The image is then profiled in a direction perpendicular to the line direction and its area is normalized [44]. However, as the slit possesses a finite width, a deconvolution between the LSF and the rectangular input should be performed to allow correct position resolution determination.

The LSF can be understood as the 2D representation of the PSF or even as the integration of the PSF along the line coordinates. This is true because a line can be seen as the summation of infinite points along its length. Therefore, the LSF can be mathematically determined from the PSF [4] using equations 13 and 14.

$$LSF(x) = \int_{-\infty}^{+\infty} PSF(x, y) dy \tag{13}$$

$$LSF(x) = PSF(x, y) * LINE(y) \tag{14}$$

The thinner the LSF, the better the spatial resolution of the system is [44]. An example of a LSF (c) of an image (a) is shown in figure 21 [49].

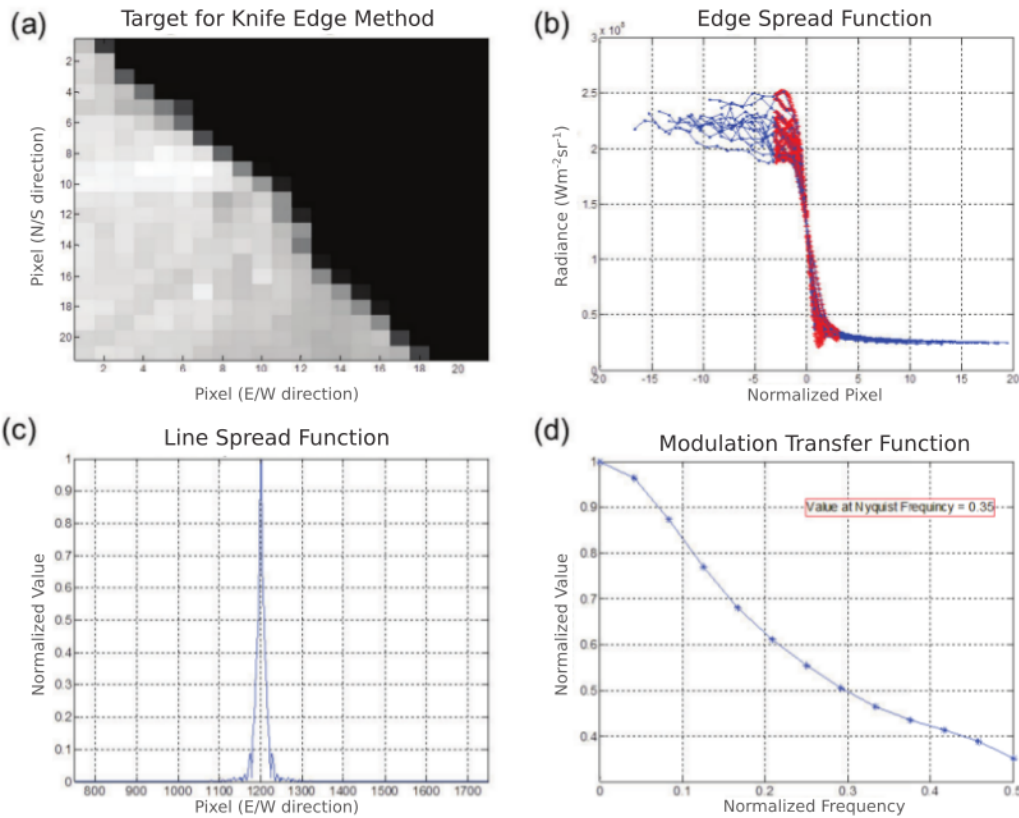


Figure 21: Line (c), edge (b) and modulation (d) transfer functions of a digital image (a): the processed image represents a section of the coastal line of the Korean peninsula used in satellite imaging applications. Adapted from [49].

4.2.4.3 Edge spread function

The *edge spread function* (ESF) is used for images where the PSF and LSF can't be applied. In this case, the presence of a sharp edge is needed. The ESF corresponds to the edge gradient of the image and commonly has the profile shown in figure 21-(b) [44].

An ideal edge has its discontinuity represented by the Heaviside step function (equation 15 where a is the position of the discontinuity). However, the measurement process is not able to reproduce this profile because of the imaging system's limitations [50].

$$H(x) = \begin{cases} 1, & \text{if } x > a \\ 1/2, & \text{if } x = a \\ 0, & \text{if } x < a \end{cases} \quad (15)$$

A line is known to be the first derivative of an edge, so the LSF can be obtained from the ESF by differentiation [4]. Furthermore, if the LSF is a normal distribution (very common radiation detector imaging), the ESF adopts the profile of a complementary gauss error function defined by equation 16 [50].

$$\text{erfc}(z) = 1 - \frac{2}{\sqrt{\pi}} \int_0^z e^{-t^2} dt \quad (16)$$

Sharp descents in the ESF mean that the edge quickly progresses from one medium to the other in terms of position coordinates. This means that the image discontinuities are well defined and the image contours allow good object resolving.

The ESF can be determined from the PSF and the LSF using equations 17 and 18 [44].

$$\text{ESF}(x) = \text{PSF}(x, y) * \text{EDGE}(y) \quad (17)$$

$$\text{ESF}(x) = \int_{-\infty}^{x'} \text{LSF}(x) dx \quad (18)$$

4.2.4.4 Modulation transfer function

The *modulation transfer function* is commonly used to evaluate the quality of any imaging system or device in terms of contrast response to spatial frequency [51].

When an imaging system receives a sum of different sinusoidal wave inputs, the system is able to replicate the received frequencies¹, but with different contrasts. This is the consequence of spatial resolution loss, which means that the image contrast is dependent on the spatial frequency of the objects [44]. This effect can be observed in figure 21-(d); for higher frequencies (horizontal axis), the image contrast (vertical axis) reduces significantly, which is a common result.

In experimental conditions, the MTF is not easily measured so the normalized LSF is used to infer its profile using the Fourier transform, which is illustrated in equation 19.

$$\text{MTF}(f) = \left| \int_{-\infty}^{+\infty} \text{LSF}(x) e^{-2\pi i f x} dx \right| \quad (19)$$

The limiting spatial resolution is defined as the frequency at which the MTF drops below a certain value in percentage (typically agreed upon 10%) [44].

4.2.5 Position resolution limitations

Spatial resolution is influenced by many physical and experimental factors like the gas medium or the intrinsic resolution of the electronic system. For the scope of this

¹ only if the frequency is lower than the Nyquist frequency

work, only some will be discussed, like the *signal-to-noise ratio*, *photoelectron range*, *magnification* and *distortion*.

Figure 22 depicts a typical curve of position resolution for most noble gases as a function of the incoming x-ray energy. The degradation of position resolution observable for low and high values of x-ray energy occurs because of the *signal-to-noise ratio* and the *photoelectron range* effect, respectively.

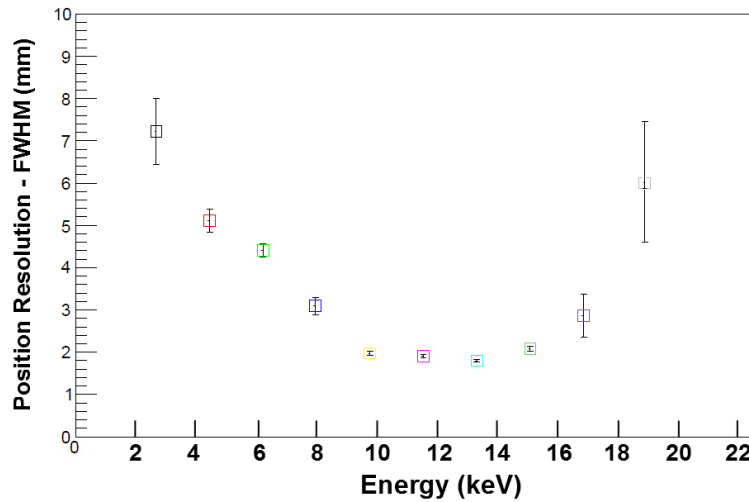


Figure 22: **Position resolution as a function of x-ray energy:** it is noticeable that, for both low and high radiation energies, the position resolution worsens because of *signal-to-noise ratio* and *photoelectron range*, respectively. These values were measured for an Ar-CO₂ (70:30) mixture [4].

4.2.5.1 Photoelectron range

Because electrons have comparable masses to the other particles they are interacting with (orbital electrons), they suffer very abrupt energy losses, affecting the overall *electron range*. This phenomena greatly influences the position resolution of a gaseous imaging system [2].

When a *photoelectron* is emitted from an excited atom with a low value of kinetic energy, the electron is rapidly stopped by the medium, resulting in a primary electronic cloud formation very close to the point of interaction. However, as the x-ray energy increases, so does the kinetic energy of the free electrons, increasing their range. This means that the primary electronic cloud will be formed further from the point of interaction, deteriorating the value of position resolution [52].

The spatial resolution value can be improved by using a denser gas medium, as they prevent the increase of *photoelectron range* [22].

4.2.5.2 Electronic signal-to-noise ratio

When using a resistive strip to apply the charge division principle, the ratio of the charge collected at the left, Q_L , and right, Q_R , side of the strip is equal to the inverse of the ratio of the strip resistances between the avalanche point and the strip tips as shown in equation 20. This quantity is here corrected by the addition of the input impedance of the preamplifiers. The schematic that illustrates this assumption is presented in figure 23.

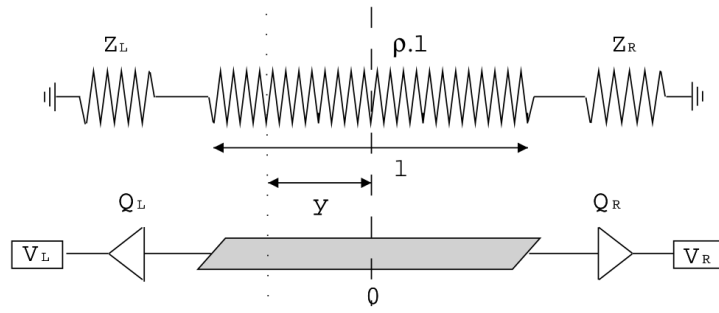


Figure 23: **Resistive charge division:** Z_R and Z_L are the input impedances of the preamplifiers and Q_R , Q_L are the correspondent collected charge. Quantity l is the length of the resistive strip, ρ its resistivity and y is the distance from the interaction position to the middle of the strip [53].

$$\frac{Q_L}{Q_R} = \frac{(l/2 - y)\rho + Z_R}{(l/2 + y)\rho + Z_L} \quad (20)$$

Solving the previous equation in order to the avalanche position, y , and accounting that $R = \rho l$ is the total resistance per unit area, we obtain equation 21.

$$y = \frac{l}{2} \left(\frac{Q_R - Q_L}{Q_L + Q_R} \right) + \frac{l}{R} \left(\frac{Q_R Z_R - Q_L Z_L}{Q_L + Q_R} \right) \quad (21)$$

Assuming the preamplifiers have the same input impedance, Z , the latter equation can be rewritten as equation 22.

$$y = \frac{l}{2} \left(\frac{Q_R - Q_L}{Q_R + Q_L} \right) \left(1 + \frac{2Z}{R} \right) \quad (22)$$

From this equation, position resolution can be defined as the standard deviation of the coordinate y , calculated using the standard error propagation formula (equation 23), and assuming that the equivalent noise charges $\delta_{Q_L} = \delta_{Q_R} = \delta_Q$ are identical and non-correlated. At the middle of the strip, where $Q = Q_L = Q_R$ we obtain equation 24.

$$\delta_y = \sqrt{\left(\frac{\partial y}{\partial Q_L} \delta_{Q_L} \right)^2 + \left(\frac{\partial y}{\partial Q_R} \delta_{Q_R} \right)^2} \quad (23)$$

$$\delta_y = \frac{l}{2\sqrt{2}} \left(1 + \frac{2Z}{R} \right) \frac{\delta_Q}{Q} \quad (24)$$

where Q represents the signal and δ_Q the noise.

This means that the position resolution is inversely proportional to the electronic's SNR. Therefore, to achieve better position resolution (lower δ_y), higher values of SNR must be obtained. High SNRs are known to be associated with higher incoming x-ray energy and values of charge gain, while for low energies and small multiplication coefficients, noise overcomes the signal, affecting the value of position resolution [53].

4.2.5.3 Magnification

Magnification is also known to degrade the overall position resolution as it adds extra uncertainty to the photon's trajectory.

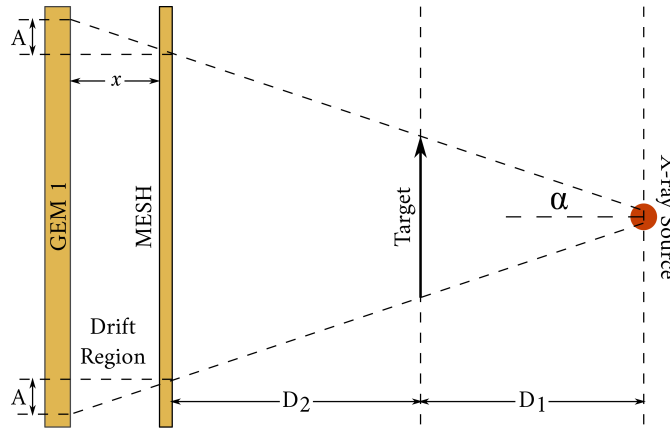


Figure 24: **Image magnification and uncertainty:** x is the length of the drift region, D_1 is the distance between the target and the x-ray source while D_2 is the distance between the target and the cathode mesh. The higher the value of D_2 , the higher is the uncertainty \mathcal{A} imposed in the acquired images.

The magnification, \mathcal{M} , of an optical system depends on the target positioning relative to the detector, D_2 , and to the x-ray source, D_1 , and is calculated using equation 25.

$$\mathcal{M} = \frac{D_1 + D_2}{D_1} \quad (25)$$

When the magnification is different from the unity, the uncertainty of the image grows by an amount \mathcal{A} , which is related to the drift region length and the angle α defined in figure 24, according to equation 26.

$$\mathcal{A} = x \tan \alpha \quad (26)$$

Uncertainty in the overall acquisition is guaranteed to be minimized when the target is close to the cathode ($D_2 \approx 0$), setting the magnification closer to the unity. When this happens, angle α is smaller, implying that the uncertainty \mathcal{A} is also reduced.

4.2.5.4 Distortion

Another factor that may jeopardize the spatial resolution measurement is image distortion that appears as a consequence of experimental conditions and the reconstruction algorithms combined. Ideally, the distances within the reconstructed image are proportional to the distances within the real object they represent. Whenever this proportionality constant is not the same throughout the entire image area, *distortion* is said to occur. Consequently, a non-uniform imaging system implicates an error in coordinate representation which affects all distance measurements applied to the final image [54].

Consequently, it is of importance to evaluate and quantify the distortion of a certain imaging system. This characterization is often made by imaging a known-dimension mask and plotting the point locations as a function of their real position within the

imaged object. This distribution should resemble a straight line and a linear regression enables the calculation of the *integral nonlinearity* (INL), which is the average of the absolute distance between each point and the fitted function. The smaller the value of the INL, the better the imaging system behaves in terms of distortion [54].

CHAPTER OVERVIEW

The most relevant parameters used to characterize detector performance in terms of imaging acquisition are *charge gain*, *energy resolution*, SNR and *position resolution*. While charge gain is related to the multiplication mechanism that takes place inside the detector, the energy resolution evaluates the detector's response to a mono-energetic source. Image signal-to-noise ratio is a measurement on how the measured data surpasses the intrinsic noise present in the final image.

Spatial resolution quantifies the minimum required distance between two objects for the image system to be able to distinguish them. This parameter can be determined by three different profiles, being them the PSF, the LSF and the ESF. Also, the MTF characterizes how the contrast response behaves with increasing spatial frequency.

Position resolution can be limited by physical and experimental conditions; while *photoelectron range* degrades the position resolution for more energetic radiation, the electronic SNR contribution is most noticeable for low x-ray energies.

The positioning of the target within the detection system is also fundamental to avoid the addition of extra uncertainty during image formation. Furthermore, the distortion effects should be quantified to evaluate the quality of the imaging system and account for the correspondent errors during the image reconstruction process.

Part II
EXPERIMENTAL SETUP

SYSTEM DESCRIPTION

This chapter describes the organization and operation of the experimental system, focusing on the x-ray source, gas flow control and the electronic system used for the optimization and the imaging studies.

5.1 SYSTEM OVERVIEW

As it is depicted in figure 25, the experimental setup was composed by the following elements:

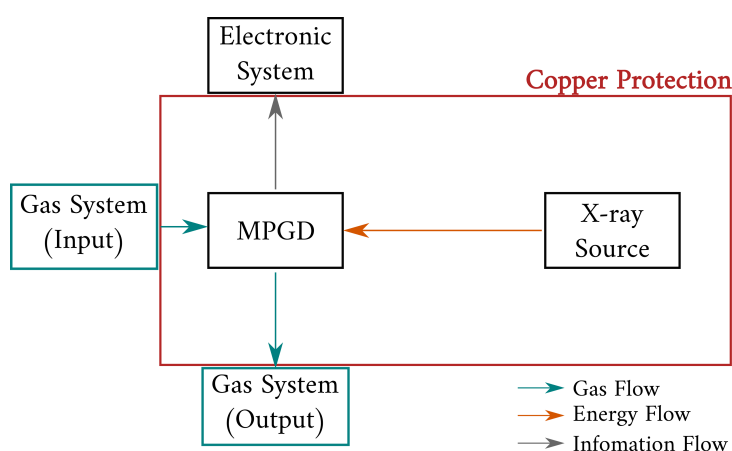


Figure 25: **Block diagram of the experimental system:** its main constituents were the MPG, the x-ray source, the gas system and electronic system which established the energy, gas, and information flows, respectively.

- **X-ray source:** it was responsible for providing the necessary energy (in the form of a photon beam) to ionize the gas flowing through the detector. For most of the imaging studies, an absorbent mask was used between the x-ray source and the detector to spatially select the incoming radiation by beam attenuation;
- **MPGD:** the gaseous detector was responsible for converting the incoming (sometimes masked) radiation into a measurable electronic signal. Because of its complexity and importance for this work, the elements that constituted the MPG will be fully described in the following chapter;
- **Electronic system:** physically connected to the detector, the electronic system amplified, processed and digitized the incoming electronic signal. The last stage of this block was a laboratory computer where the binary information files were stored in memory;
- **Gas system:** also physically connected to the MPG, the gas system stored, mixed and controlled a constant flow of the selected gas mixture. It was also responsible for guiding the gas flow through the MPG and then expelling it into the surrounding atmosphere.

For security reasons, both the MPGD and the x-ray source were enclosed in a copper box to protect the users from the radiation doses produced by the x-ray generator.

Each one of these blocks and its constituents will be further described throughout the following sections.

5.2 X-RAY SOURCE

The x-ray source used in this work was not maintained throughout the experiments; while a ^{55}Fe radioactive source was used for the optimization and calibration of the detector, an x-ray generator was used more consistently during image acquisition.

5.2.1 Radioactive ^{55}Fe source

The radioactive ^{55}Fe source makes use of the electron capture decay process which produces ^{55}Mn and soft x-rays. This decay process has a half-life of 2.737 years and is described in equation 27.



Table 4 shows the most probable transitions and the correspondent energies [55]. The K_{α} transitions have very similar energies and common detectors cannot distinguish them, so it is often said that mono-energetic x-rays of 5.89 keV with 24.4% probability are produced [42]. Consequently, it is expected a K_{β} energy peak about nine times smaller than the one correspondent to the K_{α} line.

Table 4: **Characteristic x-rays of a ^{55}Fe source:** for the dominant transitions, the correspondent energy and probability are presented [55].

TRANSITION	ENERGY (keV)	PROBABILITY
K_{α_1}	5.89875	16.2%
K_{α_2}	5.88765	8.2%
K_{β}	6.49045	2.85%

5.2.2 X-ray generator

The x-ray tube used in this work belongs to the Series 5000 Apogee from Oxford Instruments[®], with a stability of 0.2% over 4 hours. This apparatus has a 0.127 mm beryllium window, an anode current up to 1.0 mA and a maximum anode voltage of 50 kV [56].

5.3 GAS SYSTEM

For this work, a gas system with continuous flow was chosen over a sealed environment as it presented itself as a more adequate alternative for the studies that were made.

While a continuous gas flow is able to keep the gas purity for much longer (as there is a constant renovation of the medium), in a sealed detector a purifier must

be used to remove the oxygen molecules as well as other electronegative impurities. These last systems are also more subjected to gas aging effects [22]. Furthermore, as studies about a wide variety of gas mixtures were in order, changing the gas medium inside the detector should be an easy and fast procedure, which could only be assured with a renewable gas system. Actually, the experimental system allowed the usage of a different gas mixture every day, with the sole inconvenience of letting the desired mixture run for at least five hours before the beginning of the measurements.

One of the major disadvantages of using a continuous flow system is the operational cost, as a bigger gas supply and an exhausting system are indispensable. The gas flow imposed was 2.0 L h^{-1} as previous works established this value as the minimum gas flow that ensured optimum operational conditions. This value was imposed to ensure an exchange rate of one gas volume each two hours at a small, stable, laminar flow.

The gas system used throughout this project was composed by two gas bottles (Kr and CO_2), two mass flux controllers connected by a "T" junction to regulate their proportions and an exit filter, all connected by sealed tubes to prevent leaks. Figure 26 shows the layout of the gas system.

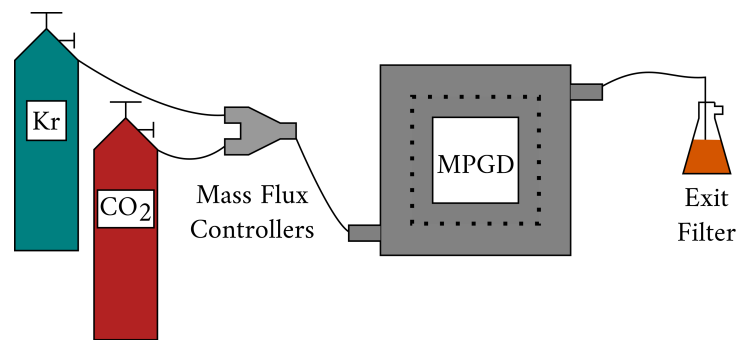


Figure 26: **Schematics of the gas system:** the gases are mixed by the mass flux controllers and guided through the detector, exiting the system through an oil-filled container.

Carbon dioxide was mixed with krypton for two reasons:

1. **Price:** krypton is an expensive gas when compared to carbon dioxide. Consequently, by adding CO_2 , the cost of each image acquisition decreases.
2. **Positive reinforcement:** noble gases are known to emit ultraviolet radiation during the de-excitation process which can produce new avalanches within the detector, compromising the proportionality between the radiation energy and the collected charge. As a consequence, the usage of krypton alone may cause non-linear effects, which influences the detector's performance by corrupting the measured signal. The addition of a light molecular gas such as CO_2 is often made to absorb this secondary ionization and increase the charge gain, restoring the system's linearity. This methodology is denominated as *quenching of UV* [29].

5.3.1 Gas containers

The three gas containers were provided by Praxair® and shipped from Madrid, Spain. The Ar- CO_2 (70:30) canister was the same as the one used in [4], being 30.05% of carbon dioxide and 69.95% of argon. The krypton container was filled with Kr-5.0, which dictates a concentration of, at least, 99.999%. The pure CO_2 bottle (used to produce the Kr- CO_2 mixtures) had a concentration of 99.9%.

5.3.2 Mass flux controllers

The mass flux controllers used (one for krypton and other for CO₂ control) belong to the series EL-FLOW Prestige[®] and were manufactured by Bronkhorst[®]. This instrument uses thermal bypass sensor technology to measure and control the intended gas flow in a pressurized system. Also, the system provides high precision control because the user is able to chose the desired gas species. The gases used in this work are dry and had high purity indexes with low chance of condensation, so the gas control process was not compromised [57].

5.3.3 Detector connection

Between experiments and every time the detector's chamber was opened, air penetrated inside the detection chamber, compromising the experimental results. So, in order to guarantee the gas purity, all the residual air was expelled before measurements were performed. To achieve this, a steady gas flow of the desired mixture ran through the detector for a minimum of five hours before the measurements began. Also, knowing that the krypton mixtures used in this work are more dense than the atmospheric air (according to table 5), the input tube was placed lower than the output tube (as shown in figure 26) to push the air out of the detector more efficiently.

Table 5: **Density of different Kr-CO₂ mixtures:** all the mixtures used are heavier than air (these values refer to NTP conditions) [58].

	AIR	Kr	CO ₂	Kr-CO ₂ (60 : 40)
DENSITY (kg/m ³)	1.292	3.748	1.9763	3.039

5.3.4 Exit filter

Before entering the atmosphere, the gas that exited the detector was conducted by a tube into a glass container filled with oil. This mechanism prevented air entrance into the gas system. Also, it allowed manual pressure regulation which is dependent on how much the tube was dipped within the oil. The pressure inside the detector can be related to the atmospheric pressure, P_{atm} , by equation 28.

$$P_{detector} = P_{atm} + \rho gh \quad (28)$$

where ρ is the oil density ($\approx 0.9 \text{ g/cm}^3$), g is the acceleration of gravity and h is the length of the exit tube that is dipped into the oil ($\approx 0.5 \text{ cm}$). According to these dimensions, the pressure imposed inside the detector is very close to P_{atm} .

A steady bubble flow visible in the oil also ensured that the gas mixtures were successfully running through the system.

5.4 ELECTRONIC SYSTEM

Throughout the entire course of the experimental studies, the detector was operated under the pulse mode to allow the recording of information relative to each incoming radiation *quantum*.

Two electronic setups were installed during the course of the project: for optimization and calibration purposes, a 1D information channel system for energy recording was used; while for image acquisition a 4D channel system was necessary to resolve the spatial information.

5.4.1 Optimization studies

During optimization and detector calibration no position information was needed, only the sum of the energy collected by the readout plate. Therefore, the output channels of the readout foil were short-circuited and the resulting signal was then processed by the instruments depicted in figure 27.

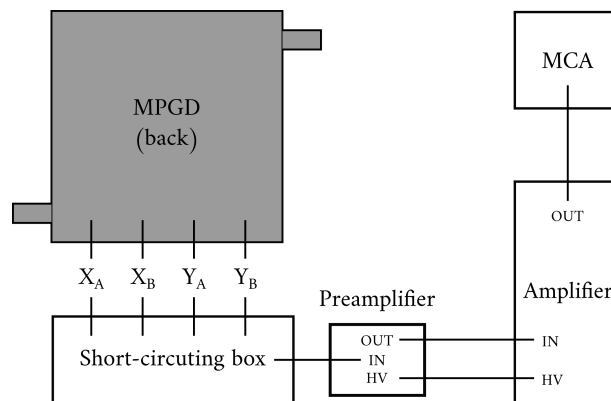


Figure 27: **Electronic system setup used for the optimization studies:** the four information channels (X_A , X_B , Y_A and Y_B) were short circuited. The signal was then processed firstly by a preamplifier and then by an amplifier before reaching the MCA for data digitization and representation.

BNC cables were used to guide the electric signal throughout the different apparatus.

5.4.1.1 Charge-sensitive preamplifier

The charge-sensitive preamplifier used in the setup was a Model-2004 developed by Canberra[®]. This device converts the incoming charge carriers produced in the detector into a step function voltage pulse as shown in figure 28. This conversion occurs as the first stage of the apparatus acts as an operational integrator over the accumulated charge. The amplitude of this pulse is proportional to the total collected charge and decayed with a nominal time constant of $50 \mu\text{s}$ [59].

Ideally, the output signal has a small rise time and a long decay time ($50 - 100 \mu\text{s}$) to decrease noise influences. However, bigger values of decay time also increase the probability of event pile-up which can negatively influence the measurement process.

5.4.1.2 Shaping amplifier

A Tennelec (TC-243) shaping amplifier was connected to the preamplifier and configured with a peaking time of $4 \mu\text{s}$. This device assures that the ADC is capable of detecting the peak with sufficient precision by shaping the incoming signal as a quasi-Gaussian (figure 28). The signal height is kept, so the amplitude continues to be proportional to the event energy. After the signal maximum, the baseline should be

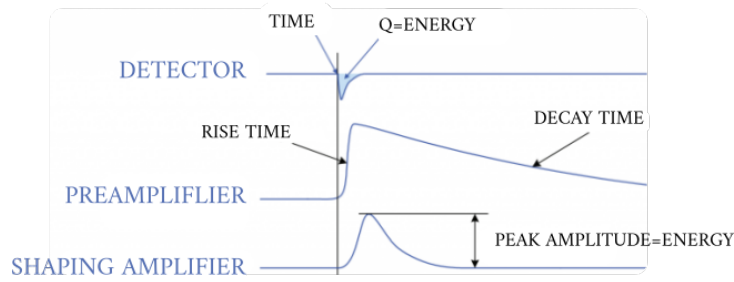


Figure 28: **Electric signals along the electronic system:** the detector output signal is converted firstly into a step function voltage pulse and then into a quasi-Gaussian [60].

rapidly established to avoid pulse overlapping. The amplifier is also responsible for filtering high and low-frequency noise to increase the SNR [2].

5.4.1.3 Multi-channel analyzer

The Multi-Channel Analyzer (MCA) used was a Nucleus-PCA embed in a lab computer. This apparatus allowed signal digitization, representation and storage in the form of an energy spectrum. The signals were read with the Maestro software. The information files were analyzed using the Ajusto software, which is a homemade tool commonly used at GIAN.

5.4.2 Imaging studies

For the imaging studies, the four channels were analyzed by the electronics separately to record the interaction position information. The signals were then digitalized and the correspondent information was stored in a computer, as depicted in figure 29.

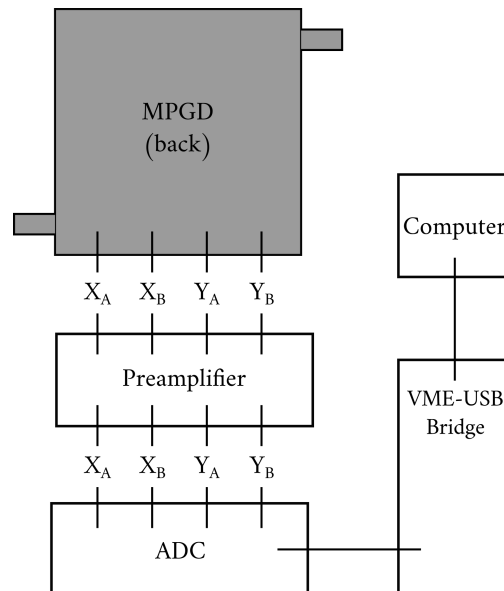


Figure 29: **Electronic system setup used for the imaging studies:** the four channels (X_A , X_B , Y_A and Y_B) were amplified and digitized separately. The information was then recorded in a laboratory computer.

5.4.2.1 8 channel preamplifier

The charge-sensitive preamplifier is able to individually process the signal from 8 input channels, applying a rise time of $10\ \mu\text{s}$. For the purpose of this work, only four channels were used to handle the X_A , X_B , Y_A and Y_B signals.

5.4.2.2 ADC and bridge

The ADC used was a CAEN Mod.V1724, with 14 bit resolution and 8 input channels available. This module was connected to a CAEN V1718, which is a USB-VME bridge. This module allows data recording in the laboratory computer in the form of four binary .dat files, correspondent to the four channels of the readout board. Each file line has the time stamp and the measured signal amplitude for each candidate event.

The signals were collected and processed in real time using the DPP-PHA Control Software. Conventional equipments treat the input signal analogically, digitizing the signal only at the end of the processing chain. CAEN makes use of a digital approach, converting the input signal at the beginning, and then applying analogous digital operations. Digital processing allows higher stability, reproducibility, personalization of the processing algorithms, information preservation along the processing chain, pile-up reduction, among other advantages. The main steps used in this approach, are represented in figure 30 [61].

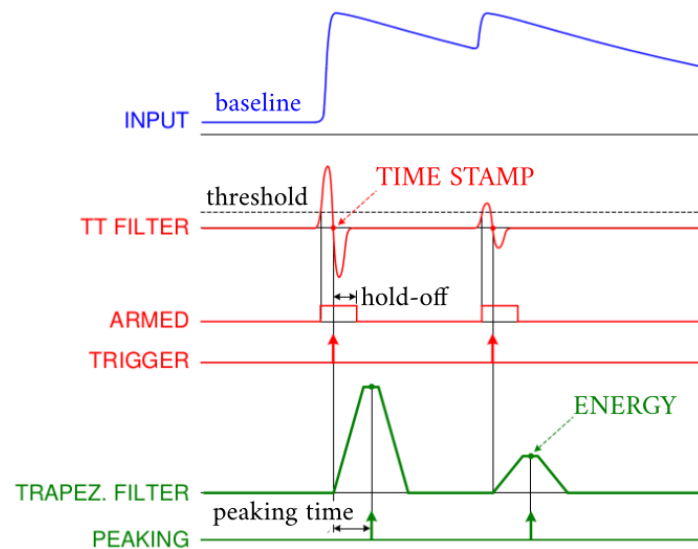


Figure 30: **Signal processing using the CAEN digital approach:** the input signal from the amplifier (blue) is digitized first, then passing through a *trigger and timing filter* (red) and a *trapezoidal filter* (green) [61].

The signal inputted by an external preamplifier (blue) is immediately digitized. The signal then passes through a *trigger and timing filter*, which is responsible for identifying the incoming pulses, triggering and calculating their time stamp. A *trapezoidal filter* then shapes the signal into a trapezoid with amplitude proportional to the energy of the corresponding signal. The flat top of the trapezoid provides a time interval where its correspondent amplitude can be determined with precision [61].

CHAPTER OVERVIEW

The detector system can be divided in three main modules (not counting the detector itself). The first one is composed by the x-ray source, which generates the x-rays necessary for gas ionization.

The gas system is responsible for flowing the gaseous mixture at a constant rate inside a sealed system from the gas container, through the detector and into the atmosphere.

The electronic system carries, amplifies, processes and digitizes the electronic signals provided by the detector. For the image analysis, the electronics was connected to a laboratory computer, saving four data files, correspondent to each channel of the readout plate. For the optimization studies, the end of the electronic system was a real-time MCA for spectra visualization.

DETECTOR DESCRIPTION

This chapter describes the layout of the detector used throughout the project as well as its elements and their operation mode.

6.1 DETECTOR CONFIGURATION

The method of using multiple G-100 foils in a cascade layout to increase the overall charge gain was applied to the construction of the MPGD. Two consecutive G-100 plates were placed between the mesh and the readout board according to the schematics presented in figure 31. The different structures were separated and supported by a group of four teflon pillars with the specified heights.

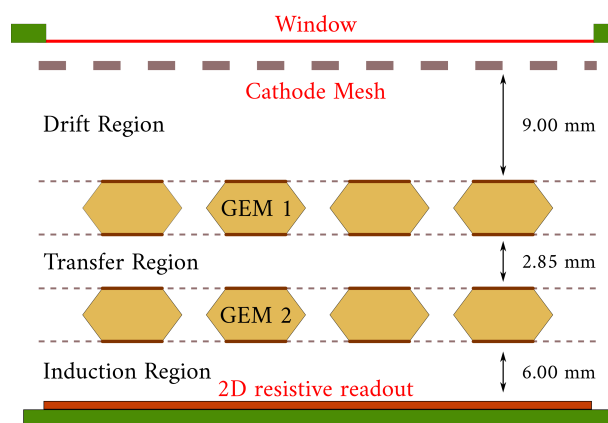


Figure 31: **Configuration of the G-100-based MPGD:** a cascade setup provided two multiplication stages while a metallic mesh limited the drift region.

The elements of the detection system had an active area of $10 \times 10 \text{ cm}^2$ and were independently biased with negative voltages, except for the readout plate, which was connected to the ground frame. This decision was made because the preamplifier connected to the readout board required a ground connection. With this configuration, the free electrons created during the ionization process were successfully guided through three distinct regions of space:

- **Drift Region:** being 9.00 mm deep, is where the primary electron cloud is produced. The free electrons are then guided to the multiplication region (top of the first G-100) by the means of the imposed electric field. During their transportation, recombination should be avoided by applying higher voltage differences. However, high electric fields may lead to the loss of charge carriers as they can become trapped at the top of the first GEM, so an equilibrium should be found;
- **Transfer Region:** this region is 2.85 mm deep and plays a decisive role in the extraction of the charge from the holes of the first G-100 and in electron focusing into the holes of the second one [4]. The requirements for these two actions are opposite: while a large transfer field is required for adequate electron-focusing, increasing the transfer field may lead to electron accumulation at the top electrode of the second G-100, reducing the overall gain of the cascade;

- **Induction Region:** a strong field is required to detach electrons from the bottom of the second G-100 and guide them towards the readout board where the electric signal will be measured;

There is also an electric field applied between the electrodes of each G-100 plate to allow charge multiplication. Here, the maximum electric field possible is required to maximize electron multiplication and guarantee stronger signals. However, very high electric fields may cause sparking that lead to structure damaging.

Another factor that should be taken into account is the separation between the place where the primary electron cloud is formed and the region for charge multiplication. This physical detachment guarantees that every charge carrier is amplified in an uniform manner [22].

6.2 GASEOUS CHAMBER

The detector housing (figure 32) was made of stainless steel and had a volume of $(25 \times 25 \times 6) \text{ cm}^3$. A $25 \mu\text{m}$ thick entrance window of aluminized Mylar™ allowed the passage of x-rays, also keeping the gas mixture inside the chamber. A robust structure and rigorous setup was necessary to prevent leaks like gas escape, pressure loss or atmospheric air entrance. On the other hand, the material of the window is known to be optically opaque to prevent the entrance of visible and ultraviolet radiation that may induce electron emission within the gas medium and lead to spurious signals.

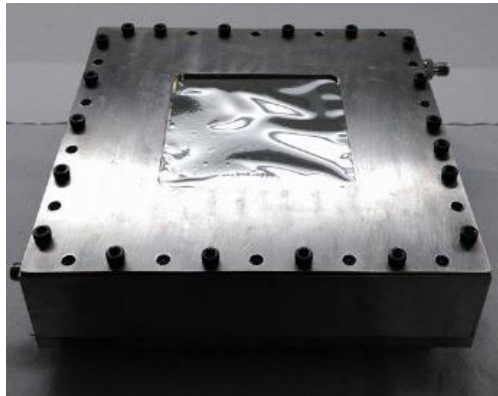


Figure 32: **Gaseous chamber:** made of stainless steel, the detector housing prevents gas exchange between the inside volume and the outside environment [4].

6.3 CATHODE MESH

The cathode mesh is a metallic electrode that was responsible of limiting the drift region. It was made from a $80 \mu\text{m}$ diameter stainless-steel wire with a spacing of $900 \mu\text{m}$.

6.4 G-100 PLATES

The characteristics of these plates were already discussed in section 3.4.1.3. A cascade setup of two G-100 plates was implemented to increase the charge gain of the system and strengthen the overall output signal. Figure 33 shows the inside of the de-

tector and the positioning of the top G-100 plate with the necessary wiring for biasing and output signal collection.

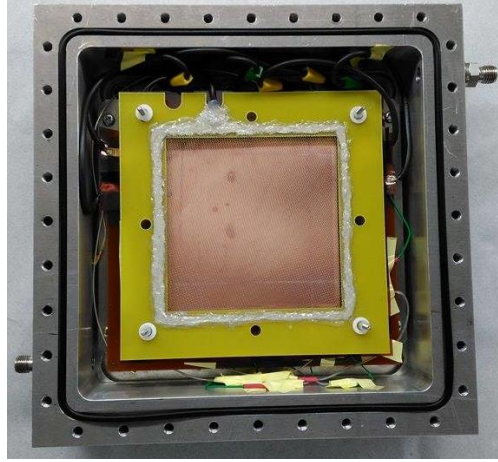


Figure 33: **Assembly of the G-100 plates:** the use of non-standard, 100 μm thick GEM plates determined a more robust and sparking-tolerating detection system [4].

The addition of more than two G-100 foils could increase even more the gain of the detection system and lower the voltage across each G-100 element, thus reducing the chances of discharges. However, the setup of the detector would be more complex and electronic issues could arise. If more structures were added to the setup, the total voltage needed to polarize the entire system would be much higher. Because the adopted polarization scheme (figure 31) kept the anode at ground, the highest applied voltage was located in the cathode mesh. As the mesh was placed close to the detector window, insulation problems could occur. Weighting all these factors, it was agreed to use a cascade of only two G-100 foils.

6.5 READOUT BOARD

Two orthogonal sets of conductive strips (with 200 μm pitch), where each direction was connected to a separate resistive line ($\approx 5 \text{ k}\Omega$) composed the 2D readout board. This arrangement allowed the recording of the interaction position and the correspondent deposited energy. This structure had an active area of $10 \times 10 \text{ cm}^2$.

The charge pulses created in the surface of the readout plate during electron arrival are divided according to the principle of the resistive charge division, codifying the event position and the correspondent energy. Four output channels (X_A , X_B , Y_A and Y_B), placed at the ends of each resistive line collected the necessary information for image reconstruction [4]. This process is illustrated in figure 34.

To calculate the position of each recorded event, equations 29 are usually applied [22].

$$x = \frac{X_A - X_B}{X_A + X_B} \times L \quad y = \frac{Y_A - Y_B}{Y_A + Y_B} \times L \quad (29)$$

where L is a calibration factor and X_A , X_B , Y_A and Y_B represent the signal amplitudes at the end of the resistive line. The total energy of the interaction, E_T is proportional to the sum of the four readout terminal signals, where its coefficient can be determined by calibrating the imaging system. This kind of readout assures a *quantum particle detector*, as it retains the (x, y, E_T) information for each incoming particle [54].

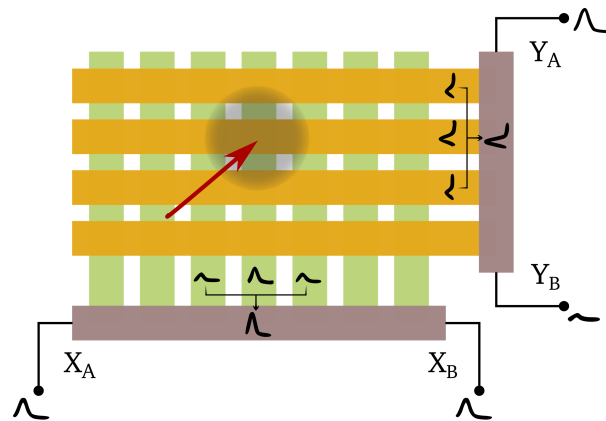


Figure 34: **Schematics of the 2D resistive readout:** the two perpendicular sets conductive strips (yellow and green), each connected by a resistive line (gray) allow position and event energy recording by collecting the charge from the second G-100 plate.

Many imaging systems use pixel-based readouts where each element constitutes an isolated electronic channel because these sensors have better spatial resolution and are less subjected to distortion. However, the number of pixels is known to grow exponentially with the total area of the readout, quickly adding complexity to the overall imaging system. Furthermore, the growth of electronic channels implies a stronger processing effort, both by the electronics and the reconstruction software. Consequently, a four-channel readout is a simple, low cost and reliable system capable of recording the necessary information for imaging applications.

6.6 STRUCTURE BIASING APPARATUS

A CAEN Mod.V6521HN power supply with a current limitation of 100 nA was used to enforce the desired voltages to the electrodes of the detector. Each power line was then filtered using a custom-made low pass filter with a RC constant of 20 ms to assure stable polarization conditions. The input voltages were controlled using the correspondent CAEN software, which returns the board real-time status.

CHAPTER OVERVIEW

The detector is divided into three distinct regions, according to the physical phenomena they enforce and which are physically separated by the detector's structures. The gas molecules are ionized by the x-rays, producing heavy ions and free electrons in the drift region. The electrons are guided to the first G-100 plate where multiplication occurs. In the transfer region, the resulting electrons are directed towards the second G-100 foil where a second charge multiplication occurs. Finally, the induction region assures the collection of the electrons by the readout board, producing a measurable electronic signal.

AUXILIARY MATERIAL

This chapter describes the most relevant aspects of the auxiliary material used as imaging masks with the objective of evaluating the system's capabilities. These objects possessed distinct shapes and x-ray transparencies to allow both qualitative and quantitative characterization of the imaging system. Their contributions to the measurements are discussed, as well as the conditions that assure their proper usage.

7.1 MTF MASK

A 0.05 mm thick lead mask was used to estimate the MTF of the imaging system. As seen in figure 35, twenty six sets of three x-ray-transparent slits with variable spacing allow the characterization of contrast for different spatial frequencies. This line pitch is quantified in line-pairs per millimeter (lp/mm) .



Figure 35: **MTF mask used as an imaging target:** this mask was made of 0.05 mm thick lead. Sets of three slits with variable separation (in lp/mm) allow the MTF estimation.

The maximum value in lp/mm for which the three slits are visually distinguished is an estimation of the systems' MTF function close to 3% intensity [22].

Knowing the thickness of the mask and using the information presented in [62], equation 3 may be applied to determine which x-ray energies are completely attenuated by the lead mask. Figure 36 shows the attenuation curves for the x-ray energies of 16, 20, 30 and 40 keV. The thickness of the lead mask is represented by the dotted black line.

The figure shows that 20 keV x-rays (red) are almost totally attenuated by the lead mask. When 30 keV photons are used (blue), about 80% of the x-rays are still absorbed by the mask. However, for 40 keV x-rays, more than 40% of the photons can penetrate the lead mask, lowering the contrast of the output image. This response curves demonstrate that, during image acquisition, the x-ray energy should not surpass 40 keV, or the image of the MTF mask loses the necessary contrast for correct image analysis.

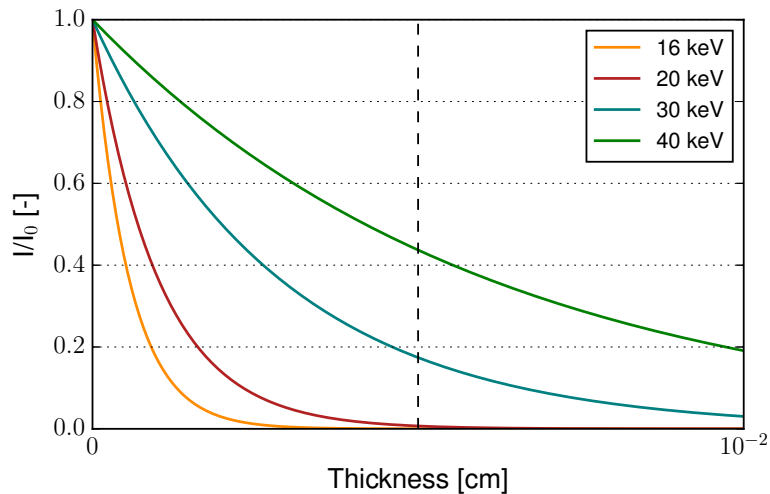


Figure 36: **Lead x-ray attenuation characteristics:** the relation between I/I_0 and the absorber's thickness is shown. Only the curves for 16, 20, 30 and 40 keV are presented. The thickness of the lead mask ($t = 0.005$ cm) is represented by the vertical black line.

7.2 WOOD MANNEQUIN

The purpose of the wood mannequin was to provide a qualitative analysis about the dynamic range of the imaging system. The dummy has an outer body made of wood, which is quite transparent to x-rays. Inside, a metallic wire unites the wooden parts to keep the structure and allow some torso and member flexibility. This "skeleton" is better at attenuating the x-rays than the wooden body. A picture of this dummy is shown in figure 37.



Figure 37: **Wooden dummy used as an imaging target:** the body of the dummy is made of wood, while an interior metallic wire allows member and torso flexibility.

According to the data represented in figure 38, gathered from the references [63]–[66], wood from the *Rhizophora* species has a similar behavior to the soft tissues of the human body. Although this is not the type of wood used in the manufacture of these mannequins, the response of different types of wood to x-rays does not fall very far from the values presented by [65].

Furthermore, it can be concluded that bone has a completely different response to x-rays, with higher attenuation coefficients, which means that they do not allow the passage of the radiation as easily as soft tissues do. Although the material that constitutes the interior skeleton is unknown, metals and alloys are capable of attenuating the gamma radiation much better than wood.

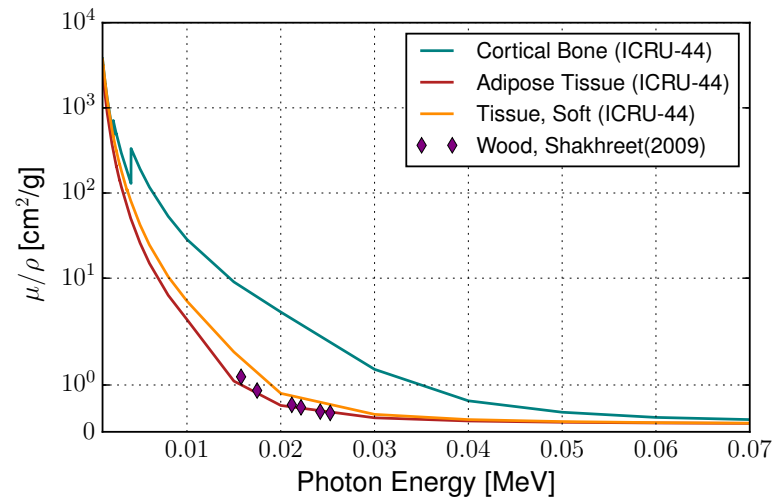


Figure 38: **X-ray attenuation of soft tissue, wood, and cortical bone:** comparing the mass attenuation coefficient of soft tissues of the human body [63], [64] with the one for wood [65], a similar behavior is visible for energies in the range 15.77 – 25.27 keV. The mass attenuation coefficient is also shown for bone [66].

After this analysis, we can conclude that the characteristics of this target may help transpose the imaging system to a medical application; the wooden body may be interpreted as a “soft tissue”, like the skin, while the metallic wire has a similar behavior to hard materials, such as bone. Thus, this target may reflect the potentials of the detection system to the imaging of organic bodies.

7.3 MUSIC BOX

A music box was imaged as it constituted a complex and composite target with intricate details. A rectangular wood base of $(4.51 \times 5.57 \times 5.80)$ cm³ supported the plastic and metallic elements. These constituents can be seen in figure 39. The whole piece (except for the metallic lever) was imaged inside a cardboard case.

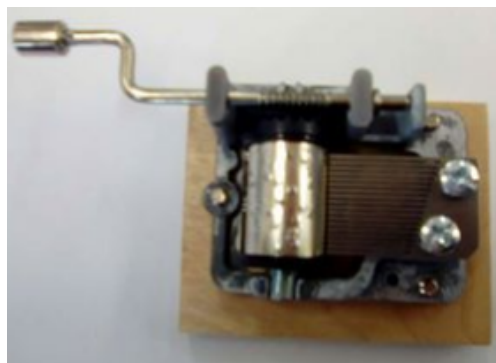


Figure 39: **Interior of the music box:** supported by a wood base, plastic and metallic elements compose the structure of the music box. This object was imaged inside its original cardboard case.

The constituents of the music box have different transparencies to the x-rays. Plastic and cardboard are almost transparent to 20 keV x-rays; wood, on the other end, attenuates some percentage of the photons. The metallic pieces, however, block almost

completely the incoming x-rays. Consequently, it is expected to distinguish the metallic structure of the music box from the wood base, without the interference of the cardboard case.

7.4 GEOMAG® KIT

A Geomag® kit from PlastWood® was also used as an x-ray target. The kit is composed by eight steel spheres (figure 40a) and twelve red magnetic rods (figure 40b) with neodymium magnets as its main constituent. The original polystyrene case was used to contain these elements during image acquisition.

The steel spheres have a diameter of 1.26 cm, while the magnetic rods have a diameter and height of 0.6 cm and 2.79 cm, respectively. The thickness of radiation-penetrated polystyrene was 1.95 cm for the steel spheres and 2.55 cm for the magnetic rods image.



(a) Steel spheres



(b) Magnetic rods

Figure 40: **Geomag® kit**: the kit is composed of eight steel spheres and twelve magnetic rods, enclosed in a polystyrene case.

Because polystyrene has a small attenuation coefficient ($\mu/\rho = 0.4363 \text{ cm}^{-1}$ [67]) when compared to steel or neodymium magnets (which are metallic alloys), x-rays are expected to go through the outer case, being almost completely absorbed by the spheres and rods inside. Consequently, it is expected to individually distinguish the steel spheres as well as the magnetic rods from the polystyrene case.

CHAPTER OVERVIEW

The masks used for x-ray imaging allow the characterization of different properties of the imaging system. While a three-slit grouped lead mask enables the visual estimation of the MTF, the wooden mannequin provided a direct analogy with medical imaging of the human body. A music box, cylindrical magnetic rods and steel spheres also enable qualitative considerations about the response of the imaging system to different materials and shapes.

Part III

SOFTWARE DEVELOPMENT AND TESTING

This chapter focuses mainly on the fundamental requirements the analysis software should satisfy to provide an adequate processing environment with trustworthy output results.

8.1 FUNCTIONAL DESCRIPTION

The system should be able to upload the raw data provided by the detector's electronic system and then compute and show the acquired images. The output images should then be analyzed under multiple metrology parameters, returning the calculated qualitative values as well as the corresponding plots.

8.2 USER'S PROFILE

The target users for this software are researchers who work with imaging systems similar to the one studied in this project. As they are familiar with programming environments, the interface, although indispensable, does not necessarily need to be high level.

8.3 INPUT AND PRECONDITIONS

Each image, to be successfully processed, needs a group of four .dat binary files stored automatically by the electronic system in the laboratory computer. Each file corresponds to a different output channel of the readout board. The data within is arranged in two columns where a `uint64`¹ represents the time information and a `uint16` quantifies the correspondent energy value.

8.4 OUTPUT

The system should reconstruct the acquired images and calculate the SNR, position resolution and MTF correspondent to a given energy range within a predefined region of interest (RoI).

8.5 SUCCESSFUL COMPLETION

A successful image reconstruction and processing should comprise the following fundamental steps:

1. the user inserts the names of the files to be processed;
2. the system processes the files and plots the computed image;
3. the user selects the analysis' tools he finds adequate and inserts the necessary parameters;

¹ `uintn`: unsigned integer of n bits, assuming a value in the interval $(0, 2^n - 1)$.

4. the correspondent functions are called and the results are shown.

8.6 SPEED OF OPERATION

As the input files usually have a size close to dozens of MB (many times approaching a hundred MB), an upper-limit of 5 minutes per image reconstruction was set as an initial objective. This processing time still allows a real-time analysis during the experimental acquisitions.

8.7 ADDITIONAL CHARACTERISTICS

The software should assure portability across multiple platforms and run in the main operating systems used commercially (Unix, Windows and Mac OS). Also, the lowest level of maintenance should be set, ensuring full integrity during software updates. This application, aiming to be a laboratory tool, should allow users to personalize and easily add new functions to the existing code.

8.8 QUALITY

The methodologies used to compute the quantitative parameters for image quality quantification should be based on standard documentation.

CHAPTER OVERVIEW

The developed analysis and processing software should be able to collect the four output files of the detector system and convert the correspondent data into a bi-dimensional image during a practical time frame. Besides the reconstruction, parameters such as the PSF, LSF, ESF, MTF and SNR should be rigorously determined in order to quantify the image resolution. This software is intended to be used in laboratory conditions by researchers familiar to basic programming techniques.

In this chapter, the analysis software for the image processing and the correspondent algorithms are described. The software was developed in Python-2.7 because of its free using policy and facilitated array and histogram manipulation as well as for its powerful tools regarding data visualization.

9.1 IMAGE RECONSTRUCTION

The section of the software that was developed for image reconstruction starts by gathering the data collected from the four channels of the ADC. Then, the correspondent image is reconstructed and plotted as a 2D-histogram. To achieve this result, the binary data files (one for each channel) are loaded and then a coincidence analysis is implemented. After the events are gathered and reconstructed, the correspondent interaction position is computed. Only after these steps, the data is ready to be visualized and analyzed as an image.

9.1.1 *File reading*

For each acquired image four .dat files are generated corresponding to the four different channels of the 2D resistive plate. For each file, time and energy information is recorded as a 64 uint and 16 uint, respectively. This function only requires the name of the files (without the extension nor the channel number) and then collects the time and energy data from the respective files. The time and energy values for each channel are returned as arrays in a dictionary.

9.1.2 *Event resolving*

To identify the recorded data that corresponds to real electron cloud arrivals (events), a signal must be recorded simultaneously in the four channels (within a fixed time window of a few hundred of ns to account for the electronic delay of the detection system). The optimization of this time window value is discussed in the following subsection.

The algorithm to perform the coincidence analysis is illustrated in figure 41 and described bellow:

1. **Concatenation:** the time and energy data from the four channels is concatenated in a single time and energy arrays. At the same time, a channel array is also created to preserve the information of each element in those vectors, having value 0, 1, 2 or 3, according to the readout channel they correspond to.
2. **Sorting:** the time array is ordered in ascending order. The channel and energy arrays are sorted accordingly to preserve the index correspondence between the three vectors.
3. **Neighboring:** three matrices (A_time, A_channel and A_energy) are constructed using the correspondent arrays, according to the format represented in equation

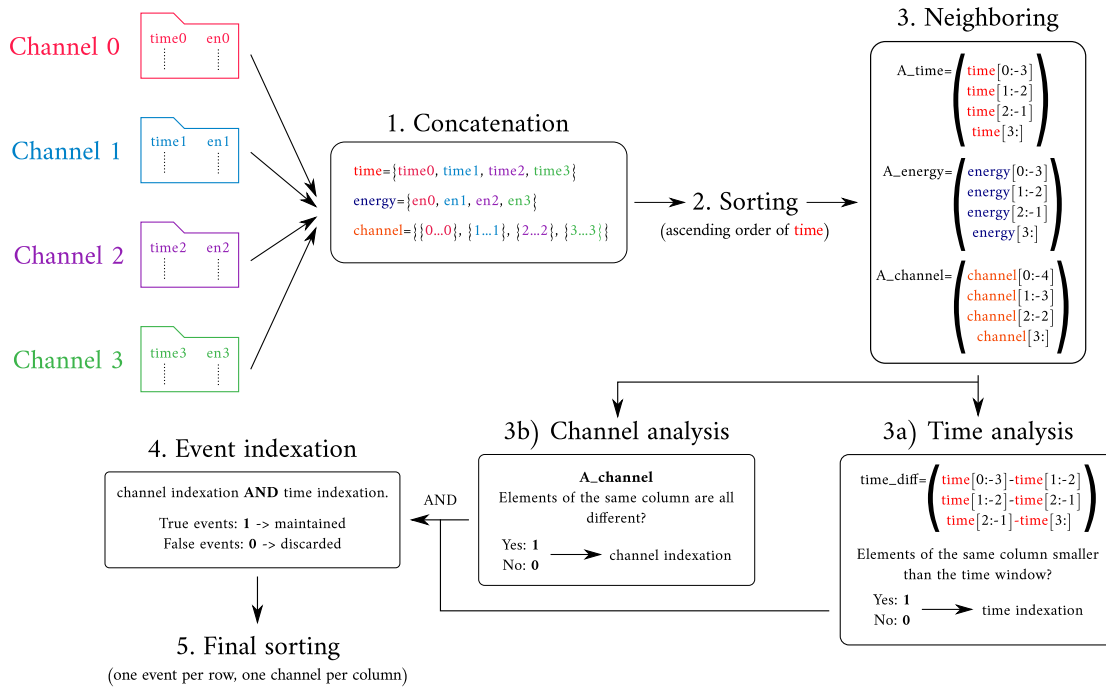


Figure 41: **Coincidence analysis algorithm:** the fundamental steps of the event selection are enumerated. The arrays are represented in “{}”, while the matrices are represented by “()”.

30. The numbers between brackets are the indexes of the original array. The correspondence between the elements of the three matrices is preserved.

$$A_time = \begin{pmatrix} \text{time}[0] & \text{time}[1] & \text{time}[2] & \dots & \text{time}[n-3] \\ \text{time}[1] & \text{time}[2] & \text{time}[3] & \dots & \text{time}[n-2] \\ \text{time}[2] & \text{time}[3] & \text{time}[4] & \dots & \text{time}[n-1] \\ \text{time}[3] & \text{time}[4] & \text{time}[5] & \dots & \text{time}[n] \end{pmatrix} \quad (30)$$

a) **Time analysis:** using the matrix A_time , the consecutive rows are subtracted to evaluate the time difference between the four signals. The elements of the time_diff matrix are compared to the time window parameter and converted into a boolean matrix; when the time difference is lower than the time window, the cell assumes the value 1. The value 0 appears otherwise.

To simplify the following computations, the logic operation “and” is applied to each column of the matrix. This forms a binary array with 1 for the indexes where the signal combination has an adequate time difference and 0 for the false events.

b) **Channel analysis:** evaluating the time difference is not enough to resolve the events: each column must have a signal correspondent to different read-out channels. Consequently, the matrix $A_channel$ is evaluated by column and a boolean array is constructed to be 1 when all the channels are different and 0 when there is a repetition.

4. **Event indexation:** the intersection of the two boolean arrays (channel indexation and time indexation) identifies the indexes where the true events are held. By multiplying this binary vector by the time, channel and energy matrices, only the

true events are maintained (the other rows assume the value 0). This zero-value rows are removed from the matrix because they represent irrelevant data.

5. **Final sorting:** finally, the matrices are simultaneously ordered to guarantee that each column has the information for the same channel number as it is pictured in 31.

$$\text{energy_events} = \begin{matrix} & \text{channel 1} & \text{channel 2} & \text{channel 3} & \text{channel 4} \\ \text{event 1} & \left(\begin{matrix} a_{11} & a_{12} & a_{13} & a_{14} \\ a_{21} & a_{22} & a_{23} & a_{24} \\ \vdots & \vdots & \vdots & \vdots \\ a_{n1} & a_{n2} & a_{n3} & a_{n4} \end{matrix} \right) & & & \\ \text{event 2} & & & & \\ \vdots & & & & \\ \text{event n} & & & & \end{matrix} \quad (31)$$

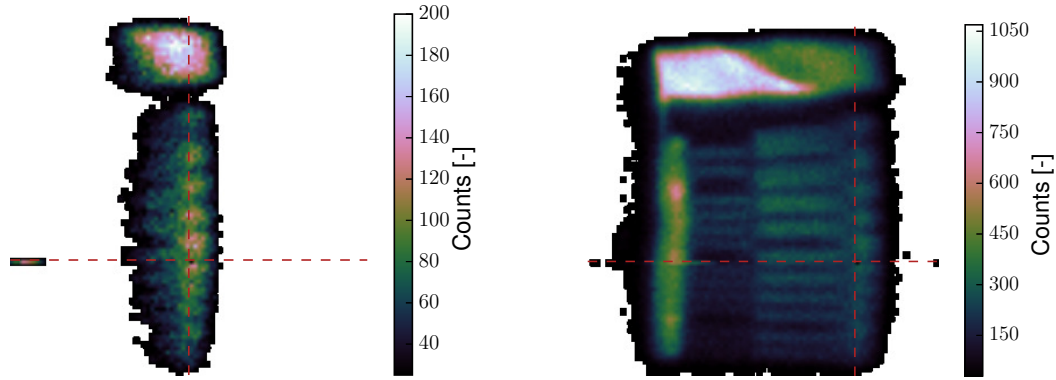
This function only returns the energy values for each channel because the other data is no longer needed in the following computations.

9.1.2.1 Time window optimization

During the processing of the data, the identification of events is highly dependent of the time window parameter. This variable sets the maximum time difference between adjacent signals in the four channels for them to be considered an event. Consequently, the value of the time window must be wisely chosen to guarantee an adequate event identification. A narrow time window implies that a smaller number of peaks will be labeled as events, compromising the statistics needed for a suitable analysis. On the contrary, a wider coincidence interval can wrongly identify uncorrelated electron arrivals as events.

A test was made to evaluate the number of events selected while varying the width of the time window for five krypton-based mixtures and one argon mixture. The six images were acquired by targeting the MTF mask with 35 kV and a $\leq 1 \mu\text{A}$ limiting current setting on the x-ray source. Only the gas mixture and the electric fields were altered. As an example, the image correspondent to the pure krypton acquisition is shown in figure 42, reconstructed with different coincidence window values (300 ns and 1000 ns).

Figure 42a represents an insufficient time window setting, as many relevant information within the data was discarded. On the other end, 42b was reconstructed with an adequate value of the coincidence interval, as the entire profile of the target mask is clearly visible. The representation of the lines $y = 0$ and $x = 0$ also highlights an interesting aspect: although events are visible throughout the vertical coordinate, for small time windows, only the events close to the origin of the horizontal coordinate are selected. By enlarging the coincidence window, further events from the $x = 0$ line appear in the reconstructed image, which is a visual demonstration of the readout plate operation principle. While the events that happen at the middle of the readout strip generate a signal that travels the same distance to both borders, an electron arrival that occurs close to one edge, although its signal is fast to arrive at the closest margin, it needs more time to travel to the opposite one, delaying the overall time of the signal. The fact that this behavior is only visible for the horizontal coordinate may also indicate that the signals travel faster through the vertical resistive strip than through the horizontal strip.



(a) Image reconstitution using a 300 ns time window.

(b) Image reconstitution using a 1000 ns time window.

Figure 42: **Time window optimization data:** this data was collected under a pure krypton flow by irradiating the MTF mask. The x and y dimensions of the image are not calibrated but have the same scale. The vertical and horizontal dotted red lines represent the $y = 0$ and $x = 0$ equations.

For figure 42, the total area of the image was reconstructed for a time window parameter of ≈ 600 ns, being this an estimative of the signal propagation time along the resistive line for this specific acquisition.

The overall results are plotted in figure 43 for the six gas mixtures.

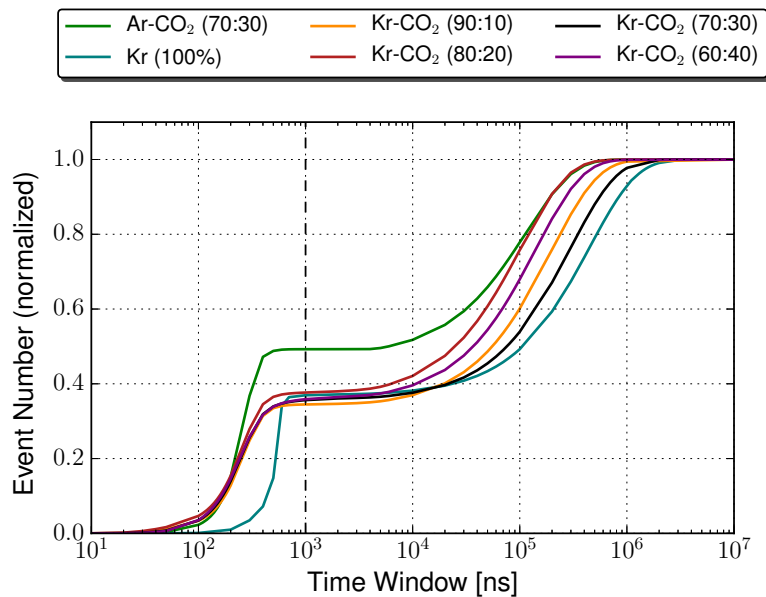


Figure 43: **Time window optimization:** the number of events identified increases with increasing time window until a plateau is reached. A second growth in event selection determines the place where false events begin to be resolved.

In a primary stage, it can be concluded that the number of events increases rapidly with increasing time window. After this, a plateau is visible for each mixture, where the number of events increases very slowly with time window enlargement. This plateau is achieved at different values of time window for the different gas mixtures; while pure Kr requires a minimum value of 8×10^2 ns, the remaining mixtures only

need a 3×10^2 ns for successful event selection. However it is possible to identify a region where all the three mixtures are simultaneously within the correspondent plateau, which allows a unique time window optimization.

The plot also shows that the value of the plateau is quite different for the Ar mixture (happening at 0.5), when compared to the ones achieved for the Kr-based mixtures (less than 0.4). This could be related to noise or charge gain effects, adding more spurious signals to krypton mixtures that are rejected during the coincidence analysis.

For all mixtures, time windows larger than 1×10^4 ns create another rise in the number of resolved events until a second plateau is reached. This second rise in event selection marks the place where false events begin to be identified.

Taking these results into account, the coincidence window was set to be 1×10^3 ns for the entire course of the image analysis. This means that, for each event, the four electric signals have a maximum time difference of 3×10^3 ns.

9.1.3 Event position determination

In most medical imaging systems the events with higher energies are given stronger weights during image reconstruction *i.e.*, the image histogram is constructed using the vector (x, y, E_T) . However, the reconstruction algorithm used in this work makes sure that each event has the same contribution, no matter what its energy value is. The usage of the vector (x, y, counts) is not new, as many works [4], [20], [54] already reconstruct x-ray images with this information. This choice was made because, typically, setting equal contributions for all the events allows higher contrast and flexibility during image analysis [54].

The energy arrays of the four channels are usually used to calculate the vertical and horizontal coordinates where the event took place relatively to the resistive readout using the equations depicted in 29.

Knowing the correspondence between the geometry of the detector and the channel number, the x and y values can be calculated for each event. The calibration factor, L , however, needs to be later determined for each experimental condition. This software function returns three arrays with the horizontal and vertical positions, and the correspondent total energy value.

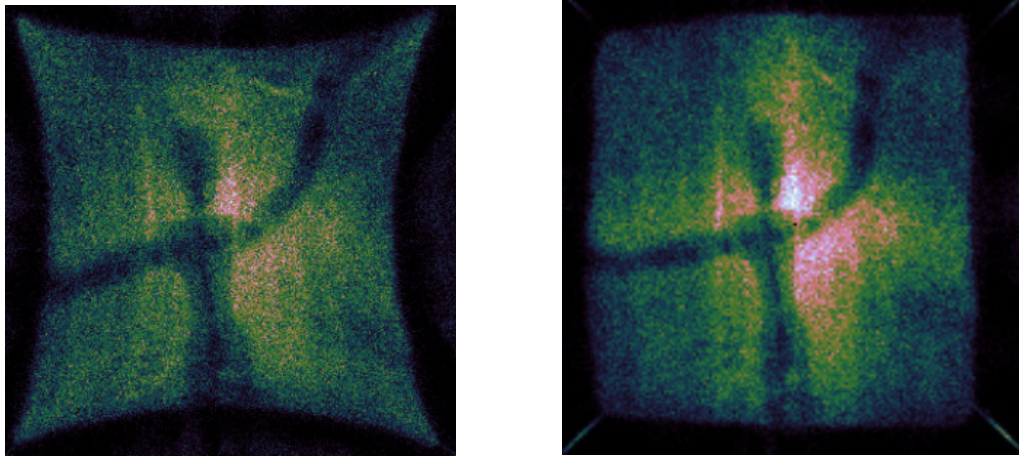
Although equations 29 (page 49) represent the most common method to calculate the coordinates of the event, the reconstructed images show a pincushion-type distortion, as seen in figure 44a.

During software evaluation, the usage of equations 32 strongly attenuated the distortion effect. This result is represented in figure 44b.

$$x = \frac{X_A - X_B}{X_A + X_B + Y_A + Y_B} \times L \quad y = \frac{Y_A - Y_B}{X_A + X_B + Y_A + Y_B} \times L \quad (32)$$

In this algorithm, instead of dividing the signal difference solely by the energy sum in the correspondent channels, the total energy is used.

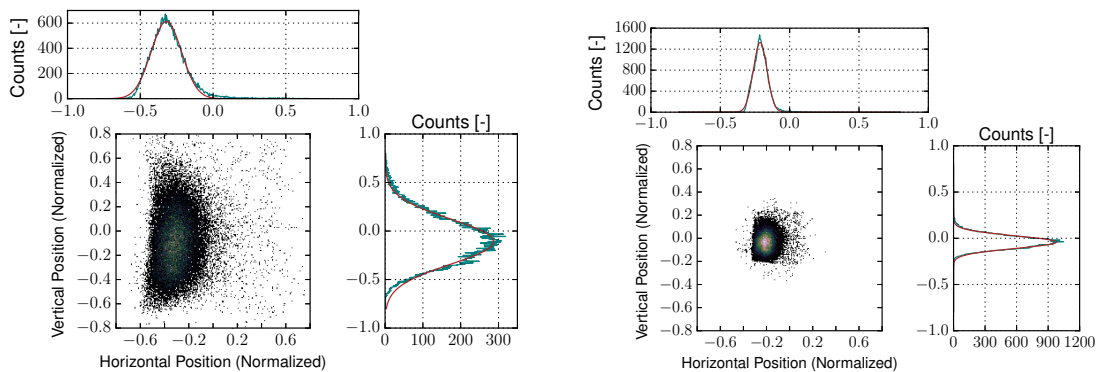
After these empirical considerations were made, it was necessary to compare quantitatively the two reconstruction equations. The INL (already described in section 4.2.5.4) was determined for the same images, each of them reconstructed with both formulas. For this study, the images used in the uniformity study (section 12.2) were reconstructed using both equations. This set of a hundred images comprise a point source image of the ^{55}Fe x-ray source moved along a 10×10 equally-spaced (1 cm) grid, covering the total area of the detector's window.



(a) Image reconstitution by applying equation 29 . (b) Image reconstitution by applying equation 32.

Figure 44: **Characteristics of the reconstruction equations:** the same data was used to reconstruct the images using equations 29 (a) and 32 (b). The usage of the latter dissolves the pincushion-type distortion.

The position of the point source in each image was determined by projecting the image in the x and y coordinates and fitting the correspondent profiles to a normal distribution. The average of the fitted Gaussian distribution was recorded as the point source location for that coordinate. This methodology is illustrated by figure 45, where $L = 1$ was set for both cases.



(a) Point source location using the reconstruction equation 29.

(b) Point source location using the reconstruction equation 32.

Figure 45: **Point source location using horizontal and vertical Gaussian fitting:** the same image of the ^{55}Fe point source (positioned at (3,6) in the 10×10 grid) was reconstructed using two reconstruction equations. The average of the x and y projections was interpreted as the location of the point source. This algorithm was repeated for all 100 images.

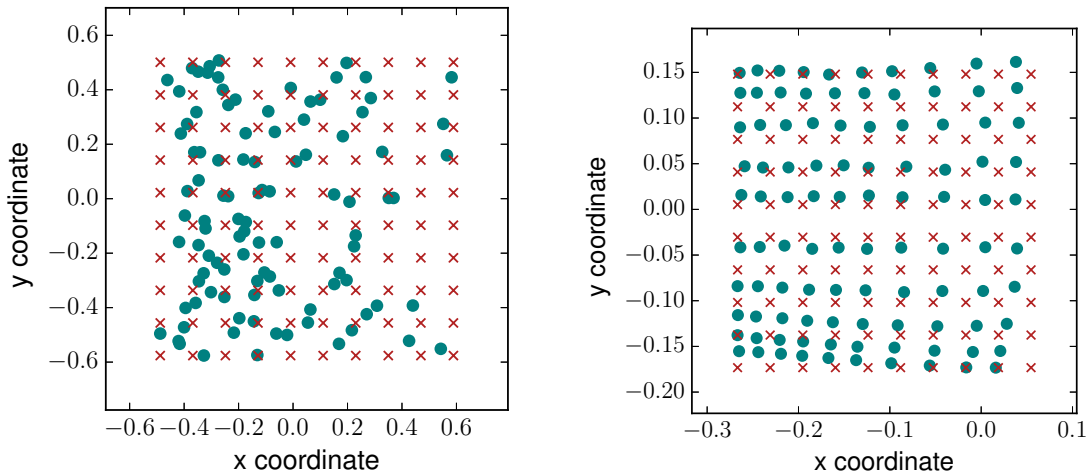
By analyzing the two reconstructions of the same image, the quality of the equations is visibly different; while equation 29 produces a more blurred image, equation 32 originates a well-defined circular shape, as expected.

The coordinates of each point source are depicted in figure 46, in blue, for the two reconstruction equations. Besides these experimental data points, the expected

positions of the point source are also presented in red. The theoretical points were calculated to be equally spaced in the x and the y coordinate, with a pitch equal to the quantity shown in equation 33 and starting at the $(\min(x), \min(y))$ coordinate. This equation determines the pitch as the average pitch between x and y grid points.

$$\Delta = \frac{1}{2} \times \left[\frac{\max(x) - \min(x)}{10} + \frac{\max(y) - \min(y)}{10} \right] \quad (33)$$

This theoretical grid was calculated for each reconstruction equation separately.



(a) Point source distribution using the reconstruction equation 29.

(b) Point source distribution using the reconstruction equation 32.

Figure 46: **Point source distribution in an equally-spaced grid:** the experimental data is plotted in blue, while the expected positions are identified with a red cross. The reconstruction of the grid is more successfully achieved using equation 32.

Once more, comparing the results provided by both equations, equation 32 is capable of reproducing the grid layout more rigorously than equation 29. Nevertheless, the points near the edges of the detector still show a certain level of distortion when compared to the points at the center of the active area.

Finally, the distance of each point (for the results of equation 29, 32 and the correspondent expected values) relatively to the coordinate $(0,0)$ was determined. All distances were normalized to produce comparable results. For each equation, the normalized point distance (virtual distance) was plotted as a function of the normalized expected distance for that data point (real distance) and a linear fit was made to the final distribution. The results are shown in figure 47.

For each distribution a linear fit was made, achieving a function defined as

$$y = 0.666(67) \cdot x + 0.161(40), \quad r^2 = 0.502 \quad \text{INL} = 0.117(6)$$

for equation 29 and a function characterized as

$$y = 0.952(30) \cdot x + 0.108(17), \quad r^2 = 0.910 \quad \text{INL} = 0.056(2)$$

for equation 32, where y is the virtual distance and x is the real (expected) distance.

Based on the plots alone, the linear tendency is much more visible for the images reconstructed with equation 32. Furthermore, the dispersion of the data points is much smaller with this last reconstruction algorithm.

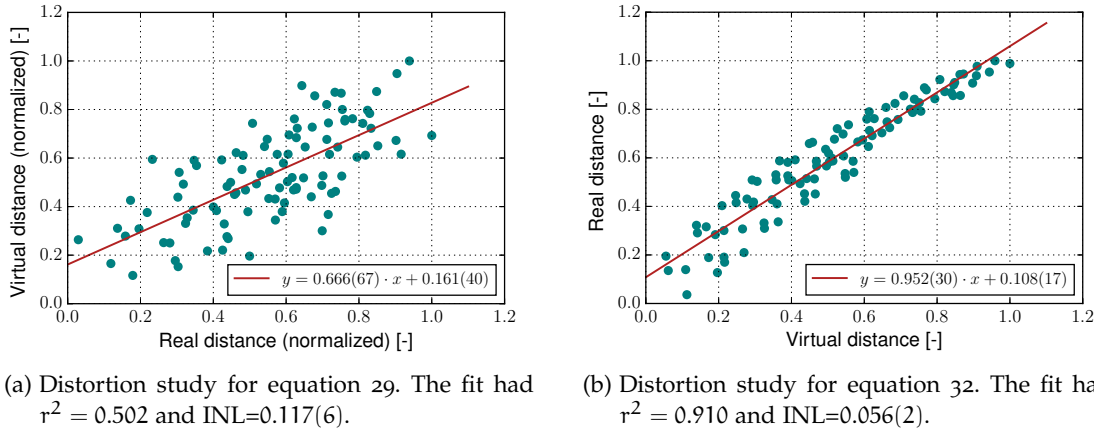


Figure 47: **Distortion quantification for the reconstruction equations:** the distance of each data point to the coordinate $(0,0)$ is plotted as a function of its theoretical distance (blue). A linear fit (red) was made to quantify the correlation of the two variables for each formula.

By evaluating the linear regression, the residuals are much bigger for the images generated with equation 29, and the fit is much poorer according to the value of r^2 . Equation 32, on the other end, shows a linear regression determined with much more confidence ($r^2 = 0.919$), reflecting a strong and direct correlation between the reconstructed coordinates and their expected location.

Furthermore, the INL for equation 29 is about 50% bigger than the INL for equation 32. This means that, using equation 32, each reconstructed coordinate is closer to the expected value than when equation 29 is applied.

Taking all these factors into account, using equation 32 as an alternative to equation 29 guarantees coordinate rigorousness during image reconstruction, minimizing the distortion effects, mainly for events collected at the center of the readout board.

9.2 IMAGE ANALYSIS TOOLS

The images were represented as a 2D histogram of events recorded in each horizontal (x) and vertical position (y). The computed histograms possess 500 bins in each direction which implies, for the biggest calibration factor ($L = 24.587$ cm), a pixel 0.98 mm wide. The minimum expected spatial resolutions are in the order of 1.5 mm, so the results are unaffected by the pixel resolution, as well as this factor is taken into account.

9.2.1 Point source profiling

When a collimated x-ray source is imaged, the PSF of the detection system can be estimated from the horizontal and vertical projections of the 2D histogram. As a result, the function $psf()$ determines these two projections while fitting a Gaussian function (equation 34) to each one. This methodology was the one used to generate figure 45. While \mathcal{A} represents the amplitude, \bar{x} and σ represent the centroid and the standard deviation of the normal distribution.

$$f(x) = \mathcal{A} \times \exp\left(-\frac{(x - \bar{x})^2}{2\sigma^2}\right) \quad (34)$$

These values can only be seen as the true PSF of the system if the imaged point source is dimensionless. Nevertheless, they are able to quantify the horizontal and vertical profiles, allowing direct comparison between images acquired in different experimental conditions. The position resolution is determined from the Gaussian profile by calculating its FWHM by equation 9.

9.2.2 Double slit profiling

To evaluate the profile of a certain region of interest (RoI), the software allows the definition of its edges (x_{\min} , x_{\max} , y_{\min} and y_{\max}) and adds the count number in the vertical coordinates. This tool is especially useful to evaluate the spatial resolution of the detector from double slit acquisitions.

After the user defines the RoI, the bimodal function shown in equation 35 is fitted to the experimental data. The \mathcal{A}_i represents the amplitudes of the normal distributions, \bar{x}_i the centroids of the Gaussians and σ_i is their standard deviation.

$$b(x) = \mathcal{A}_1 \times \exp\left(-\frac{(x - \bar{x}_1)^2}{2\sigma_1^2}\right) + \mathcal{A}_2 \times \exp\left(-\frac{(x - \bar{x}_2)^2}{2\sigma_2^2}\right) \quad (35)$$

The fit then returns the two centroids and the correspondent position resolutions, calculated from the standard deviation with equation 36.

$$R_i = 2\sqrt{2 \ln 2} \sigma_i \quad \delta R_i = \frac{R_i}{\sigma_i} \times \delta \sigma_i \quad (36)$$

Although no image acquisitions that justified the usage of this algorithm were performed, the development of a function to evaluate a double LSF could be of interest in future investigations.

9.2.3 Position resolution and MTF determination

To determine the spatial resolution and the MTF of an acquired image, the edge-gradient analysis method (represented in figure 48) was chosen because it is one of the most rigorous and common algorithms to perform the computation. More recently, the standard ISO-12233 introduced a new method to calculate this parameter using more realistic experimental conditions: the slanted-edge method allows MTF determination using slanted or skewed edges. However, as the acquired images in this work have an edge feature oriented in a direction perpendicular to the edge, a more complex algorithm is not necessary to compute the system's MTF [68].

The overall algorithm implementation is illustrated in figure 49.

The most important prerequisite needed to perform an adequate edge-gradient analysis is the acquisition of an image with edge scans oriented perpendicular to the edge itself [69]. A RoI containing only a edge profile must then be defined. The following computations are implemented only in this smaller region (bottom of figure 49a). The reflectance (in this case it is perceived as the count histogram) is then represented as a function of the position along the edge scan, composing its ESF. This profile is fitted to a transformation of function 16, (equation 37) to allow vertical amplitude (m),

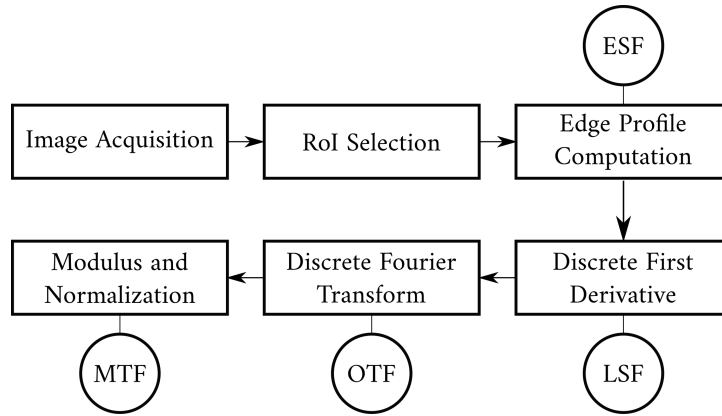
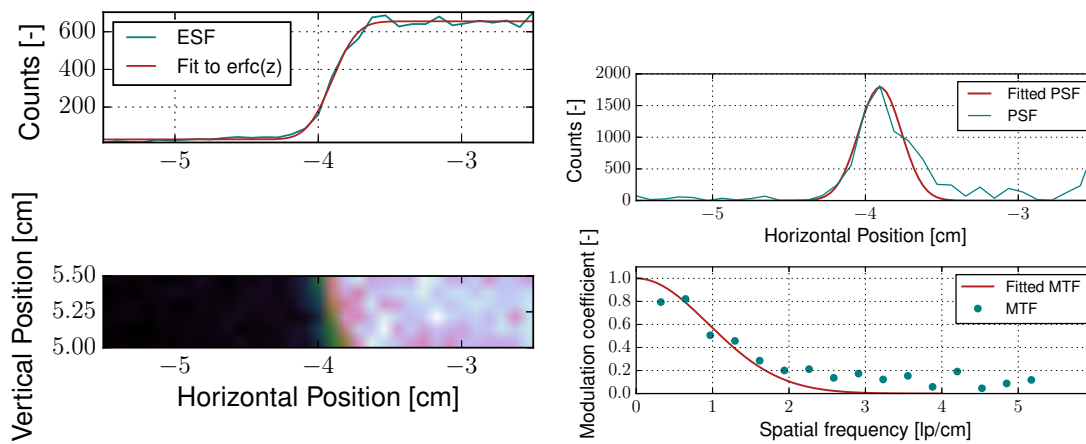


Figure 48: **Edge-gradient analysis algorithm:** this is the most traditional method used in literature to determine the MTF using an edge profile.



(a) Determination of the ESF from a horizontal edge profile.

(b) MTF and LSF determination.

Figure 49: **Implementation of the edge-gradient algorithm:** after selecting a RoI containing a sharp, non-slanted edge, the ESF is determined and fitted to equation 37. By computing the first derivative and the Fourier transform, the LSF and the MTF are determined, respectively.

horizontal and vertical shift (a and c , respectively) and dilation/contraction (b) of the edge relatively to the conventional error function. At the end of this step, the ESF is estimated from the input data.

$$f(z) = m \times \operatorname{erfc} \left[\frac{z - a}{b} \right] + c \quad (37)$$

The fitted function is then derived to obtain the LSF, according to the relation represented in equation 18. Computationally, the derivation is made using a discrete first derivative algorithm using the `gradient()` method from the numeric python (numpy) library.

This profile is fitted to a normal distribution from which the position resolution (FWHM) value can be derived (figure 49b). The error related to this factor was propagated from the ESF goodness of fit to the error function, which is illustrated by equation 38.

$$\delta\text{FWHM} = \sqrt{2\ln 2} \times \delta b \quad (38)$$

Using the relation represented in equation 19, the discrete Fourier transform of the LSF function originates the Optical Transfer Function (OTF) and its modulus and normalization originates the MTF. The discrete Fourier transform was computed (and applied to the Gaussian fit) using the `fft.fft()` and `fft.fftfreq()` methods from the numpy library. A Gaussian fit was then applied to this profile.

The developed software automatically plots the RoI histogram, the ESF, LSF and MTF, as seen in figure 49. The position resolution is calculated as the FWHM of the LSF, by applying equation 9 (page 26). The value of the MTF at 10% in lp/cm is also determined according to equation 39. This formula was determined as the intersection of a normalized Gaussian with parameters $(\bar{x}, \sigma, \mathcal{A} = 1)$ to a line of equation $y = 10\%$. This is true because the MTF is a normal distribution as it is the Fourier transform of the LSF (also a Gaussian distribution).

$$\begin{aligned} \text{MTF}(10\%) &= \bar{x} + \sigma\sqrt{-2\ln(0.1)} \\ \delta\text{MTF}(10\%) &= \sqrt{\delta\bar{x}^2 - 2\ln(0.1)\delta\sigma^2} \end{aligned} \quad (39)$$

9.2.4 SNR determination

To evaluate the SNR within a complex image, a RoI must be selected by the user from the horizontal and vertical boundaries (x_{\min} , x_{\max} , y_{\min} and y_{\max}). Inside that region, equation 12 is applied, where \bar{x} is the average of pixel intensity and σ is the standard deviation of the pixel intensity in the same region. These values were calculated using the functions `mean()` and `std()` from the numpy library.

9.2.5 Energy filtering

The software also enables the analysis of each image in a narrower energy interval. Firstly, the energy spectrum is plotted. After this, the user selects the energy intervals of interest for further analysis. Only the events within the selected interval are filtered and a sub-image is formed. This procedure is illustrated in appendix A.

This energy selection affords direct application of all the tools described above, such as the MTF and position resolution determination. As a consequence, the behavior of these parameters can be easily studied for different energy intervals.

CHAPTER OVERVIEW

The quality parameters established by the software requirement specification were successfully implemented. These tools can be divided into data processing related to image reconstruction and image analysis.

The software actuates by reading the binary files and resolving the events, selecting only signals that are recorded simultaneously (within a coincidence window of 3×10^3 ns) in the four readout channels. The bi-dimensional event position is then calculated by a new formula that minimizes distortion effects.

The image analysis is capable of calculating the PSF, from a point source image, the LSF from a double-slit target and the MTF and position resolution from a perpendicular edge profile. Images can also be generated by selecting a specific energy window and the position resolution can be determined for each energy interval. The SNR calculation was also implemented.

In this section, the properties of the developed analysis software will be compared with the previously established *software requirement specification*. The limitations and external system prerequisites are also referenced.

10.1 FUNCTIONAL REQUIREMENTS

The final version of the software was capable of performing the following tasks:

- Reconstruct the image from the raw input files;
- Perform position and energy calibration for different experimental conditions;
- Select regions of interest within the original image for further analysis;
- Profile the image of a collimated x-ray source and quantify the vertical and horizontal projections (assuming they follow a normal distribution);
- Profile the image of a double slit and determine the correspondent position resolution (from the FWHM) by fitting a double-Gaussian;
- Determine the energy histogram of the original image;
- Determine the SNR of a predefined RoI;
- Determine the position resolution of the image by the edge-gradient method and the correspondent MTF;
- Select a customizable energy interval from the histogram and represent only the events within that interval, creating a sub-image. The tools previously enumerated can then be applied to each sub-image;

Consequently, and as it was proposed in the requirement analysis, the software is capable performing the originally proposed tasks.

10.2 SPEED OF OPERATION

The speed of operation is not an easy parameter to evaluate, as it is highly dependent of many system variables such as data size, acquisition time, computer task-queue, histogram bin number, processing power, among others. However, the running time was determined for each image reconstruction process and, for the images evaluated in the course of this project, no individual task surpassed the time of 2 min. This limit is well below the threshold indicated during the SRS, which allowed “real-time” visualization of the images during acquisition.

This factor optimized greatly the experimental procedures, as it was possible to see, with a 60 s acquisition time, if the target object was visible and centered in the final image, which was crucial for the fluency of the experimental work. With this 60 s test, adjustments to the experimental conditions (target positioning, tube voltage and limiting current) could be performed very quickly, increasing the productivity of the experiments.

10.3 COMPATIBILITY AND MAINTAINABILITY

As the software was written using python-2, which is compatible with most operating systems, there will be no loss as long as the following packages are correctly installed:

- numpy
- scipy
- matplotlib
- pyplot
- os
- decimal

Although the processing and analysis functions were written in a script and are accessible manually from the terminal, a jupyter notebook¹ was developed to facilitate the image analysis process. This environment was able to simplify the interaction process between the user and the computer. The advantage of markdowns and the `%matplotlib inline` feature allows real time image visualization in an organized manner. Some screenshots of this interface are shown in appendix A.

Another advantage of this environment is the ease with which a user can add more cells and call other functions within the script according to the necessities of the analysis procedure. Jupyter notebook also exports the results of a certain time-instance into a .pdf file, which is also of interest for fast report production.

10.4 FLEXIBILITY

During software development, each function and correspondent algorithms were documented within the attached Jupyter Notebook (and, in some cases, commented next to the code) to allow future alteration or additions by external users.

10.5 QUALITY

All the algorithms applied to the images were constructed using standard documentation as well as external knowledge of more experienced members of the collaboration to produce rigorous results.

Whenever possible, the output parameters and plots were compared to the previous analysis software and the results were consistent.

Another test was made to evaluate the consistency of the implemented edge-gradient method (described in section 9.2.3), as this was the most complex and important analysis tool for the objectives of this dissertation project. For the same image and RoI (featuring an image of a sharp edge), the position resolution was determined for two different energy intervals:

- **Odd:** for events within [2,4] keV, [4,6] keV, [6,8] keV, [8,10] keV, *etc.*
- **Even:** for events within [1,3] keV, [3,5] keV, [5,7] keV, [7,9] keV, *etc.*

With this test, the two sets of results are expected be consistent and follow the same tendency with energy variation. The results were plotted for the average value of the energy interval and are shown in figure 50.

¹ **Jupyter notebook:** cell-based files that run and present the correspondent output of introduced computer code. Rich text elements such as paragraphs of text, links, figures and equations are also supported.

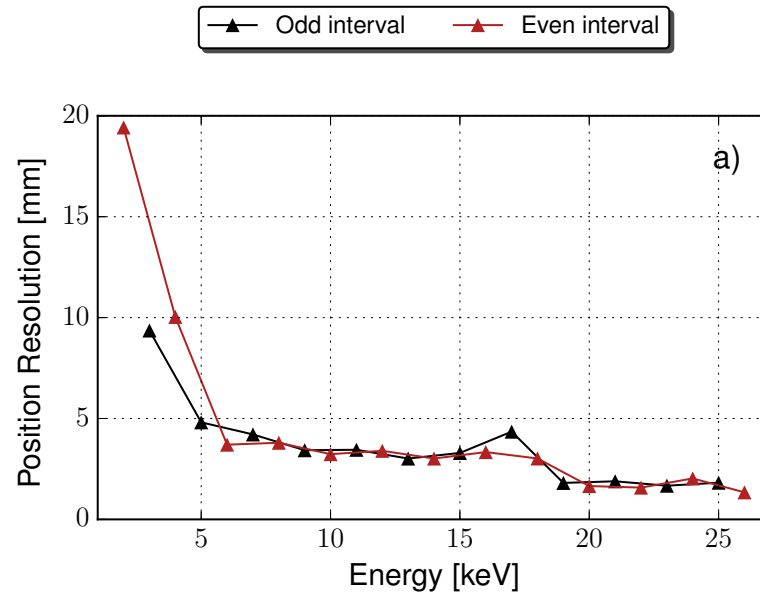


Figure 50: **Consistency of the position resolution determination:** by selecting slightly different energy intervals for the sub-images reconstruction, the values of position resolution show small fluctuations and follow the same tendency.

The plot shows small fluctuations and similar behaviors between odd and even energy intervals, which is a strong indicator that undesired artifacts do not affect the consistency of the edge-gradient method implementation. Other RoIs comprising a sharp-edge profile were evaluated under this same methodology, expressing similar results.

10.6 LIMITATIONS

The most relevant limitation of the software is related to the fact that it could not be used in the laboratory computer that recorded the data directly from the ADC. This device runs under the Scientific Linux operating system which requires the 2.6.6 python version for intrinsic functions. However, the matplotlib library (fundamental for data visualization) requires, at least, the 2.7 version. As a consequence, the raw data files needed to be sent from one computer to the other before image visualization could take place. Even though this procedure slowed down the overall process, the acquired images could still be rapidly observed and analyzed during the the course of the measurements.

CHAPTER OVERVIEW

After the software was developed, many initial requirements were met, such as processing time, available tools and performance. The edge-gradient method implementation was also tested in terms of result consistency, indicating that no undesired artifacts were present.

All these factors allow a rigorous and fast processing environment that simplifies the experimental measurements and image quality quantification.

Part IV

EXPERIMENTAL RESULTS AND DISCUSSION

This chapter focuses on the determination of the electronic, position and energy calibration of the detector as well as the optimization of the imposed electric fields. These procedures were performed for each gas mixture to ensure that the best experimental conditions were set for later detector characterization.

11.1 ELECTRONIC CALIBRATION

To establish the relation between the channels in the MCA and the charge in this particular system, a 1 pF capacitor was used to inject a known amount of charge into the electronic chain, as a substitute for the detector. The block diagram of the actual setup used is presented in figure 51.

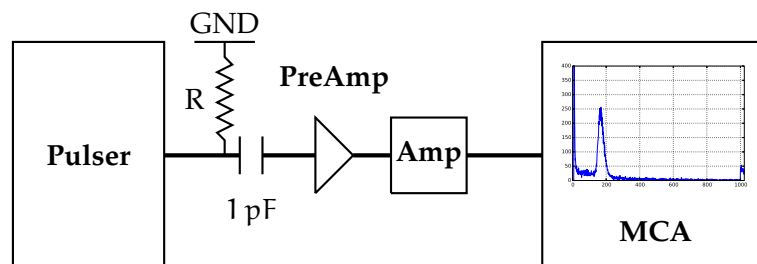


Figure 51: **Electronic calibration system setup:** a *Pulsar* injects a known amount of charge into a 1 pF capacitor, which discharges by the means of a resistance (R). A preamplifier (*PreAmp*) and then an amplifier (*Amp*) integrate the charge signal that leaves the capacitor which is then read by the MCA in the form of an histogram of counts *per* channel. The common instruments are the same as the ones described in chapter 5.

In the course of this work, two different calibrations took place as the electronic setup was changed in between measurements. The first calibration was used in the Kr(100%) experiments and the second one in the Kr-CO₂ (90:10) and Kr-CO₂ (80:20) mixtures.

When the detector is irradiated with a mono-energetic x-ray source, the amplitude of the output pulses follow the behavior of a normal distribution, with its average value proportional to the energy of the x-rays emitted by the radioactive source. In this case, the ⁵⁵Fe source was used so the average value of the normal distribution should correspond to an energy of 5.9 keV [70].

For each one of the induced amplitudes (V_i), the output channel (C_i) that corresponded to the Gaussian peak in the MCA was recorded. These amplitudes were then translated into values of charge gain.

Measuring the amplitudes of the signals with an oscilloscope (V_i), it was possible to determine the charge induced in the capacitor (Q_i) with $C = 1$ pF using equation 40.

$$Q_i = C \cdot V_i \quad (40)$$

From here, the final charge was (N_f) was determined with equation 41.

$$N_f = Q_i/e = \frac{C \cdot V_i}{e} \quad \delta N_f = \frac{C}{e} \sqrt{\delta V_i^2 + \left(\frac{V_i}{e}\right)^2 \cdot \delta e^2} \quad (41)$$

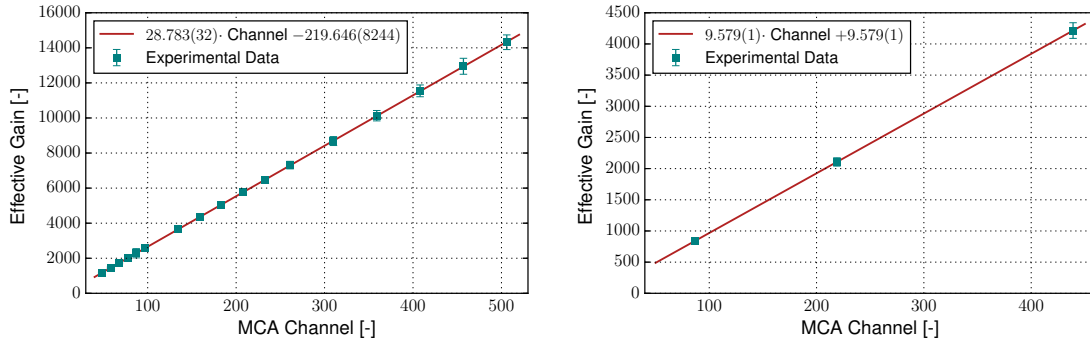
Being w the average energy necessary to produce an electron-ion pair, which, for krypton is $w_{Kr} = 24.0(7)$ eV [36]¹, the initial number of electrons N_i before the multiplication process becomes

$$N_i = \frac{E}{w} \quad \delta N_i = \frac{E}{w^2} \cdot \delta w \quad (42)$$

Finally, the charge gain (\mathcal{G}) of the detector for each of the amplitudes is determined by the relation:

$$\mathcal{G} = \frac{N_f}{N_i} = \frac{C \cdot V_i \cdot w}{e \cdot E} \quad \delta \mathcal{G} = \frac{C}{e \cdot E} \sqrt{w^2 \cdot \delta V_i^2 + \left(\frac{w \cdot V_i}{e}\right)^2 \cdot \delta e^2 + V_i^2 \cdot \delta w^2} \quad (43)$$

Figure 52 was the result of plotting the charge gain value as a function of the centroid channel for both calibrations.



(a) Calibration curve obtained for pure krypton measurements: the linear fit revealed the coefficients $m = 28.783(32)$ and $b = -219.646(8244)$. (b) Calibration curve obtained for the 90:10 and 80:20 mixtures: the linear fit revealed the coefficients $m = 9.579(1)$ and $b = 9.579(1)$.

Figure 52: **Electronic calibration curves using a 1 pF Capacitor:** the charge gain (\mathcal{G}) as a function of the the MCA channel (centroid of the distribution for each electronic pulse) is represented in blue. The red line shows the linear fit ($y = mx + b$) applied to the experimental data.

The linear behavior of the data is visually clear and the error bars are insignificant when compared to the dimensions of the correspondent data points.

The values of charge gain (\mathcal{G}) can be determined from the centroid of the distribution of the x-ray pulses recorded by the MCA (Channel) using a linear regression. Equation 44 corresponds to the data set shown in figure 52a and equation 45 was obtained from the data plotted in figure 52b.

$$\mathcal{G}_1 = 28.783(32) \times \text{Channel} - 219.646(8.244) \quad (44)$$

$$\mathcal{G}_2 = 9.579(1) \times \text{Channel} - 9.579(1) \quad (45)$$

¹ w -value for 1350 mbar and $E_p = 5.9$ keV

11.2 ENERGY CALIBRATION

The energy calibration was performed for each set of experiments using the energy histogram of the ^{55}Fe point source. As the spectrum determined for krypton mixtures comprises a single dominant peak, the ADC offset was previously determined with an Ar-CO₂ (70:30) mixture. Because argon has a lower value of the K_α emission line (2.95770 keV [71]), an escape peak is expected at 2.94015 keV. This double peak profile enables a more rigorous energy calibration, as seen in figure 53.

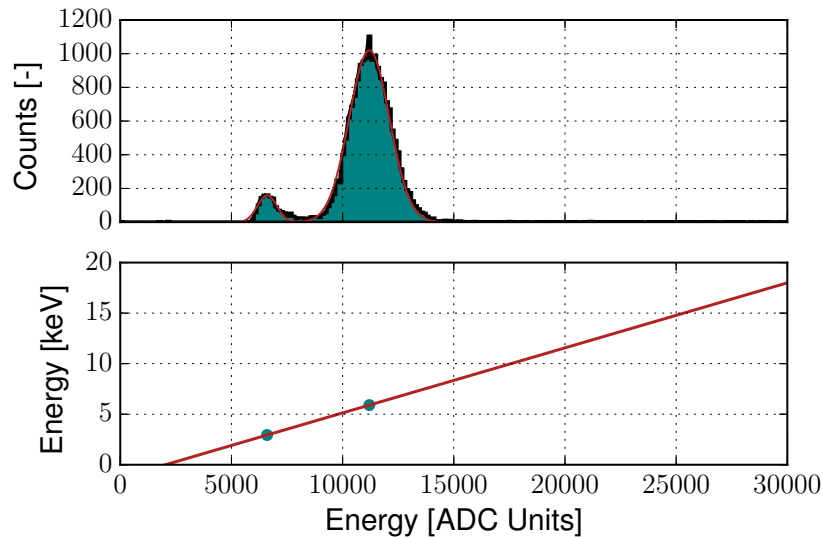


Figure 53: **Energy spectrum of a ^{55}Fe source in Ar-CO₂ (70:30):** the ^{55}Fe K_α emission line and the correspondent escape peak for argon are both visible. The result of the linear fitting was $y = 0.000640 \cdot x - 1.266258$.

These peaks were then fitted to a bimodal distribution (equation 35), where the mean of the distribution, \bar{x} , is the centroid value in ADC units. The calibration curve is defined by equation 46.

$$E_{\text{keV}} = 0.000640 \times E_{\text{ADC}} - 1.266258 \quad (46)$$

By definition, this linear regression has no parameter-related error because only two data points were used.

From this relation, the ADC offset was determined as 1979 ADC channels. Using this value along with the fitted value of the ^{55}Fe peak for each krypton mixture, energy calibration was possible.

11.3 POSITION CALIBRATION

The position of the system was calibrated for each image by choosing an inner region of known dimensions in cm. Figure 54 illustrates the methodology used for the calibration process.

The uncalibrated images were reconstructed from equation 32, by setting $L = 1$.

Knowing the distance that separates two borders within the image, χ , two RoIs that comprise the edges (red rectangles) were selected. For each one of these regions the ESF was determined. The edge profile was then fitted to equation 37 where parameter a quantifies the position of each edge for the uncalibrated image. Thus, by

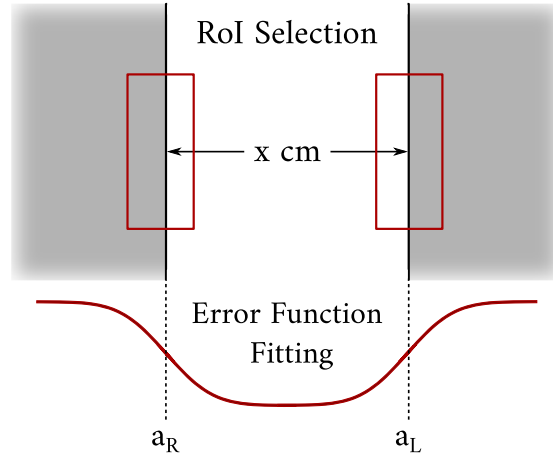


Figure 54: **Schematics of the position calibration method:** the borders (red rectangles) that limit a known length (x cm) were fitted to an error function. This allowed the determination of the right and left positions of the borders (a_R and a_L , respectively).

determining a_L and a_R , which are the edge positions for the left and right borders, respectively, the distance between the object's edges could be calculated. Finally, the calibration parameter from equation 32, L , was determined by equation 47.

$$L = \frac{x}{|a_R - a_L|}$$

$$\delta L = \frac{1}{|a_R - a_L|} \cdot \sqrt{\delta x^2 + \left[\frac{x}{|a_R - a_L|} \right]^2 (\delta a_R^2 + \delta a_L^2)} \quad (47)$$

By updating the calibration parameter for each quantitative image, the correspondent position resolution could be determined rigorously.

For the images presented in appendix B, the spatial calibration constants (L) are presented in table 6, as these were the images used for position resolution determination.

Table 6: **Position calibration constants used for quantitative analysis:** the position calibration constant, L , is given for each image presented in appendix B. This parameter was fundamental for later position resolution determination and MTF profiling. The values are presented in cm.

ARGON	100%	90:10	80:20	70:30	60:40
21.397(2)	24.587(2)	23.273(2)	23.217(2)	23.568(2)	23.676(2)

Except for the Ar-CO₂ (70:30) image, the calibration constants have consistent values, which was expected, as the imposed experimental conditions were similar.

11.4 ELECTRONIC OPTIMIZATION

To choose the optimum electronic conditions for the detector, exhaustive measurements were made to study the behavior of the charge gain and energy resolution for different induction, transfer and drift fields.

For these measurements, the ^{55}Fe x-ray source was used and the readout board was short-circuited to collect the sum of the four channels in the MCA so a stronger signal could be recorded. The electrodes that compose the detector were independently biased and the voltages of the top and bottom GEMs, were kept at $\Delta V_{\text{GEM}1,2} = 550\text{ V}$ and $\Delta V_{\text{GEM}1,2} = 600\text{ V}$ for the 90:10 and 80:20 mixtures, respectively. Pure krypton measurements were performed using $\Delta V_{\text{GEM}1} = 530\text{ V}$ and $\Delta V_{\text{GEM}2} = 560\text{ V}$. The differences in the biasing voltages of the GEM plates do not allow a direct comparison between the performance of the gaseous mixtures in terms of charge gain at this stage. However, the objective of this study was only to infer the optimum voltages that maximize the values of charge gain and minimize the relative values of energy resolution. The obtained results were used to setup the detector for the comparative studies developed in the following chapter.

After obtaining the spectra with the MCA, a double-Gaussian fit (for the ^{55}Fe K_{α} and K_{β} peaks) was performed with the AJUST0 software that determined the centroid and energy resolution of the correspondent peak. The position of the K_{α} was then converted into charge gain values using equations 44 and 45.

The plots of energy resolution here presented describe only relative values, where the first measurement value was set at zero.

11.4.1 Drift region

For the drift field studies, the voltage difference between the cathode mesh and the top of the first GEM was modified while the other electrodes were kept at constant potentials, according to table 7.

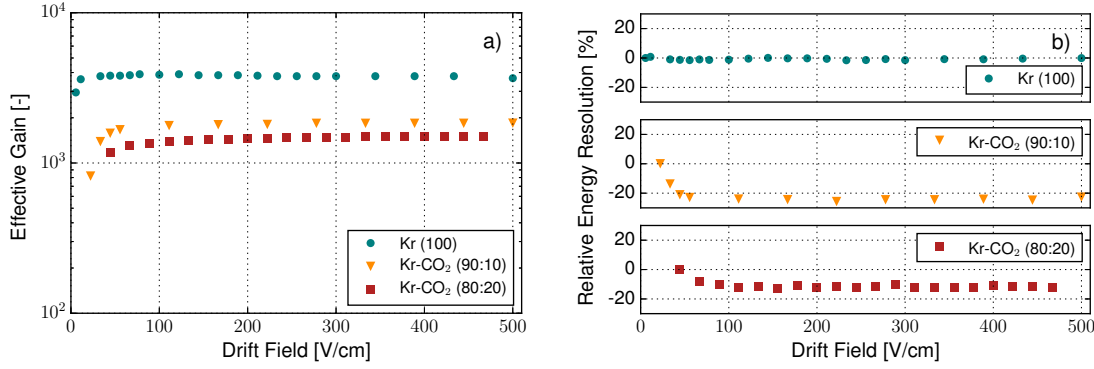
Table 7: **Electric fields for the drift region optimization:** the transfer and induction fields implemented during the optimization of the drift field are presented for each gas mixture.

	Kr (100%)	Kr-CO ₂ (90:10)	Kr-CO ₂ (80:20)
INDUCTION FIELD (V/cm ²)	500	2500	1500
TRANSFER FIELD (V/cm ²)	702	1930	2807

The results of this study are shown in figure 55.

As expected, as the applied drift field increases, a gradual rise in the absolute gain was recorded, followed by a constant plateau. For low electric fields, the voltage difference is not strong enough to overcome charge recombination, so the charge gain is low. As the electric field increases, more and more electrons are focused into holes of the first GEM until all the charge is collected. This shape shows how the drift field affects the overall charge gain in the different krypton mixtures.

The plots show that pure krypton promotes a faster rise to plateau where absolute gain and energy resolution remain constant. This means that lower fields are required to achieve full electron collection; the inclusion of CO₂ in the mixture increases the electric field required to assure full collection of the primary electric charges. The plateau is reached at 50 V cm^{-1} in pure krypton, 150 V cm^{-1} in Kr-CO₂ (90:10) and 300 V cm^{-1} in Kr-CO₂ (80:20). Maximum gains above 10^3 were reached in all krypton mixtures.



(a) **Effective charge gain as a function of the drift field:** for pure krypton, lower electric fields are needed to assure full electron collection when compared to the other mixtures. (b) **Relative energy resolution as a function of the drift field:** for pure krypton there is no significant change, while for the remaining mixtures, there is a significant drop in energy resolution.

Figure 55: **Drift field optimization:** effective charge gain and relative energy resolution dependency of the drift field in the three krypton-based mixtures.

As for energy resolution, for pure krypton there is no significant variation with the applied electric field. In the (90:10) and (80:20) mixtures, however, a considerable drop in energy resolution values is visible. The minimum energy resolution was recorded for the same electric fields that maximized the charge gain.

11.4.2 Transfer region

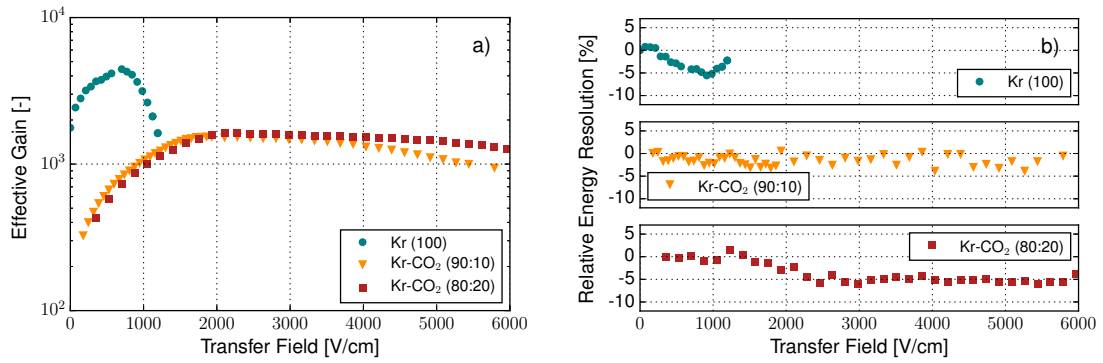
During this part of the study, the electric field between the bottom of the first GEM and the top of the second one, the transfer field, was changed while the remaining electric fields across the detector were kept constant at the values expressed in table 8.

Table 8: **Electric fields for the transfer region optimization:** the drift and induction fields implemented during the optimization of the transfer field are presented for each gas mixture.

	Kr (100%)	Kr-CO ₂ (90:10)	Kr-CO ₂ (80:20)
DRIFT FIELD (V/cm ²)	522	333	556
INDUCTION FIELD (V/cm ²)	500	1833	1500

Figure 56 shows the effective gains and energy resolution for each of the mixtures studied, as a function of the transfer field.

For the two mixtures with the presence of CO₂, a similar profile was recorded, showing a progress to high values of charge gain, followed by a slower drop to lower values, where an operation plateau can be found. Pure krypton also follows this overall profile, although with no defined plateau and a much faster degradation in charge gain. As the transfer field increases, the electrons are guided to the second GEM for the second amplification step. However, when the applied electric field is too high, the electrons become trapped in the top of the second GEM and that charge is lost, decreasing the overall charge gain.



(a) **Effective charge gain as a function of the transfer field:** pure krypton is the most sensitive to changes in the electric field, lacking a well-defined plateau. The other krypton mixtures, however, have similar profiles.

(b) **Relative energy resolution as a function of the transfer field:** for Kr-CO₂ (80:20), the energy resolution appears more stable than for the other mixtures.

Figure 56: **Transfer field optimization:** effective charge gain and relative energy resolution dependency of the transfer field in the three krypton-based mixtures.

Pure krypton measurements are the most sensitive to small changes in the electric field, reaching charge gains above 4×10^3 at 560 V cm^{-1} and then dropping rapidly to lower values. The krypton-CO₂ mixtures, present a different behavior, with a much less severe drop in the gain with increasing transfer fields. They have similar profiles with a maximum gain about 1.6×10^3 and a plateau of $\approx 1.5 \text{ kV cm}^{-1}$ where the effective gain does not change significantly.

For the three mixtures, energy resolution dropped around 5% from the first measurement, however no common pattern can be identified in these profiles. For pure krypton and the Kr-CO₂ (80:20) mixture energy resolution changes with increasing electric field, although with different profiles. For Kr-CO₂ (90:10) the behavior of energy resolution seems to be roughly independent of the changes in the transfer field. Nevertheless, a minimum value of energy resolution can be found for each mixture at the higher values of charge gain, allowing proper electronic optimization.

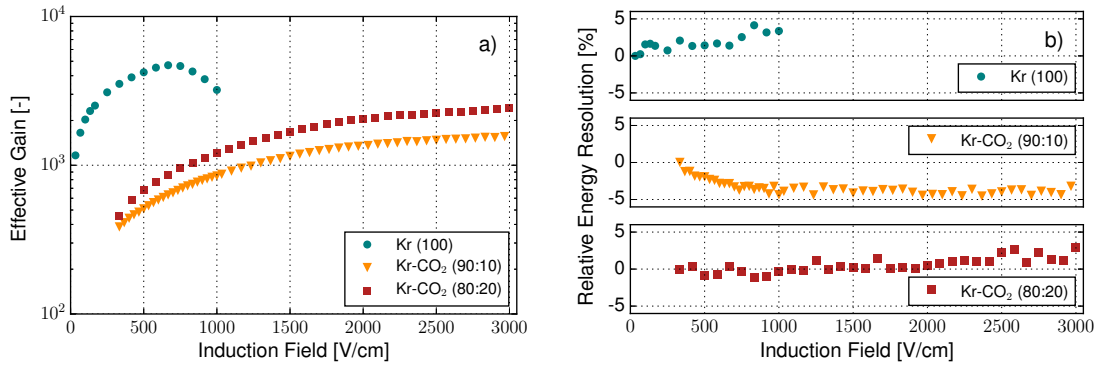
11.4.3 Induction region

To study the behavior of the detector as a function of the induction region, all the electric fields were kept constant (as seen in table 9) with the exception of the field between the bottom of the second GEM and the readout board.

Table 9: **Electric fields for the induction region optimization:** the drift and transfer fields implemented during the optimization of the induction field are presented for each gas mixture.

	Kr (100%)	Kr-CO ₂ (90:10)	Kr-CO ₂ (80:20)
DRIFT FIELD (V/cm^2)	522	333	556
TRANSFER FIELD (V/cm^2)	877	1404	1754

The results are shown in figure 57.



(a) **Effective charge gain as a function of the induction field:** although the Kr-CO₂ (90:10) and (80:20) mixtures follow the expected profile for this region, effective gain in pure krypton decreases for fields above 700 V cm⁻¹. (b) **Relative energy resolution as a function of the induction field:** for pure krypton and Kr-CO₂ (80:20) the energy resolution increases with increasing induction field. The (90:10) shows a progress towards lower values.

Figure 57: **Induction field optimization:** effective charge gain and relative energy resolution dependency of the induction field in the three krypton-based mixtures.

For krypton mixtures with the presence of CO₂ (figure 57a), extraction from the holes of the second GEM increases with increasing electric field. For the 90:10 mixture, an effective gain around 1.5×10^3 was measured near 3000 V cm⁻¹. For the 80:20 mixture, gains of 2.4×10^3 were achieved. Higher extraction fields could not be reached at the risk of discharges.

However, for pure krypton, a decrease in the effective gain occurs when electric fields above 700 V cm⁻¹ are applied, providing a maximum near 4.7×10^3 . This means that charge is being lost when subjected to higher electric fields. The measurements were repeated but similar results were obtained, calling for further investigation.

Energy resolution increases for higher transfer fields in pure krypton and Kr-CO₂ (80:20) measurements. The (90:10) mixture, however, presents a different profile, with decreasing energy resolution values until a plateau is reached. As a result, only this mixture combines higher values of charge gain with lower values of energy resolution for the transfer region. For the other two, optimal conditions were agreed for maximum values of charge gain where the energy resolution is not very high and roughly constant.

While gas mixtures containing CO₂ showed defined operation plateaus, pure krypton did not, which means that very stable electric conditions are required to avoid charge gain and energy resolution fluctuations for the latter.

11.5 SIGNAL OPTIMIZATION FOR THE IMAGING STUDIES

The DPP-PHA Control Software allows the personalization of many parameters associated with the digital operations applied to the detector signals during image acquisition. The optimization of these constants was made for each channel separately to achieve an overall profile similar to the one shown in figure 30. The parameters used during image acquisition are presented below:

- **DC offset (35%):** sets the baseline of the input signal as zero;

- **Pulse polarity** (Positive): selects the polarity of the incoming signal from the preamplifier;
- **Threshold** (240 LSB): sets the minimum input value to set the trigger;
- **Smoothing factor** (2): size of a moving average filter used to minimize the high frequency noise of the input signal;
- **Holdoff** (10 μ s): reduces pile-up probability, setting the minimum interval between two consecutive triggers;
- **Decay time** (20 μ s): relates to the exponential decay time constant of the input pulses. When this value is not well set, the trapezoid top may not be flat (as seen in figure 30);
- **Rise time** (1 μ s): it is the value of rise and fall time of the trapezoid. While higher rise times enable higher SNRs, they also increase the probability of pile-up occurrence;
- **Flat top** (2 μ s): sets the width of the top of the trapezoid;
- **Baseline mean** (64): number of baseline samples to be averaged. These will determine the reference value to calculate the trapezoid's height;
- **Peaking delay** (0.5 μ s): sets the position within the flat top used to determine its height;
- **Peak mean** (1): the number of samples to be averaged to determine the height of the trapezoid;
- **Baseline holdoff** (0.1 μ s): time break in the baseline determination whenever a trapezoid signal appears. This pause is needed to give rise to the trapezoid appearance;
- **Peak holdoff** (1 μ s): sets the time between two trapezoids.

A minimal adjustment to these parameters was punctually made to enhance the signal processing during image acquisition, mainly regarding the *threshold* parameter. The individual input signals (visualized with the aid of the oscilloscope mode) adopted different shapes and behaviors, which complicated the task of properly shaping all the signals. Instead, an effort to successfully shape the maximum number of input signals was made.

CHAPTER OVERVIEW

The response curves for electronic, position and energy calibration were determined by imposed standards to find the relation between the output measurement and the real values of charge gain, dimension in cm and energy, in keV.

The optimum conditions that guarantee maximum performance in charge gain and energy resolution for different gaseous mixtures are systematized in table 10.

The electric fields that were chosen imply both a stable plateau with high absolute gain and a constant region of relative low energy resolution. These were the setup

Table 10: **Optimized electric conditions for krypton mixtures:** the optimized values for the drift, transfer and induction fields are presented for pure krypton, Kr-CO₂ (90 : 10) and the Kr-CO₂ (80 : 20) mixture.

	DRIFT (V cm ⁻¹)	TRANSFER (V cm ⁻¹)	INDUCTION (V cm ⁻¹)	GEM _{1/2} (V)
Ar-CO ₂ (70:30)	1444	2737	1667	580
Kr 100%	200	649	583	535
Kr-CO ₂ (90:10)	278	2351	3333	550/580
Kr-CO ₂ (80:20)	278	2351	3333	605
Kr-CO ₂ (70:30)	167	2210	3333	650
Kr-CO ₂ (60:40)	167	2210	3333	685

values used in the following measurements for the correspondent gaseous mixture unless other ones are presented. Although only three of these mixtures were characterized, the behaviors of the other krypton-based mixtures were extrapolated from the measured data. The electric fields used for the Ar-CO₂ mixture were extracted from the logbook correspondent to the work referenced in [4].

These measurements and operation modes proved themselves to be unaffected by the *charging up* effect or other phenomena that implies measurement fluctuation over time.

For the optimized conditions determined in the last chapter, the stability, charge gain, energy resolution, signal-to-noise ratio and spatial resolution are measured. These are quantitative parameters capable of assessing the quality of the developed MPGD.

12.1 TIME STABILITY

Because the image acquisition process may take several minutes to achieve adequate statistics, it is fundamental to guarantee that there is no significant change in charge gain values over time. Unknown fluctuations during image acquisition may lead to loss of energy and position resolution, which affects the overall quality of the final images. To evaluate this behavior, the energy spectra of a ^{55}Fe source was evaluated for 240 s, each 15 min, during a total time of 200 min. This procedure was implemented for pure krypton and for the (90:10) and (80:20) Kr-CO₂ mixtures. The results are shown in figure 58.

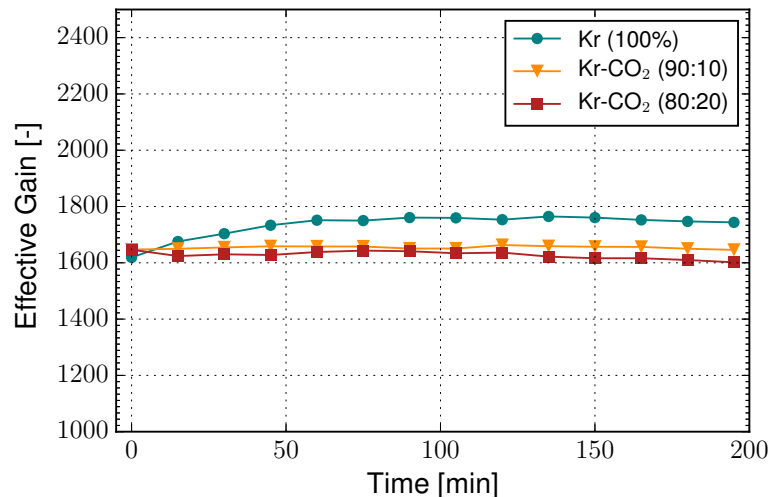


Figure 58: **Time stability of charge gain:** for three krypton based mixtures, the charge gain was measured over time, under the same experimental conditions. The value of charge gain suffered no significant fluctuations that could affect future image acquisition.

According to the profiles of charge gain, no significant fluctuations were recorded over time. However pure krypton shows a gradual increase of charge gain before the 50 min running time, this might be an indicator that the electric conditions were not yet completely stable. Nevertheless, these changes in the values of charge gain will not influence the image formation process significantly. Even so, a constant care regarding charging up effects was taken throughout the entire course of the experimental work, as they could affect the charge gain of the detector during the acquisitions.

12.2 SPATIAL UNIFORMITY

The uniformity studies were performed with the ^{55}Fe source, and with the aid of a $(100 \times 100) \text{ mm}^2$ perforated grid that covered the total active area of the detector. This matrix had the configuration and dimensions shown in figure 59.

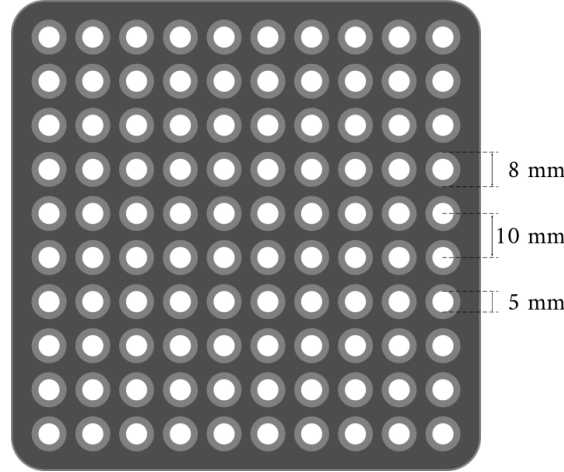


Figure 59: **Perforated grid used to study the uniformity of the detector:** the 10×10 hole matrix contains 5 mm collimators with a separation of 10 mm.

The x-ray source was sequentially positioned inside each collimator and a 30 s image was recorded. These measurements were made with a pure krypton flow of 2 L h^{-1} .

For a single position, the acquired image provided information about the charge gain, energy resolution, distortion and vertical and horizontal FWHM variation along the detector's active area.

12.2.1 Charge gain and energy resolution

The energy spectra of each image was evaluated and fitted to a normal distribution (equation 34). The charge gain and energy resolution values (centroid and FWHM(%) values, respectively) were determined for each spectra and plotted according to the position of the x-ray source. The results are shown in figures 60 and 61.

The charge gain behavior (figure 60) adopts the expected shape as described in [54]. The higher charge gain values measured at the borders of the active area are a consequence of the readout plate configuration. Events located at the center of the plate, suffer more attenuation along the resistive line when compared to the ones recorded near the outer limits. An average gain of 6.9×10^3 was recorded, with a maximum fluctuation of 16.72% relatively to this value.

Regarding the energy resolution mapping, no overall tendency could be determined. The upper right corner showed the highest values of energy resolution, achieving a maximum of 27.63% (FWHM). In this region, the spectra of the x-ray source appeared as an asymmetric distribution, with an extended descent towards high energies. The mean value of energy resolution along the detector's area was 21.01%.

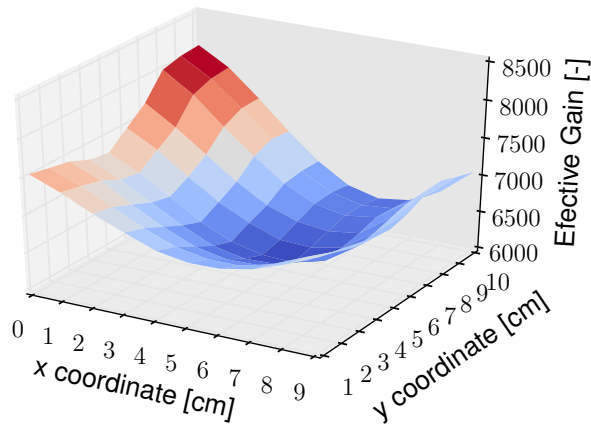


Figure 60: **Charge gain variation with position:** the average charge gain was 6.9×10^3 and a maximum relative fluctuation of 16.72% was recorded at the edges.

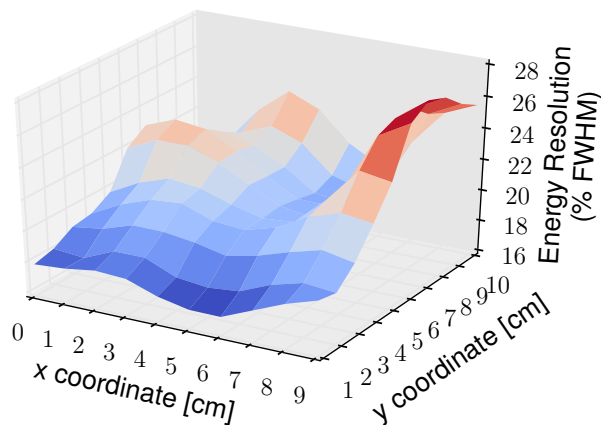


Figure 61: **Energy resolution variation with position:** the average energy resolution was 21.01% and a maximum relative fluctuation of 31.51% was recorded (at the edges).

12.2.2 Image distortion

To evaluate the distortion associated with the experimental setup and the reconstruction algorithm, the images of the x-ray source were analyzed. By determining the vertical and horizontal projections of each image and fitting these profiles to a normal distribution, the position of the point source was calculated. This algorithm was previously described in 9.2.1 and illustrated in figure 45.

The results are plotted in figure 62, where each vertex corresponds to the location of the point source. The horizontal and vertical lines were plotted to “guide the eye” in a qualitative evaluation of the distortion.

Ideally, the crossing points in figure 62 should be equally spaced, as the x-ray source was positioned always with the same pitch. Nevertheless, there is a visible distortion, mainly near the limits of the detector’s window. This distortion may be a consequence of the resistance fluctuations associated with the resistive line of the readout plate.

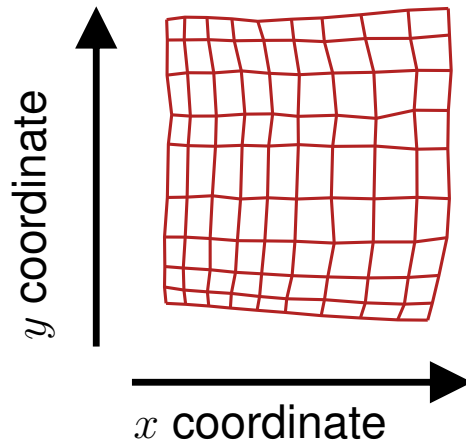


Figure 62: **Geometric distortion of the detector:** for each image acquisition, the position of the point source was determined within the active area of the detector.

Reference [4] already remarked this effect but with a more prominent pincushion-type distortion. The minimization of the deformation achieved in figure 62 is mainly due to the reconstruction algorithm already described in 9.1.3.

12.2.3 Position resolution

Using the same methodology as the one described in the last section, the FWHM of the horizontal and vertical projections of the image was determined. Because the ^{55}Fe source is not truly an infinitesimal point source, the absolute value of the FWHM does not correspond to the position resolution of the system. Nevertheless, the relative values of the vertical and horizontal FWHM are directly related to the fluctuations in the overall position resolution of the system.

The experimental data is plotted in figures 63 and 64. The horizontal FWHM was measured along the x coordinate, while the vertical FWHM was measured along the y axis.

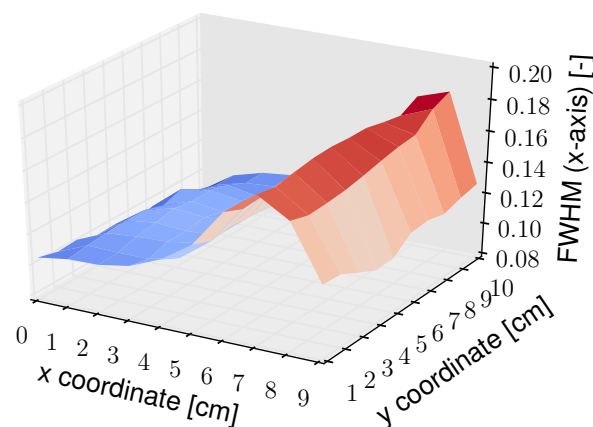


Figure 63: **Horizontal FWHM uniformity:** the right side of the detector shows higher values of FWHM (measured in the x axis) when compared to the left side.

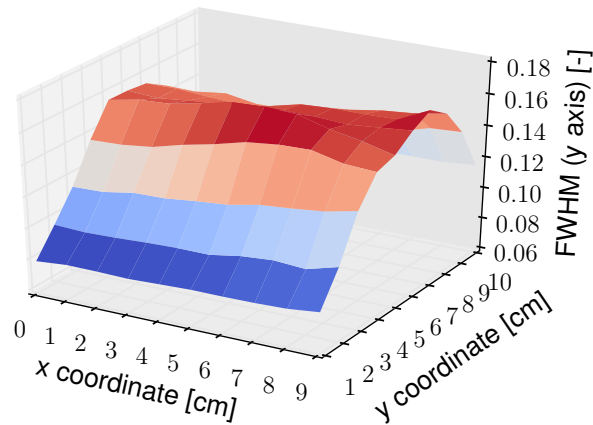


Figure 64: **Vertical FWHM uniformity:** the central layer of the detector comprises higher values of FWHM (measured in the y axis) when compared to the top and bottom area.

The FWHM measured in the horizontal axis (figure 63) has similar values along the vertical axis of the image, varying in the horizontal coordinate. The left side of the detector is the region that presents the lowest values of FWHM and with small fluctuations. However, in the right side of the active area, the values of the FWHM degrade up to 42.52% relatively to the average value.

The FWHM measured in the vertical axis (figure 64), on the other end, has small variations along the horizontal axis while presenting big fluctuations along the y coordinate. Furthermore, the vertical FWHM suffers a gradual degradation, lacking a region where its values remain constant. Nevertheless, the overall fluctuation in the FWHM value is much lower than the one measured for the horizontal FWHM, with a maximum of 27.82% relatively to the average value. These variations show that the developed MPGD is a non-stationary system, as the PSF is not maintained along the detectors' active area.

Taking all these considerations into account the upper left region of the detector was chosen to locate the RoIs during the following quantitative measurements. This region assures high values of charge gain and average values of energy resolution. It is also the region where the distortions are less pronounced and the horizontal spatial resolution remains roughly constant in this region. Although it is the worst area for the vertical position resolution, a choice was made to evaluate the horizontal position resolution alone.

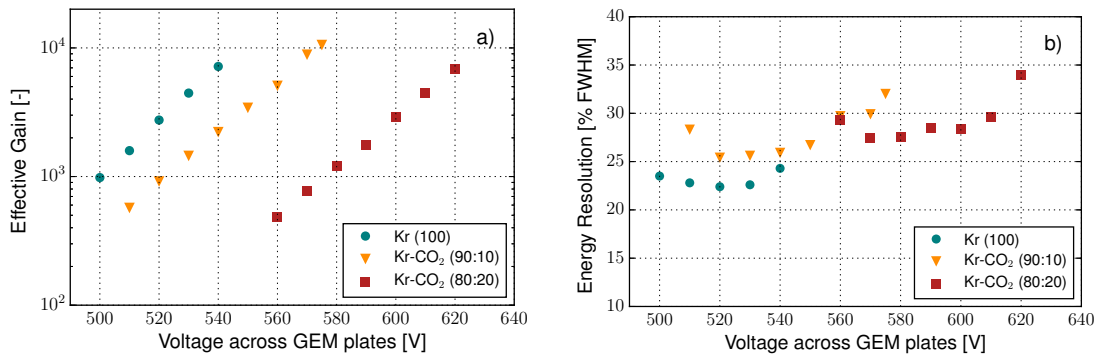
12.3 CHARGE GAIN AND ENERGY RESOLUTION

The charge gain (figure 65a) and energy resolution (figure 65b) of the double G-100 cascade were studied as a function of the voltage difference across the GEM foils, ΔV_{GEM} for the optimal setting in table 10. For each gas mixture, both foils were biased with the same voltage difference, as it was assumed the foils had similar performances.

The electric fields selected for the drift, transfer and induction regions were the ones shown in table 11. These are different from the ones shown in table 10 because the charge gain and energy resolution measurements were taken before the final optimum

Table 11: **Electric fields used for the charge gain and energy resolution study:** the drift, transfer and induction fields applied are presented for pure krypton and the Kr-CO₂ (90:10), Kr-CO₂ (80:20) mixtures.

REGION	PURE KRYPTON (V cm ⁻¹)	90:10 (V cm ⁻¹)	80:20 (V cm ⁻¹)
DRIFT	200	333	310
TRANSFER	650	1930	2800
INDUCTION	580	2500	1500



(a) **Charge multiplication as a function of the voltage across the G-100 plates :** all mixtures present an exponential behavior with increasing ΔV_{GEM} . The measurements were made until the sparking limit was reached. (b) **Energy resolution as a function of the voltage across the G-100 plates:** for pure krypton, energy resolution lies around 22%, as for the Kr-CO₂ (90:10) and (80:20) mixtures a minimum value of 25% and 27% were recorded, respectively.

Figure 65: **Charge gain and energy resolution:** charge multiplication and energy resolution as a function of the voltage across the G-100 plates.

graphs were plotted and analyzed. However, the electric fields used in this study still guarantee the optimum electric conditions in each MPGD region (see figures 55, 56 and 57). The ⁵⁵Fe source was collimated to 1 mm diameter and a thin Cr foil was used to filter the K_β line. The measurements were made until the discharge limit in the GEMs was reached.

The first visible aspect in figure 65a is the exponential growth of charge gain with increasing applied voltage between the G-100 plates. This is the expected behavior, as it is compatible with the Townsend avalanche mechanism.

The highest charge gain (10.5×10^3) was achieved for the Kr-CO₂ (90:10) mixture for $\Delta V_{\text{GEM}} = 575$ V. Using pure krypton, a maximum gain of 7.2×10^3 was reached before the onset discharges, while for the Kr-CO₂ (80:20) mixture, the highest measured gain was 6.8×10^3 .

Furthermore, as the concentration of CO₂ increases, higher voltages, ΔV_{GEM} are required to achieve the same level of charge gain. Degradation in energy resolution also occurs with increasing value of CO₂; for pure krypton the minimum energy resolution was 22.40% as for the Kr-CO₂ (90:10) and (80:20) mixtures values near 25.40% and 27.48% were recorded, respectively. The value of energy resolution for each mixture is a fundamental factor to take in mind during image analysis. This is true because the

reconstruction algorithm (described by equation 32) relies on how precise the energy information is recorded by the imaging system.

A histogram of the normalized pulse height amplitudes for the Kr (100%) and Kr-CO₂ (80:20) mixtures is represented in figure 66. As the CO₂ concentration increases, the spectrum widens, which illustrates the energy resolution degradation already quantified in figure 65b. The spectra obtained with the Kr-CO₂ (90:10), although not represented along with the others, followed the same Gaussian profile, with an intermediate width.

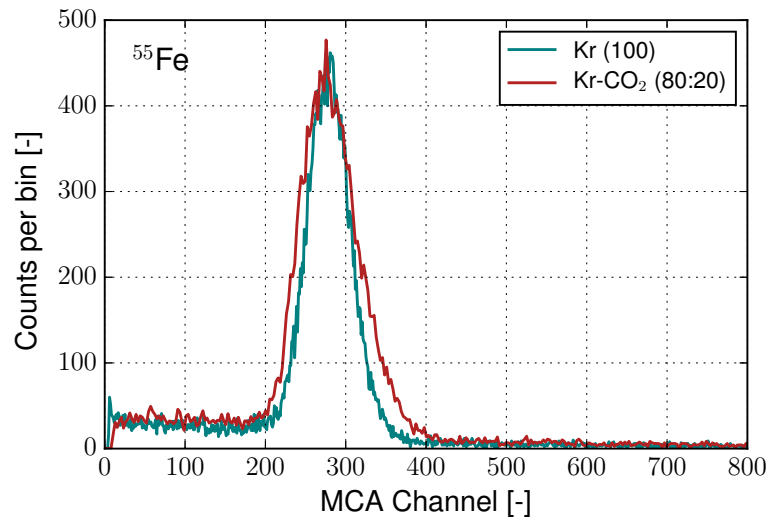


Figure 66: **Pulse height distribution for pure krypton and Kr-CO₂ (80:20)**: energy resolutions measured in Kr 100% and Kr-CO₂ (80:20) were, respectively, 22 and 27% (FWHM).

According to the work referenced in [72], the maximum charge gain obtained with Kr-CO₂ (90:10) with a double standard-GEM cascade was 10^3 which is smaller than the value achieved with the G-100 cascade. This result shows that G-100 performs similarly to standard GEMs, with the additional advantage of better withstanding sparking.

For Ar-CO₂ using the same detection system (work [4]), the final charge gain was similar to the Kr-CO₂ (90:10) mixture (10^4). Regarding energy resolution, the values achieved for Kr-CO₂ (90:10) are close but still superior to the ones recorded for Ar-CO₂ (70:30). However, this difference does not compromise the usage of krypton mixtures for x-ray imaging.

12.4 SIGNAL-TO-NOISE RATIO

To measure the image's SNR, an uniform, squared RoI of 0.25 cm^2 was chosen within the rectangular window of the images presented in appendix B. To allow a direct comparison between the measured SNR values, the RoIs were positioned according to the methodology illustrated in figure 67. Firstly, the position of the right, a_x , and top edges, a_y , of the rectangular window was determined by its ESF profile. The RoI was designed to be distanced 0.4 cm from a_x and 0.2 cm from a_y , while assuming a square shape with 0.25 cm^2 . These values were defined to place the RoI in an uniform region; near the left edge of the window, (but after its edge) and equally spaced to the top and bottom edges of the window. This procedure was applied to the acquired image for each gaseous mixture represented in appendix B.

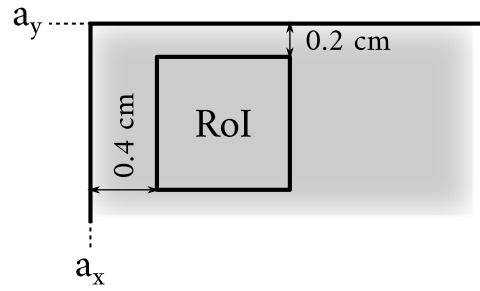


Figure 67: **RoI determination for image SNR calculation:** the RoI was selected using pre-determined distances to the vertical and horizontal edge positions (a_y and a_x , respectively).

The SNR value of each RoI was calculated using the tool described in 9.2.4 and compared to the standards presented in table 3. The results are shown in figure 68.

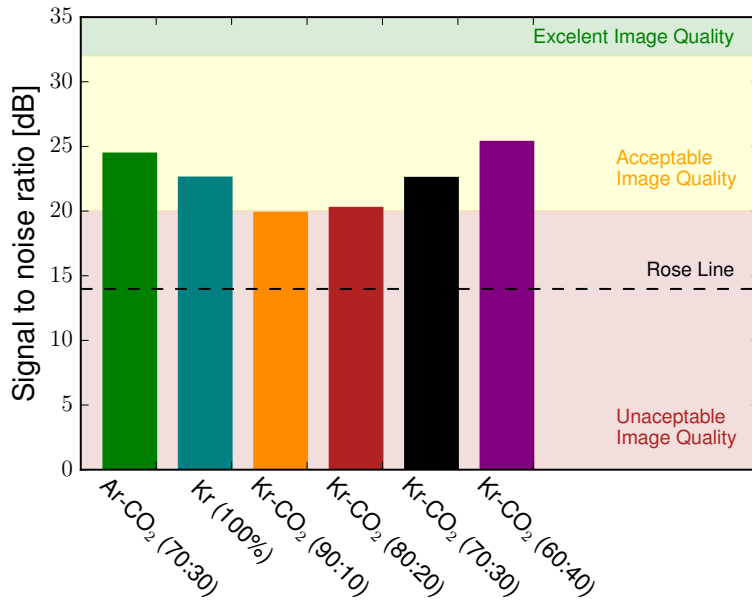


Figure 68: **Image SNR of different krypton-based mixtures:** the SNR value (in dB) of the mixtures is represented as a bar plot. The Rose line (black) and the ISO 12232 – 2006 regions (red, yellow and green) are also presented.

As it can be seen, all the images are well above the Rose line (located at 13.97 dB), meaning that the objects within the images are successfully recognized. Evaluating them under the ISO 12232 – 2006 standard, most images (with the sole exception of the 90:10 mixture), achieve an acceptable image quality status, comparable to the performance of a digital still camera. The Kr-CO₂ (90:10) mixture, although below this line, is very close to the lower limit of the acceptable image quality region.

The plot also suggests that, for the Kr-CO₂ mixtures, the SNR value improves with the presence of carbon-dioxide, achieving its maximum value for the 60:40 mixture. The SNR of the Ar-CO₂ (70:30) image was also determined for comparison purposes and its value was only surpassed by this last Kr-CO₂ mixture.

12.5 SPATIAL RESOLUTION

The spatial resolution of the images acquired with krypton-based mixtures was measured by selecting a ROI containing a sharp edge, as described in 9.2.3. The images used for this study are presented in appendix B, where the left limit of the rectangular window provided the necessary information for the ESF determination. These images were acquired using the x-ray generator, imposing a tube voltage around 30 keV and the maximum limiting current that prevented the saturation of the readout board (generally, below $1 \mu\text{A}$).

For each acquisition, a set of sub-images was reconstructed from the original one by sectioning the total energy histogram into sequential energy regions 2 keV wide, starting at 2 keV. The position resolution was then measured for each sub-image, using the edge-gradient method. The gaseous mixtures evaluated were, once more, Kr (100%), Kr-CO₂ at (90:10), (80:20), (70:30) and (60:40) and an Ar-CO₂ (70:30) mixture for comparison purposes.

The measurements of spatial resolution were made until the statistics of the sub-image prohibited their calculation. Punctually, the fitting algorithm did not converge for certain sub-images.

The results obtained with this study are presented in figure 69. Fitting the ESF to the Gauss-error function for all sub-images at once (with a fixed ROI) was a very challenging operation, so the error bars in the plot represent the fit quality of the edge profile to equation 37, and its influence in the FWHM calculation of the LSF.

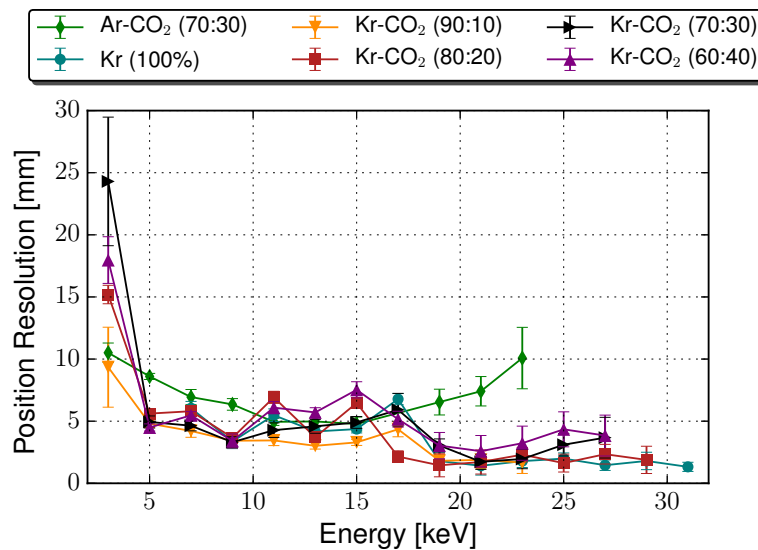


Figure 69: **Position resolution as a function of radiation energy:** for the krypton-based mixtures, the spatial resolution value remains at low values for energies above the 18 keV threshold. The error bars quantify the ESF goodness of fit to the Gauss-error function.

It is clearly visible that krypton-based mixtures show a very different behavior for higher energies when compared to the argon mixture. As already reported in [4], the spatial resolution of argon mixtures (green) is affected by the electronic SNR below 15 keV (position resolution minimum). After this threshold, the spatial resolution starts to increase progressively due to the photoelectron range effect. This behavior for high energies is also reported in figure 14.

Krypton-based mixtures, however, show a very different profile for energies above 18 keV, where the correspondent spatial resolution remains at low values. This is the expected result according to figure 14, where the spatial resolution for krypton drops near the 15 keV value. Nevertheless, in figure 69, the spatial resolution decrease only happens for energies higher than 18 keV. This can be a consequence of the 12.649 keV fluorescence photons produced for energies slightly higher than the krypton's absorption edge.

Although the absolute values of position resolution are not remarkable¹, the relative behavior between argon and krypton mixtures is according to the theoretical previsions. Moreover, the fact that the spatial resolution for krypton is maintained at its minimum for a longer energy interval, enables the acquisition of more detailed images, being an undeniable advantage for x-ray imaging.

12.6 CONTRAST RESPONSE

After the position resolution study, the MTF was determined for each mixture, for the sub-image reconstructed within the 22 – 24 keV interval. The correspondent functions are represented in figure 70.

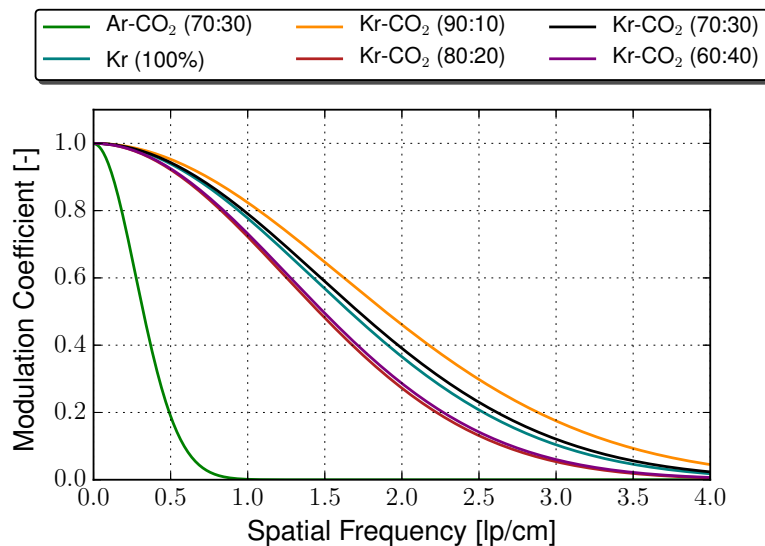


Figure 70: **MTF for energies within the 22 – 24 keV range:** while the Ar-CO₂ mixture revealed a MTF value at 10% of 0.5876(342) lp/cm, the minimum value recorded for a krypton-based mixture was 2.6609(1) lp/cm.

Evaluating the contrast attenuation as a function of the spatial frequency, once more, krypton mixtures reveal themselves as more adequate for imaging purposes. While the Ar-CO₂ suffered a 10% drop in contrast for a spatial frequency of 0.5876(342) lp/cm (which is consistent with the result reported in [7], for a 5×5 cm² readout), the Kr-CO₂ (80:20) mixture only suffered this decrease at 2.6609(1) lp/cm. The best response to contrast is associated with the Kr-CO₂ (90:10) mixture, whose MTF value at 10% happens at 3.2702(15) lp/cm. However, the MTFs for the different Kr-based mixtures have very similar profiles, surpassing the performance of the Ar-CO₂ (70:30) mixture.

¹ In [4], the minimum position resolution for Ar-CO₂ (70:30) was 1.69 mm, while in this work a 4.94 mm value was measured. Consequently, the spatial resolution values measured for the krypton mixtures should also be much lower.

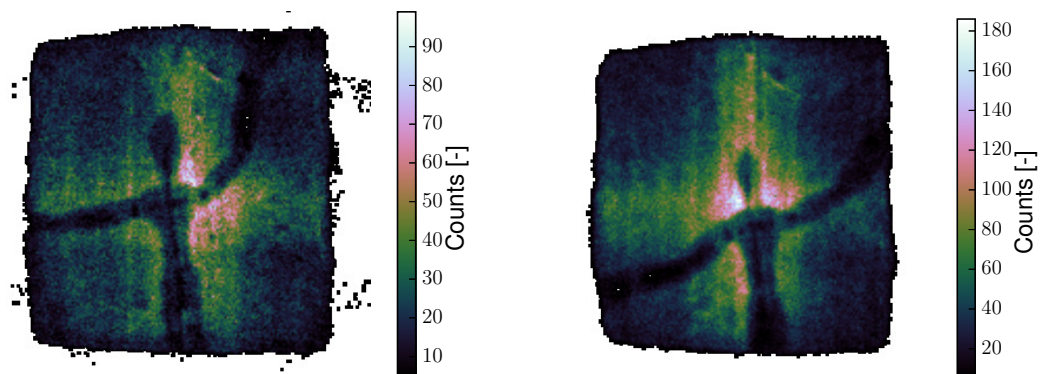
12.7 IMAGING CHARACTERISTICS

As to evaluate the upcoming potentials of the developed imaging system, more complex profiles were imaged. These objects were previously presented in chapter 7. Although the following images were not analyzed quantitatively, the qualitative information they provide is of interest.

12.7.1 Wood mannequin

This type of imaging system, by recording energy and time simultaneously, allows the filtering of certain energy ranges during image reconstruction. This feature was already described in [4] and allowed the enhancement of certain objects of the wooden dummy by selecting narrower regions of the energy spectrum.

The images of the wood dummy (figure 37) taken for the Kr-CO₂ (90:10) and (80:20) mixtures are presented in figure 71.



(a) Image acquired for Kr-CO₂ (90:10) with 18 keV and 0.001 mA limiting current. The image reconstruction was made using events within the 10 – 18 keV range.

(b) Image acquired for Kr-CO₂ (80:20) with 20 keV and 0.010 mA limiting current. The image reconstruction was made using events within the 14 – 20 keV range

Figure 71: Wooden dummy imaging for Kr-CO₂ mixtures: the acquisitions were made by positioning the wood mannequin at half distance between the x-ray source and the detector window. The images were reconstructed using a narrower energy interval. Higher energies were chosen to better feature the details of the mannequins.

By choosing the higher energies of the spectra, the details of the object were further enhanced from the original images. The contrast of the wooden body is visibly higher and more easily distinguishable from the background. The metallic spring was also better resolved in both Kr-CO₂ mixtures.

The successful imaging of this object shows the imaging system's potential to perform medical imaging, being able to distinguish wood (with similar x-ray response to the soft tissues of the human body) from the metal spring (comparable to the bones and other biological hard structures).

12.7.2 Music box

The music box was also imaged with a Kr-CO₂ (90:10) flow, with a 20 keV and $\leq 1 \mu\text{A}$ limiting current setting in the x-ray generator. The acquisition was made with no

magnification and was reconstructed for energies within the range 14 – 20 keV. The resultant image is shown in figure 72.

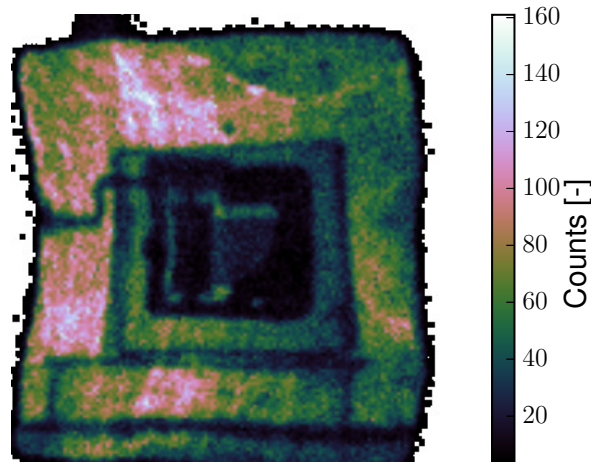


Figure 72: **Music box imaging for Kr-CO₂ (90:10)**: this acquisition was made for 20 kV and $\leq 1 \mu\text{A}$ limiting current. The music box was placed the closest possible to the detector's window and an energy filtering of 14 – 20 keV was applied during the image reconstruction.

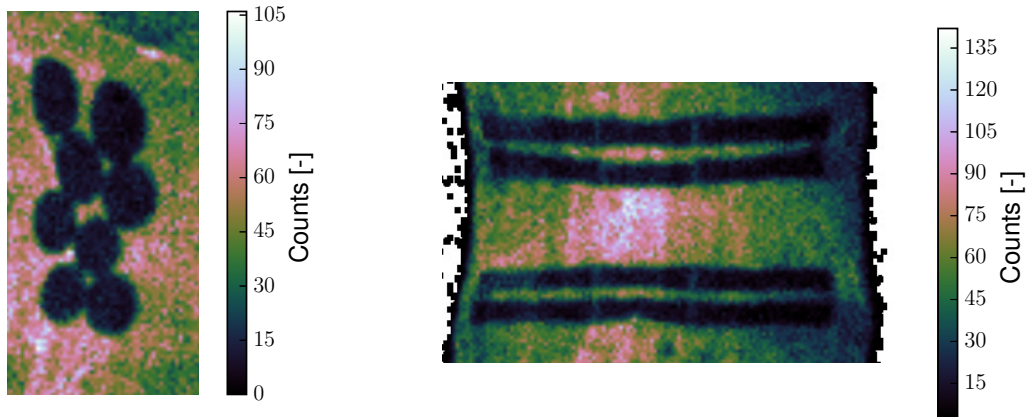
All the metallic pieces are clearly visible, especially the barrel, the cylindrical drum and the frame. The vibrational plate appears with slightly higher intensity values than the compact regions of the music box. This happens because some photons pass through the gaps between the comb teeth of the vibrational plate. The wood base in which the music box is supported is also distinguished from the uncovered area of the detector. The rectangular shape of this structure is evident. With the aim of centering the music box with the detector window, a cylindrical plastic lid was used as a vertical support. The contours of this auxiliary piece are also clear at the bottom of the image.

12.7.3 Geomag® kit

The steel spheres and the magnetic rods of the Geomag® kit were imaged inside the polystyrene box, with a setting of 20 keV and a limiting current of $\leq 1 \mu\text{A}$. The steel balls are shown in figure 73a, while the magnetic rods are presented in figure 73b. Both images were reconstructed using an energy filtering of 14 – 20 keV.

The eight steel spheres that constitute the kit can be easily distinguished from each other and from their surroundings. The bottom four spheres appear more symmetrical, while the ones located at the top of the detector window show distortions along the vertical coordinate. Nevertheless, the limits of the steel spheres are well defined, with an abrupt change in pixel intensity.

The twelve magnetic rods can also be individually distinguished from each other, even though the horizontal distance between them (imposed by the strong magnetic attraction) was very small. A shape deformation in the outer regions of the detector is also visible. The left and right rods appear longer than the ones positioned at the center, although they all have the same size. Furthermore, the parallel disposition between the four-group rods is more apparent for the bottom six cylinders. For the



(a) Steel balls imaging for Kr-CO₂ (90:10).

(b) Magnetic rods imaging for Kr-CO₂ (90:10)

Figure 73: **Geomag kit imaging for Kr-CO₂ (90:10)**: these acquisitions were made for 20 kV and $\leq 1 \mu\text{A}$ limiting current. The polystyrene box was placed at minimum distance from the detector's window and an energy filtering of 14 – 20 keV was applied during image reconstruction.

top set, the vertical distance between the rods varies, increasing for the central rods relatively to the distance between the top and bottom edge rods.

CHAPTER OVERVIEW

The most relevant quantitative results determined throughout this chapter are presented in table 12.

Table 12: **Quality parameters of krypton mixtures**: the maximum charge gain, \mathcal{G} , minimum energy resolution, R_e , position resolution, R_p , MTF value at 10% and the SNR determined experimentally are presented for Ar-CO₂ (70:30) (Ar), pure krypton (100%) and the remaining Kr-CO₂ mixtures. The presented position resolution and MTF_{10%} values correspond to the 22 – 24 keV interval.

	\mathcal{G}	R_e (%)	R_p (mm)	MTF _{10%} (lp/cm)	SNR (dB)
Ar	-	-	10.08(247)	0.5876(342)	24.45
100%	7.2×10^3	22.40	1.78(52)	3.0252(4)	22.59
90:10	10.5×10^3	25.40	1.67(88)	3.2702(15)	19.87
80:20	6.8×10^3	27.48	2.30(58)	2.6609(1)	20.25
70:30	-	-	1.95(78)	3.1304(6)	22.57
60:40	-	-	3.23(137)	2.7136(1)	25.36

In terms of charge gain, the advantages of using a G-100 instead of a standard GEM plate allowed the imposition of higher electric fields with a low chance of sparking damage. Consequently, charge gains above 10^3 were recorded. The addition of carbon-dioxide to the krypton mixtures meant that higher electric fields needed to

be applied to achieve the same value of charge gain, while degrading the value of position resolution.

The detector was also evaluated in terms of uniformity revealing that the objects should be centered relatively to the detector's window to assure they were imaged properly.

The SNR of the acquired images satisfied the Rose Criterium and, with the exception of the Kr-CO₂ (90:10) mixture, the ISO 12232 – 2006 standard, achieving a status of *acceptable image quality*.

Krypton-based mixtures showed lower values of position resolution when compared to argon mixtures for energies above the 18 keV threshold. Furthermore, the contrast of images acquired with krypton mixtures decreases more slowly with increasing spatial frequency. This means that with krypton more detailed and contrasting images can be produced in x-ray imaging applications.

Analyzing several images acquired with complex and "real-life" objects, the imaging system demonstrated great potential to distinguish them and replicate their shape. Nevertheless, distortion effects remain the most challenging factor to overcome.

13.1 CONCLUSION

This project was developed under the objective of evaluating the performance of an x-ray imaging detector, based on a double cascade of non-standard GEMs, made of a 100 mm thick kapton foil. Being twice as thick as a standard GEM plate, these foils are more tolerant to sparking-caused damage, which allows the imposition of stronger electric fields and the achievement of higher charge gains.

This detector was operated under different krypton-based mixtures and Ar-CO₂ (70:30), for comparison purposes. The decision to use krypton mixtures for imaging acquisition is supported by [8]. In this work, krypton is reported to be the noble gas with the lowest value of position resolution within the 14 – 34 keV energy range. The images were obtained using the charge division method, allowing the reconstruction of each interaction event within a two-dimensional area. With the minimalistic layout of the readout board, only four electronic channels were necessary to collect the information for each acquired image, simplifying the image reconstruction process in terms of signal processing and software effort. The detector had an active area of $10 \times 10 \text{ cm}^2$

After the cleaning and the detector assembly within the detection system, optimization and calibration procedures were imposed to guarantee stable and optimum operation conditions, as well as rigorous measurements in terms of energy and position values. Using this information, the actual performance of the detector was measured in terms of charge gain, energy resolution, overall uniformity, image SNR, spatial resolution and contrast response. In parallel to the experimental work, an analysis software which allowed image reconstruction and quality assessment was developed.

The results showed that charge gains above 10^3 and close to 10^4 were achieved for krypton-based mixtures, mainly due to the robustness of the G-100 plates. A minimum energy resolution value of 22.40% was achieved for pure krypton. This value degraded with increasing concentration of CO₂. The SNR measurement revealed a satisfactory set of images, all of them satisfying the Rose Criterium, and most of them according to the ISO 12232 – 2006 standard. The most relevant results of this work are related to the behavior of krypton's position resolution with increasing radiation energy; while the spatial resolution for argon mixtures is known to degrade after 15 keV, krypton mixtures assure a low value of position resolution up to 30 keV. These observations are compatible to the study developed in [8]. Furthermore, krypton-based mixtures offer a better contrast response with spatial frequency increase when compared to argon mixtures. Consequently, krypton was proven to be a more suitable gas medium for MPGD operation, as its usage assures more detailed and contrasting images.

Although the different krypton mixtures showed very similar performances, the Kr-CO₂ (90:10) mixture appeared to be the most suitable for imaging applications. Firstly, it was the one that supported higher charge gains (surpassing the value 10^4) with lower GEM biasing voltage, along with relative intermediate values of energy resolution (minimum of 25.40%). However it was the mixture with a lower value of SNR, the Rose Criterium was still satisfied and the result was very close to the *acceptable image quality* region of the ISO 12232 – 2006 standard. Regarding spatial resolution, it was the mixture that revealed a more uniform profile, achieving a minimum of

1.67(88) mm for the 22 – 24 keV energy range. The contrast response of the (90:10) mixture was also the best, achieving an MTF value at 10% of 3.2702(15) lp/mm, for the same energy interval. Consequently, this was the chosen mixture to image more complex targets, where the correspondent fine details and shapes could be visually distinguished.

13.2 APPLICATIONS

The usage of a G-100 cascade along with a gas medium composed by krypton can be coupled to many systems that rely on radiation imaging, as this system enables the development of a robust and spatial sensitive imaging detector. As a consequence, it constitutes a viable alternative for some of the radiation detectors used currently in many different fields.

Perhaps the most common area of application is the medical imaging field, in devices designed to perform *scintigraphy*¹ or *positron emission tomography*.

X-ray fluorescence spectroscopy is also a possibility. This method allows the mapping of different elements present in a given sample as long as they emit fluorescence x-rays when subjected to a high-intensity x-ray source. Because the developed system offers an improved spatial resolution and high contrast features, more delicate and intricate samples could be evaluated under this procedure.

13.3 FUTURE WORK

Although the overall performance of the detector increased in many aspects from the one developed in [4], there are some aspects that could be further improved, such as the reduction of the electronic noise that affects the detector. Because the electronic SNR limits the position resolution for lower energies, a stable operation is fundamental to use the lower energies of the spectrum for image reconstruction. The electronic noise could be minimized by optimizing the capacitances of the charge sensitive preamplifiers and further isolating the experimental setup from external noise sources.

Also regarding the position resolution measurement, the absolute values achieved with this detector are still far from the expected results. This justifies a further optimization of the imaging system to minimize the detector limitations and lower the values of spatial resolution. The fact that the spatial resolution for krypton only drops after 18 keV instead at the expected 14 keV is also a matter of further investigation and can be related to the 12.649 keV fluorescence photons that, when interacting with the gas' atoms, contribute with a low resolution signal, as the radiation energy is below the krypton's absorption edge.

The uniformity of the detector could also be improved, mainly regarding the horizontal and vertical position resolution, which affected some regions at the center of the detector. Distortion minimization and correction tools (applied *a posteriori*) are also a factor of interest for future studies.

Finally, the analysis software could be further developed by implementing state-of-the-art processing tools to enhance the contrast of the images and reduce the artifacts that influence the overall image quality.

¹ imaging device supported by a scintillation counter along with a radioactive tracer

BIBLIOGRAPHY

- [1] E. Curie, *Madame Curie*, 8th ed., William Heinemann LTD, Ed., trans. from the French by V. Sheean, ch. War, pp. 282–283.
- [2] G. F. Knoll, *Radiation Detection and Measurement*, 4th. Michigan, USA: John Wiley & Sons, 2012.
- [3] F. Sauli, “The gas electron multiplier (GEM): Operating principles and applications,” *Nuclear Instruments and Methods in Physics Research Section A: Accelerators, Spectrometers, Detectors and Associated Equipment*, Aug. 2015. DOI: 10.1016/j.nima.2015.07.060.
- [4] V. X. P. Carvalho, “Large Area Cascaded Gas Electron Multipliers for Imaging Applications,” English, MA thesis, Universidade de Coimbra, Coimbra, Portugal, 2015.
- [5] J. Mir, H. N. Luz, X. Carvalho, C. D. R. Azevedo, J. M. F. Santos, and F. Amaro, “Gain Characteristics of a 100 μm thick Gas Electron Multiplier (GEM),” *Journal of Instrumentation*, vol. 10, 12 Dec. 2015. DOI: 10.1088/1748-0221/10/12/C12006.
- [6] F. D. Amaro, J. A. Mir, X. Carvalho, C. D. R. Azevedo, J. M. F. Santos, and H. N. Luz, “A robust large area x-ray imaging system based on 100 μm thick Gas Electron Multiplier,” *Journal of Instrumentation*, vol. 10, 12 Dec. 2015. DOI: 10.1088/1748-0221/10/12/C12005.
- [7] H. N. da Luz, J. A. Mir, X. Carvalho, and J. M. F. dos Santos, “X-ray imaging with GEMs using 100 μm thick foils,” *Journal of Instrumentation*, vol. 9, no. 06, p. C06007, 2014. [Online]. Available: <http://stacks.iop.org/1748-0221/9/i=06/a=C06007>.
- [8] C. D. R. Azevedo, S. Biagi, R. Veenhof, P. M. Correia, A. L. M. Silva, L. F. N. D. Carramate, and J. F. C. A. Veloso, “Position resolution limits in pure noble gaseous detectors for X-ray energies from 1 to 60 keV,” *Physics Letters B*, vol. 741, Feb. 2015. DOI: 10.1016/j.physletb.2014.12.054.
- [9] K. Iniewski, *Medical Imaging: Principles, Detectors, and Electronics*, I. John Wiley & Sons, Ed. 2009.
- [10] R. A. Serway and J. W. J. Jewett, *Physics for Scientists and Engineers with Modern Physics, Ninth Edition*, B. Cole, Ed. 2014, ISBN: 978-113395405-7.
- [11] G. Zentai, “X-ray imaging for homeland security,” 2008, ISBN: 978-1-4244-2496-2. DOI: 10.1109/IST.2008.4659929.
- [12] Pinsdaddy. (2018). A simple diagram x ray tube pictures to pin on pinterest - pinsdaddy, [Online]. Available: http://www.pinsdaddy.com/a-simple-diagram-x-ray-tube-Kr3Mh8xMusyT35kh1nRJ4eLLBnUEMP4JK7Yc*VUCMLU/ (visited on 02/20/2018).
- [13] P. Sprawls. (2000). X-Ray Production, [Online]. Available: <http://www.sprawls.org/ppmi2/XRAYPR0/#Function> (visited on 08/17/2017).
- [14] Journal of Nuclear Medicine Technology. (2004). X-ray imaging physics for nuclear medicine technologists. part 1: Basic principles of x-ray production, [Online]. Available: <http://tech.snmjournals.org/content/32/3/139/F4.expansion.html> (visited on 02/20/2018).
- [15] P. D. P. Cattin. (2016). Basics of x-ray: Principles of medical imaging, [Online]. Available: [https://miac.unibas.ch/PMI/01-Basics0fXray.html#\(1\)](https://miac.unibas.ch/PMI/01-Basics0fXray.html#(1)) (visited on 02/20/2018).
- [16] T. E. Brown, T. L. Brown, J. H. Eugene LeMay, B. E. Bursten, C. Murphy, and P. Woodward, *Chemistry: The Central Science, 12th Edition*, 12th ed.
- [17] U. of Oxford. (2018). History archive, [Online]. Available: <http://www.physics.ox.ac.uk/history.asp?page=moseley> (visited on 05/07/2018).

- [18] S. Editors. (2017). Infrared (IR), [Online]. Available: <http://www.spectroscopyonline.com/x-ray-fluorescence-and-raman-spectroscopy-help-uncover-archeological-facts> (visited on 05/07/2018).
- [19] K. Trentelman, K. Janssens, G. van der Snickt, Y. Szafran, A. T. Woollett, and J. Dik, "Rembrandt's an old man in military costume: The underlying image re-examined," *Applied Physics A*, vol. 121, no. 3, pp. 801–811, 2015. DOI: 10.1007/s00339-015-9426-3. [Online]. Available: <https://doi.org/10.1007/s00339-015-9426-3>.
- [20] S. G. Monteiro, "Características de Desempenho do MPGD THCOBRA a operar em AR/CH₄," MA thesis, Universidade de Aveiro, 2016.
- [21] E. Aprile, A. E. Bolotnikov, A. I. Bolozdynya, and T. Doke, *Noble Gas Detectors*. 2006, ISBN: 3527405976.
- [22] L. F. das Neves Dias Carramate, "Development of a single photon counting computed tomography system using MPGDs," PhD dissertation, Universidade de Aveiro, 2014.
- [23] N. Power, Ed. (2018). Interaction of Gamma Radiation with Matter, [Online]. Available: <http://www.nuclear-power.net/nuclear-power/reactor-physics>.
- [24] W. U. Boeglin, Ed. (). Compton Scattering, Background, [Online]. Available: http://wanda.fiu.edu/teaching/courses/Modern_lab_manual/Compton_Scattering.html.
- [25] RadiologyKey. (2018). Basic radiation protection and radiobiology, [Online]. Available: <https://radiologykey.com/basic-radiation-protection-and-radiobiology-2/> (visited on 02/20/2018).
- [26] M. D. R. Silva, "Ionizing Radiation Detectors, Evolution of Ionizing Radiation Research," *InTech*, 2015. DOI: 10.5772/60914.
- [27] European Nuclear Society. (2017). Ionization chamber, [Online]. Available: <https://www.euronuclear.org/info/encyclopedia/i/ionizationchamber.htm> (visited on 09/04/2017).
- [28] N. T. Associates. (2015). How do geiger counters work? [Online]. Available: <http://www.ntanet.net/how-do-geiger-counters-work> (visited on 02/20/2018).
- [29] M. Titov, "Gaseous detectors: Recent developments and applications," in *Physics: Instrumentation and Detectors*, C. U. Library, Ed., 2010.
- [30] A. F. Buzulutskov, "Radiation Detectors Based on Gas Electron Multipliers (review)," *Instruments and Experimental Techniques*, vol. 50, no. 3, pp. 287–310, 2007. DOI: 10.1134/S0020441207030013.
- [31] European Organization for Nuclear Research, *Close view of a GEM electrode, etched on a metal-clad, 50 μm thick polymer foil. the hole's diameter and distance are 70 μm and 140 μm*, 2016. [Online]. Available: <http://gdd.web.cern.ch/GDD/>.
- [32] European Organization for Nuclear Research, *Field lines and equipotentials in the GEM holes on application of a voltage between the two metal sides. a Drift (top) and Transfer field (bottom) transport ionization electrons into and out of the holes*, 2016. [Online]. Available: <http://gdd.web.cern.ch/GDD/>.
- [33] R. Chechik, M Cortesi, A Breskin, D Vartsky, D. Bar, and V. Dangendorf, "Thick GEM-like (THGEM) Detectors and their Possible Applications," presented at the SNIC Symposium, Stanford, California, 2006.
- [34] *The chemical composition of earths atmosphere III: The noble gases*, 2015. [Online]. Available: <http://www.gly.uga.edu/railsback/Fundamentals/AtmosphereCompIII.jpg>.
- [35] M. Ribeirete, A. Policarpo, M. Salete, S. Leite, M. Alves, and E. D. Lima, "Fano factors of krypton-xenon mixtures," *Nuclear Instruments and Methods in Physics Research*, vol. 214, 2-3 1983. DOI: 10.1016/0167-5087(83)90636-1.

- [36] F. I. G. M. Borges and C. A. N. Conde, "Experimental W-values in gaseous Xe, Kr and Ar for low energy X-rays," *Nuclear Instruments and Methods in Physics Research Section A: Accelerators, Spectrometers, Detectors and Associated Equipment*, vol. 381, 1 1996. DOI: 10.1016/0168-9002(96)00739-5.
- [37] L. P. M. M. Carita, C. A. N. Conde, and F. P. Santos, "Quenched and Non-Quenched Ar-Xe Penning Mixtures as Detection Media for a Gridded-Microstrip Gas Chamber X-Ray Detector," *IEEE Transactions on Nuclear Science*, vol. 56, 3 Jun. 2009. DOI: 10.1109/tns.2009.2018267.
- [38] *Nist: x-ray mass attenuation coefficients - table 3*, 2016. [Online]. Available: <https://physics.nist.gov/PhysRefData/XrayMassCoef/tab3.html>.
- [39] M. Capeans, "Aging and materials: Lessons for detectors and gas systems," *Nuclear Instruments and Methods in Physics Research Section A: Accelerators, Spectrometers, Detectors and Associated Equipment*, vol. 515, 1-2 2003. DOI: 10.1016/j.nima.2003.08.134.
- [40] R. C. Gonzalez and R. E. Woods, *Digital Image Processing*, 2nd ed. Prentice Hall, 2002, ISBN: 9780130946508.
- [41] L. F. N. D. Carramate, A. L. M. Silva, C. D. R. Azevedo, D. S. Covita, and J. F. C. A. Veloso, "THCOBRA X-ray imaging detector operating in Ne/CH₄," *Journal of Instrumentation*, vol. 10, 01 Jan. 2015. DOI: 10.1088/1748-0221/10/01/P01003.
- [42] E. M. Hussein, *Handbook on Radiation Probing Gauging Imaging and Analysis Applications*, 1st ed., ser. Plastics Engineering. Springer, 2003, ISBN: 1402012950.
- [43] W. R. Leo, *Techniques for Nuclear and Particle Physics Experiments: A how-to Approach*, 1st edition. SpringerVerlag, 1987, 1987.
- [44] J. T. Bushberg, J. A. Seibert, E. M. L. Jr., and J. M. Boone, *The Essential Physics of Medical Imaging*. Lippincott Williams & Wilkins, isbn = 9780781780575, year = 2011, edition = 3rd,
- [45] I. T. Young, J. J. Gerbrands, and L. J. v. Vliet, "Fundamentals of Image Processing," *Delft University of Technology*,
- [46] D. J. Schroeder, *Astronomical optics*. Academic Press, 1987, ISBN: 012629805X, 9780126298055, 0126298068.
- [47] A. Duatti. (2014). Diffraction limit on spatial resolution of light microscopy, [Online]. Available: https://www.researchgate.net/figure/263207980_fig1-FIGURE-1-Diffraction-limit-on-spatial-resolution-of-light-microscopy-a-Point-spread (visited on 08/21/2017).
- [48] P. Huynh, T.-H. Do, and M. Yoo, "A Probability-Based Algorithm Using Image Sensors to Track the LED in a Vehicle Visible Light Communication System," *Sensors*, vol. 17, no. 2, p. 347, 2017. DOI: 10.3390/s17020347. [Online]. Available: <https://doi.org/10.3390/s17020347>.
- [49] E. Oh, S. Cho, Y.-H. Ahn, Y. Park, J.-H. Ryu, and S.-W. Kim, "2012 IEEE International Geoscience and Remote Sensing Symposium - In-orbit optical performance assessment of Geostationary Ocean Color Imager," 2012, ISBN: 978-1-4673-1159-5, 978-1-4673-1160-1, 978-1-4673-1158-8, DOI: 10.1109/IGARSS.2012.6352331.
- [50] Casa Software Ltd., *Edge Measurements using a Complementary Error Function*, English, CasaXPS, Ed. [Online]. Available: www.casaxps.com.
- [51] ISO, *BS ISO 15529:2010, Optics and photonics - Optical transfer function - Principles of measurement of modulation transfer function (MTF) of sampled imaging systems*, ed. by bsi., ISO.
- [52] G. C. Smith, J. Fischer, and V. Radeka, "Photoelectron range limitations to the spatial resolution for x-rays in gas proportional chambers," *IEEE Transactions on Nuclear Science*, vol. 31, 1 1984. DOI: 10.1109/tns.1984.4333221.

- [53] J. Cussonneau, M Labalme, P Lautridou, L Luquin, V Metivier, A Rahmani, and T Re-poseur, "2D localization using resistive strips associated to the Micromegas structure," *Nuclear Instruments and Methods in Physics Research Section A: Accelerators, Spectrometers, Detectors and Associated Equipment*, vol. 492, 1-2 2002. DOI: 10.1016/S0168-9002(02)01275-5.
- [54] P. H. F. N. d. Luz, "Development of neutron and x-ray imaging detectors based on MHSP," English, doctorate dissertation, Universidade de Aveiro, Aveiro, Portugal, 2009.
- [55] M. Villa, "Developing and evaluating new micropattern gas detectors," PhD thesis, Universitäts-und Landesbibliothek Bonn, 2014.
- [56] O. Instruments, *Apogee, Packaged x-ray tubes*, Technical Data Sheet.
- [57] Bronkhorst, *EL-Flow Prestige series Thermal Mass Flow Meters/Controllers, Instruction manual*, English.
- [58] A. Liquide. (2018). Gas Encyclopedia Air Liquide | Air Liquide, [Online]. Available: <https://encyclopedia.airliquide.com/> (visited on 09/06/2017).
- [59] Canberra, *Model 2004 Semiconductor Detector Preamplifier*, ed. by M. Technologies, 2017. [Online]. Available: http://www.canberra.com/products/radiochemistry_lab/pdf/Model-2004-SS.pdf.
- [60] Physics Open Lab. (2016). PMT Pulse Processing, [Online]. Available: <http://physicsopenlab.org/2016/04/21/pmt-pulse-processing/> (visited on 09/21/2017).
- [61] CAEN, *DPHA user manual*.
- [62] NIST. (2017). X-ray mass attenuation coefficients, [Online]. Available: <https://physics.nist.gov/PhysRefData/XrayMassCoef/ElemTab/z82.html>.
- [63] NIST. (2017). X-ray mass atten. coef. - tissue, soft (icru-44), [Online]. Available: <https://physics.nist.gov/PhysRefData/XrayMassCoef/ComTab/tissue.html> (visited on 12/20/2017).
- [64] NIST. (2017). X-ray mass atten. coef. - adipose tissue (icru-44), [Online]. Available: <https://physics.nist.gov/PhysRefData/XrayMassCoef/ComTab/adipose.html> (visited on 12/20/2017).
- [65] B. Z. Shakhreet, S. Bauk, A. A. Tajuddin, and A. Shukri, "Mass attenuation coefficients of natural rhizophora spp. wood for x-rays in the 15.77-25.27 keV range," *Radiation Protection Dosimetry*, vol. 135, 1 Jul. 2009. DOI: 10.1093/rpd/ncp096.
- [66] NIST. (2017). X-ray mass atten. coef. - bone, cortical (icru-44), [Online]. Available: <https://physics.nist.gov/PhysRefData/XrayMassCoef/ComTab/bone.html> (visited on 12/20/2017).
- [67] NIST. (2017). X-ray mass atten. coef. - polystyrene, [Online]. Available: <https://physics.nist.gov/PhysRefData/XrayMassCoef/ComTab/polystyrene.html> (visited on 03/25/2018).
- [68] P. D. Burns, "Slanted-Edge MTF for Digital Camera and Scanner Analysis," presented at the IS&T's 2000 PICS Conference (Rochester, NY USA), Eastman Kodak Company.
- [69] B. Perry, "Algorithm for MTF Estimation by Histogram Modeling of an Edge," Rochester Institute of Technology, 2001. [Online]. Available: <https://www.cis.rit.edu/research/thesis/bs/2001/perry/contents.html>.
- [70] E. M. A. Hussein, *Handbook on Radiation Probing, Gauging, Imaging and Analysis: Volume I: Basics and Techniques*, 1st ed. Springer Netherlands, 2004, ISBN: 978-1-4020-1294-5.
- [71] A. C. Thompson, E. M. Attwood David T. Gullikson, and et al, *X-Ray Data Booklet*, L. B. N. Laboratory, Ed., 2001.
- [72] M. Altunbas, E. Barasch, M. Maier, D. Bednarek, S. Rudin, A. Greenwald, E. Johnson, and M. Pralle, "High pressure GEM performance with argon, krypton and xenon gas mixtures," vol. 1, 2004, ISBN: 0-7803-8700-7. DOI: 10.1109/nssmic.2004.1462256.

Part V
APPENDIX

SCREENSHOTS OF THE ANALYSIS ENVIRONMENT

Some illustrative screenshots of the analysis environment are presented bellow, as its development was key for many of the results obtained in this investigation. This analysis was performed in jupyter notebooks.

Firstly, figure 74 illustrates the output of a single image reconstruction where the file name is given by the user. Additional parameters like the indication to save the results, title addition and legend specifications are also provided.

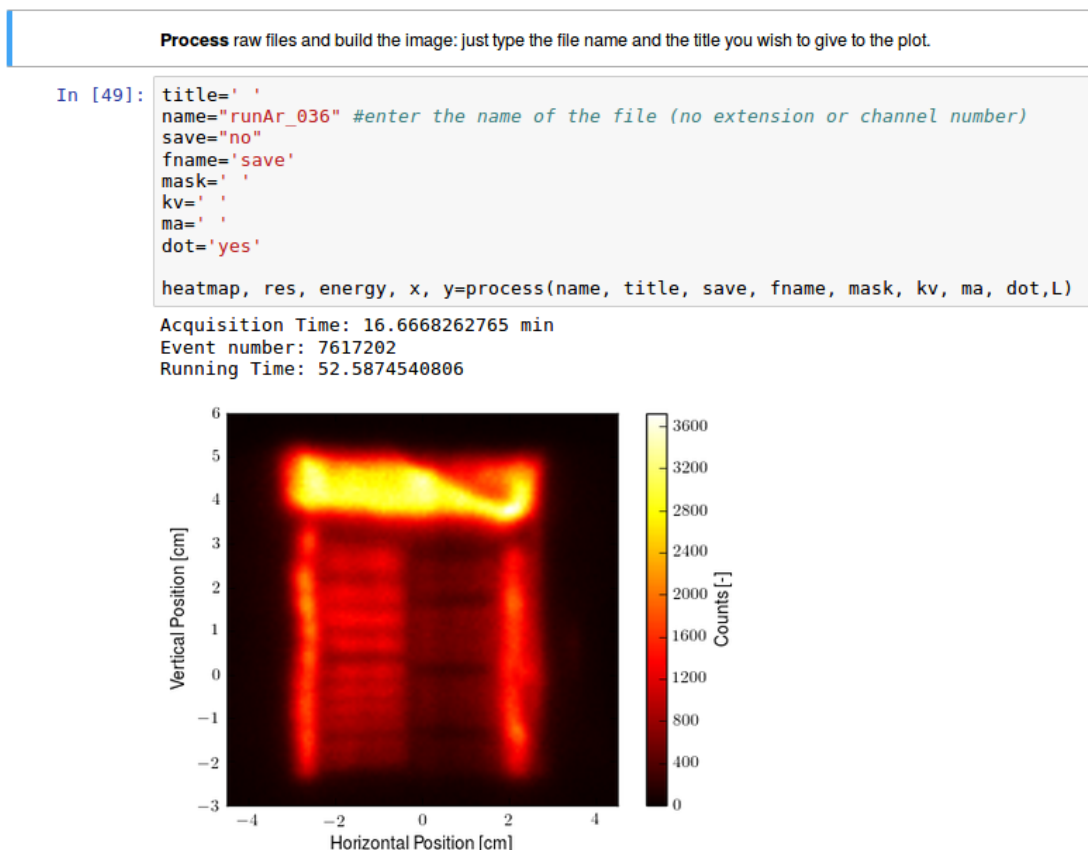


Figure 74: **Image reconstruction cell**: only the file title is needed to start the correspondent image reconstruction. The outputs are the acquisition time, number of events selected, the total running time and the final image histogram.

After processing the raw files by calling the python script running in the background, this function outputs the acquisition time (which is a specification of the experimental data), the number of events that were not rejected during coincidence analysis and the total running time of the software operations. Also, the reconstructed image is plotted as an histogram.

Another interesting tool was sub-image formation by energy filtering, represented in figure 75.

From the total energy histogram, the user may define the desired number of energy intervals and reconstruct sub-images within that regions. For this, only the array of energy limits must be provided. Additional measurements can be made with the

Determine the energy spectrum of the image and make energy cuts.

```
In [53]: n_images=8
save='no'
savename='fname'
cuts=[2,4,6,8,10,12,14,16,18]
fendas='no'
Minx=-4
Maxx=2
Miny=4
Maxy=4.5
profile='no'
sum_x='no'
sum_y='yes'
mtf='no'
energy_cut(heatmap, n_images, save, savename, energy, x, y, res, fendas, Minx, Maxx, Miny, Maxy, cuts, profile, sum_x, sum_y)
```

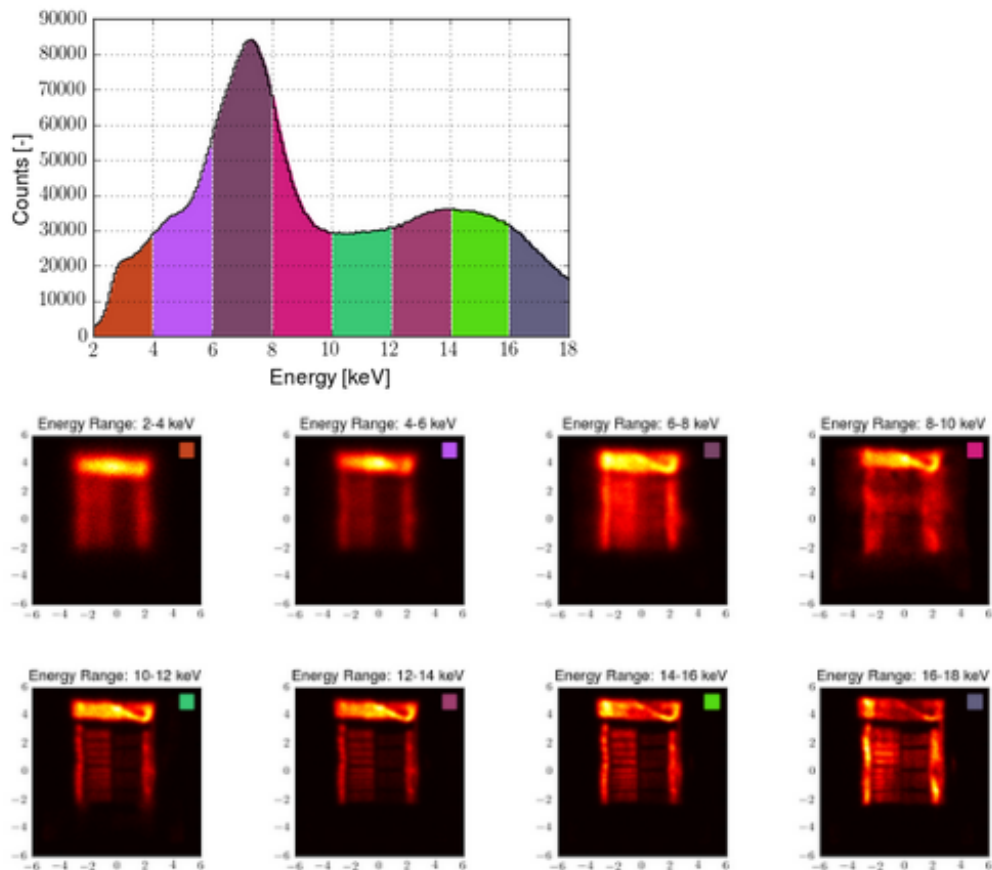


Figure 75: **Sub-image reconstruction cell**: the energy histogram is subdivided into user-defined regions and the events within each energy range are combined to form a sub-image.

energy_cut function, like RoI definition for all images, double slit and PSF profiling, as well as position resolution and MTF determination.

The outputs of the remaining developed functions are not shown here, as they were already shown in the course of this dissertation.

ANALYSIS IMAGES

The images used for SNR, position resolution and MTF determination are presented in figure 76.

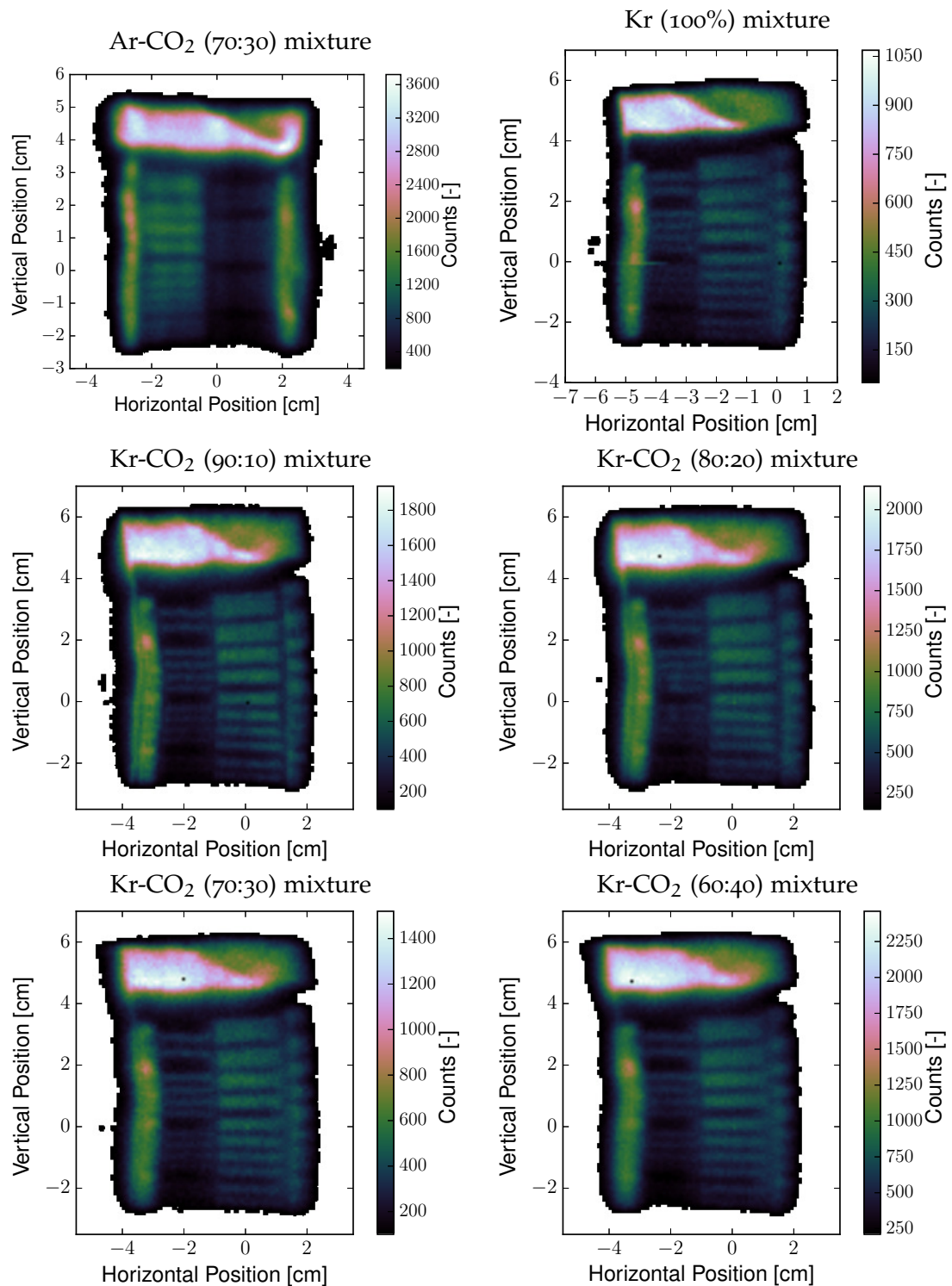


Figure 76: Images used for SNR, position resolution and MTF determination: the MTF mask was irradiated with the x-ray generator with energies up to 30 keV.

All images were acquired with $\mathcal{M} = 1$, a tube voltage near 30 keV and the maximum limiting current that prevented signal collection saturation (this was done by assuring the four channels had similar count rates). The exposition time was 1000 s for all cases. At the top of the MTF mask, a rectangular window (framed with lead sheats) was left open to provide a known length, a sharp edge profile and an uniform region. This information allowed, respectively, position calibration, position resolution (as well as MTF) calculation and image SNR determination.

These acquisitions were made by imposing similar values of charge gain (which are presented in table 13), by tuning the electric fields for each different gas mixture.

Table 13: **Charge gain and energy resolution for the quantitative analysis:** the values of charge gain and energy resolution are presented for the images in figure 76. These values were calculated by fitting a Gauss function to a ^{55}Fe -source energy spectrum acquired under the same conditions as the correspondent image.

MIXTURE	CHARGE GAIN	ENERGY RESOLUTION
ARGON	6.3×10^3	18.99%
100%	6.3×10^3	21.02%
90:10	7.1×10^3	25.50%
80:20	6.0×10^3	26.89%
70:30	6.6×10^3	30.34%
60:40	6.6×10^3	30.00%